Title

Growth of Highly Crystalline MoS2 Thin Films by Pulsed Laser Deposition

Author

Diamond, Anthony

Publication Date

2020

Peer reviewed|Thesis/dissertation

Growth of Highly Crystalline MoS_2 Thin Films by Pulsed Laser Deposition

by

Anthony Michael Diamond

A dissertation submitted in partial satisfaction of the
requirements for the degree of
Doctor of Philosophy

in

Engineering - Materials Science and Engineering

in the

GRADUATE DIVISION
of the
UNIVERSITY OF CALIFORNIA, BERKELEY

Committee in charge:

Professor Ramamoorthy Ramesh, Chair
Professor Mark Asta
Professor Sayeef Salahuddin

Summer 2020

Growth of Highly Crystalline MoS_2 Thin Films by Pulsed Laser Deposition

Abstract

Growth of Highly Crystalline MoS_2 Thin Films by Pulsed Laser Deposition

by

Anthony Michael Diamond
Doctor of Philosophy in Engineering - Materials Science and Engineering

University of California, Berkeley

Professor Ramamoorthy Ramesh, Chair

This dissertation presents a growth and characterization study of MoS_2 thin films deposited by pulsed laser deposition, with specific interest in demonstrating precise thickness control down to a single monolayer and high film uniformity over large areas (0.25 cm^2). Limits to traditional methods for scaling field effect based switching devices have necessitated the development of alternative device architectures. Devices utilizing two-dimensional materials such as MoS_2 have demonstrated improved electrostatic integrity at small scales while tunneling field effect transistors have demonstrated a pathway toward reduced power consumption. However, drawbacks to previously explored synthesis techniques have limited the applicability of MoS_2 for these applications. Toward this goal, the work presented establishes repeatable growth conditions to fabricate highly crystalline and uniform MoS_2 thin films over technologically significant dimensions and establishes the efficacy of pulsed laser deposition as a suitable synthesis technique. Films grown herein are found to be p-type with significant defect densities suggesting avenues for future research.

To Jeanne Heard Bazemore for teaching me what tenacity looks like,
To Robert Annear for teaching me what an engineer looks like,
To Michael Bazemore for teaching me what focus looks like,
To Branford Marsalis for teaching me what staying in the pocket looks like,

And to my Mother for teaching me all the above and so much more...

Table of Contents

List of Figures

List of Tables

Acknowledgements

This thesis is dedicated to my family who I have been so blessed to have in my life. From nurturing my curiosity, to instilling an attitude of tenacity and persistence, to sacrificing in support of my dreams, it is not hyperbole to say that all my accomplishments belong to you. Ubuntu: I am because we are.

To Professor Ramamoorthy Ramesh, I am extremely grateful for the opportunity you have provided for me to study at UC Berkeley and the belief you have shown in me along the way. You embody the uncompromising pursuit of scientific truth and carry on the legacy of those greatest of scientists that lifted our species from the dark ages into the age of enlightenment. May that spirit live on in me and all of your students.

I would like to thank my qualifying exam committee members, Professors Oscar Dubon and Jie Yao, and my dissertation committee members, Professors Mark Asta and Sayeef Salahuddin for their continued support throughout my graduate program at UC Berkeley. To Professor Dubon, your welcoming spirit and genuine interest in my academic journey helped to make me feel at home in the program. To Professor Yao, your enthusiasm and openness are characteristics that I continue to strive for in all of my collaborations. To Professor Asta, your integrity and accessibility were foundational to me during my time at UC Berkeley. To Professor Salahuddin, your collaborative leadership style and its empowering impact on the members of your research team garnered my respect and admiration throughout my graduate years and continue to serve as a model I try to emulate in all of my work.

To my principal collaborator, teacher, and friend, Claudy Ryan Serrao who taught me so much in areas of both science and life. Your mentorship and friendship was and is a source of joy and inspiration.

I would like to thank Shang-Lin Hsu for the TEM images and Long You for the electrical characterization work that was used in this dissertation.

I would like to thank Professors Alberto Salleo and Heinz Pitsch who contributed greatly to my academic career at Stanford University and encouraged me to continue my graduate studies and pursue doctoral research in Materials Science and Engineering.

I would like to thank my labmates John Heron, Morgan Trassin, Ajay Yadev, Di Yi and James Clarkson for fostering a collaborative work environment filled with intellectual discord, coffee breaks (where much of the real science happened) and for teaching me the guiding principle: to challenge ideas, not people.

Finally, I would like to express my appreciation for the financial support provided by the National Science Foundation Graduate Research Fellowship Program and the Chancellor's Fellowship awarded by the University of California Berkeley Graduate Division. The research presented herein was supported in part by Army Research Office contract no:W911NF-13-1-0224, Air Force Office of Scientific Research contract no: FA9550-13-1-0114, NSF grant number DMR-1207053 (RM and CC), and the IRICE program at UC Berkeley.

Chapter 1

Introduction

Materials have played a central role throughout human history. Tools and technologies available to humanity have been so foundational to the human experience that historical ages are regularly named for the most significant materials humans knew how to work with during the time. The Stone Age, lasting roughly 3.3 million years, was demarcated by the use of stone by early humans to make implements with edges, points, or as percussive tools [1]. The transition to the Bronze Age occurred roughly around 3300 BCE at which point heat began to be used in conjunction with low melting point alloys of copper and tin to make bronze [2]. The advent of this material and its associated processing techniques opened up an entirely new set of technologies such as tools to aid in agricultural production and for use in weaponry. The Iron Age was delineated by the time during which the production of iron advanced to the point where iron tools and weapons were superior to their bronze counterparts and became widespread. Archeologists place this transition sometime between 1200–550 BCE [3]. Beginning in the 1800s, the use of engineered alloys of iron (steel) became widespread.

As our understanding of the physical world increased, so too did our use of electronic materials. Starting with conductors to transmit signals long distance in the form of the telegraph and continuing to radio wave communications, electrical signals emerged as an excellent way to transmit and process information. Because of the ease of detection relative to the noise of the transmission process, binary signals became the standard way to encode information. Electrical switches are fundamental to these encoding and processing techniques. Over time these switches moved from manually to electrically actuated in the form of electromechanical relays and then became electrically switched in the case of vacuum tubes. With the development of solid state physics and the utilization of semiconducting materials, solid state electronic devices were used for the first time for signal processing in the early twentieth century ushering in the Silicon Age.

Over the last century, computational systems have had a transformative effect on human society. Nearly every facet of human activity has been touched in one way or another by digital information systems. Their ubiquity has been established in part by the development of integrated circuits (ICs). As opposed to discrete circuits that consist of independent circuit components which are then assembled into circuits, ICs are usually fabricated out of a single flat piece (chip) of semiconducting material. Silicon is frequently used for the chips, allowing for billions of circuit elements to be patterned by photolithographic processes into complex circuits with high reliability and repeatability at very low cost. In addition, ICs possess drastically enhanced computational performance compared to what is achievable in discrete circuits due to the density of electrical components achievable with ICs. At their most fundamental level, modern ICs consist of billions of switching circuit elements called transistors which are integrated into combinational logic circuits.

1.1 Introduction to Transistors

The most commonly used transistors in ICs are bipolar junction transistors (BJTs) and field effect transistors (FETs). BJTs use two junctions of N-type and P-type semiconductors forming NPN or PNP devices. Just as in PN junctions, minority carrier diffusion plays a key role in device operation and the name of this device type "bipolar" is in reference to this fact. An NPN device for example consists of a heavily doped N-type emitter, a P-type base, and an N-type collector. In typical operation, the junction formed between the emitter and base is forward biased and the junction between the base and collector is reverse biased. When the emitter-base junction is positively biased, thermally excited electrons will overcome the built-in voltage of the emitter-base depletion region, be ejected into the base, diffuse from the area of high concentration near the emitter-base interface towards the collector where they will be swept away by the built-in voltage of the base-collector depletion region. In order to avoid recombination in the base, the base layer must be made thin enough such that the diffusion time is much less than the minority-carrier lifetime. Devices are typically NPN which have higher transconductance as a result of the electron mobility being higher than the whole mobility [4, pp. 291–292].

BJTs can amplify current and are used as amplifiers in a wide array of electronic equipment such as televisions, audio amplifiers, and mobile phones. Additionally, because of their high transconductance, they excel in applications requiring high frequency analog circuits such as radio-frequency circuits for wireless systems. BJTs can be combined with FETs in ICs to take advantage of both types of devices [4, p. 195].

FETs, sometimes referred to as unipolar transistors, use a conducting channel to connect a source to a drain region. The conductivity of a conducting channel is modulated by a voltage that is applied between the gate and source terminals. Metal-oxide-semiconductor FETs (MOSFETs) achieve this by utilizing a metal as the gate, an intermediate oxide or insulator layer, and semiconductor as the channel.

MOSFETs require almost no input current from the signal to control the load current enabling them to draw little current when compared to BJTs [4, pp. 195–198].

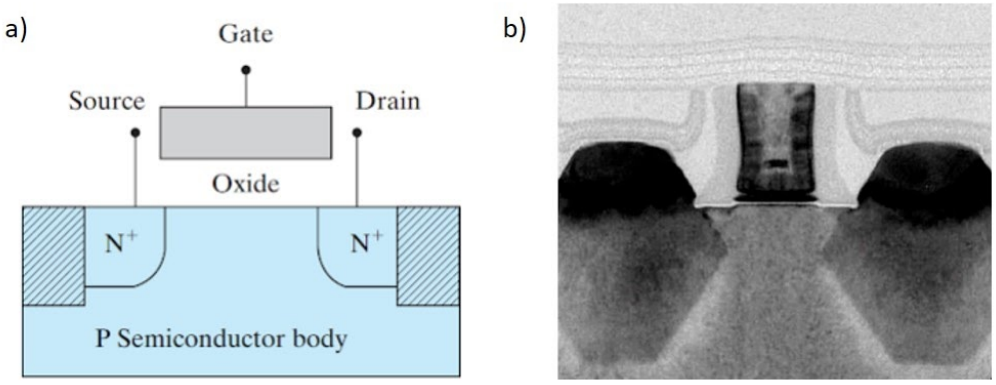

Figure 1.1) a) Schematic cross-sectional representation of the basic MOSFET structure [4, p. 196], b) TEM micrograph of a PMOS MOSFET device [5].

MOSFET channels can be made with N-type (NMOS) or P-type (PMOS) semiconductors and both types of transistors are typically combined in modern IC fabrication through the use of complementary metal-oxide-semiconductor architectures which rely on alternating PMOS and NMOS devices. Devices utilizing CMOS architectures possess low static power consumption, lower waste heat generation, and a high immunity to noise.

For a typical MOSFET during the On state the gate voltage V_{GS} is set to be higher than the required threshold voltage V_{TH}, inducing the semiconducting channel into a state of strong inversion whereby the built-in voltage between the channel and source/drain regions is significantly reduced. Under these conditions a voltage between the drain and source V_{DS} will induce a current I_{DS} which can be found by the following relation when $V_{DS} > (V_{GS} - V_{TH})$:

$$I_{DS} = \mu C_{OX} \frac{W}{L} (V_{GS} - V_{TH})^2$$

Where C_{OX} is the gate oxide capacitance, μ is the mobility (electron mobility for NMOS devices and hole mobility for PMOS devices), W is the FET channel width, L is the channel length. In this regime I_{DS} is proportional to the square of V_{GS} [6, p. 76]. When V_{GS} is greater than V_{TH} and $V_{DS} < (V_{GS} - V_{TH})$ this regime is referred to as the linear region [6, p. 76] and the drain current increases with both V_{GS} and V_{DS} following the relationship below:

$$I_{DS} = \mu C_{OX} \frac{W}{L} ((V_{GS} - V_{TH})V_{DS} + \frac{1}{2}V_{DS}^2)$$

However during the Off state, V_{GS} is typically significantly less than V_{TH} and the channel will be in a state of weak inversion. For a representative NMOS device

where source and body voltage are the same, the device current can be shown to follow the relationship below:

$$I_{DS} = \frac{\mu C_{OX} W}{L}(\eta - 1)V_T^2 e^{\frac{V_{GS}}{\eta V_T}}(1 - e^{\frac{-V_{DS}}{V_T}})$$

Where η is the subthreshold slope factor (typically between 1 and 1.5), V_T is the thermal voltage and is equal to $k_B T/q$ and V_A is the early voltage which characterizes the effect V_{DS} has on the drain-source current [6, p. 77].

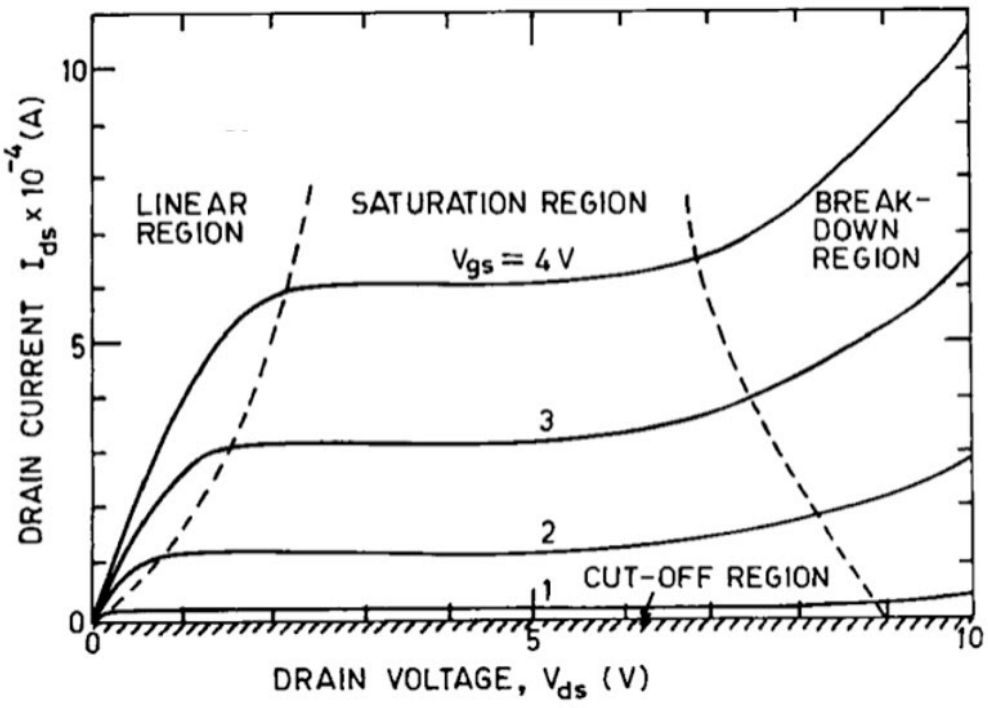

Figure 1.2) Plot of drain voltage (V_{ds}) and drain current (I_{ds}) characteristics with varying gate voltage (V_{gs}) highlighting different regions of typical device operation: linear, saturation, cut-off, and breakdown regions [6, p. 76].

For a typical NMOS device the sub-threshold slope derived from the small signal model can be shown to be:

$$S = \eta V_T ln(10)$$

In the ideal case $\eta = 1$, and at room temperature where $V_T \approx 26$ mV the ideal subthreshold slope for a MOSFET device $S \approx 60$ mV/decade. For more typical devices S is closer to 70-80 mV/decade [6, p. 266].

1.2 Moore's Law and the Future of the FET

In 1965, Gordon Moore's seminal paper "Cramming more components on integrated circuits" proposed, based on empirical observation, that a doubling of circuit components could be incorporated into integrated circuits every year [7]. Though later revised to a doubling every two years, the trend that was predicted has been maintained for more than four decades having enormous implications for the economics of computational power, the types of applications it can be applied to and expectations for continued economic growth.

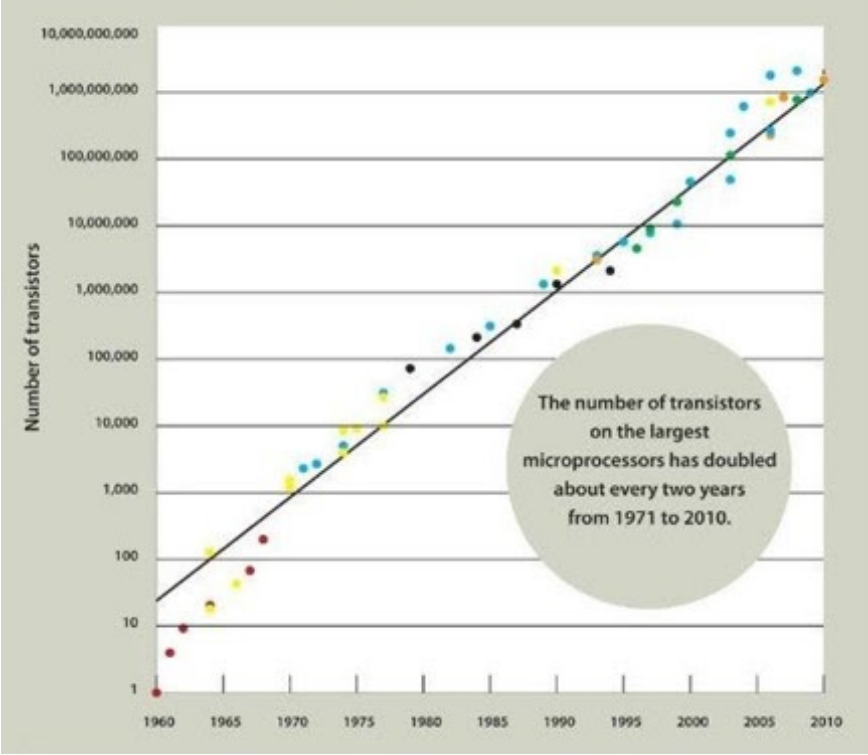

Figure 1.3) Graph depicting Moore's prediction (black line) along with points corresponding to transistor count of the largest commercially available microprocessors from 1960 to 2010 [8].

However, as the march of miniaturization has pushed on, continued progress has been threatened by a number of factors. The first has been that the processes required to make ICs utilizing very large scale integration (VLSI) have continued to grow in cost and complexity. With modern fabrication lines costing billions of dollars and containing hundreds of processes, it is becoming more difficult to bring new fab processes online and justify their costs [9].

Another limitation has been physical scaling. As channel widths have continued to shrink, traditional MOSFET devices have begun to exhibit a number of physical effects that manifest themselves when standard device architectures scale down. One

such limitation is drain-induced barrier lowering (DIBL) whereby the drain becomes so close to the source that the device configuration is able to form its own unique depletion region. This "punchthrough" is sufficient to enable a high drain voltage to effectively turn on the transistor. This can equivalently be thought of as a reduction of the threshold voltage [10, p. 198].

The strong lateral electric fields can also cause impact ionization between lattice atoms and charge carriers possessing high energies. This leads to the generation of electron hole pairs which can form a parasitic bipolar transistor between the bulk, source, and drain or avalanche electron-hole pair generation that cannot be controlled by the gate voltage [11].

Surface scattering at the interface between the channel and gate oxide also increases with shorter channels as the gate voltage must increase to offset the effects of stronger drain-source electric fields. This is regularly accomplished by making the gate oxide thinner but results in a larger component of acceleration toward the gate/channel interface [12].

Velocity saturation also occurs in short channel devices. As a result of the larger electric fields in the device, charge carriers will accelerate to their maximum velocity in the material limited by the material mobility. This, in turn, limits the achievable current I_{DS} for a given V_{DS} and causes I_{DS} to scale linearly instead of quadratically with V_{DS} in the saturation regime [13].

Finally, hot carrier injection (also referred to as aging) whereby charge carriers have sufficient energy to enter the gate oxide and begin to accumulate has been observed. The build up alters the response of the FETs to the gate voltage in a manner equivalent to changing the threshold voltage. It is typical to reduce the strength of the electric field in the channel by introducing regions of a lightly doped semiconductor which widens the depletion region; this, however, results in additional fabrication complexity [14].

Though device fabricators are bumping up against the limits of physical device scaling, other strategies are being employed to continue the march of IC computational power such as utilizing multiple cores to enable multi-thread parallel compute applications. Figure 1.4 below shows that while clock speed and single-thread performance has begun to stagnate, total transistor count and number of cores have continued to keep pace with Moore's Law.

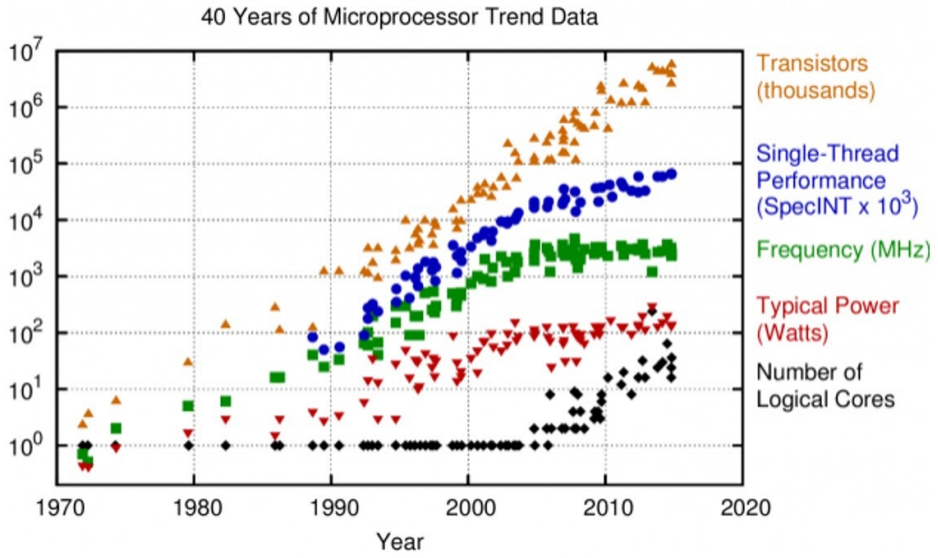

Figure 1.4) Plot of trends in key metrics for microprocessors over the last 40 years [15].

As devices have continued to shrink and power densities increase, thermal limitations have also become of principal concern with current devices well over 100 W/cm^2 and trending towards the power density of rocket engine nozzles in the coming generations.

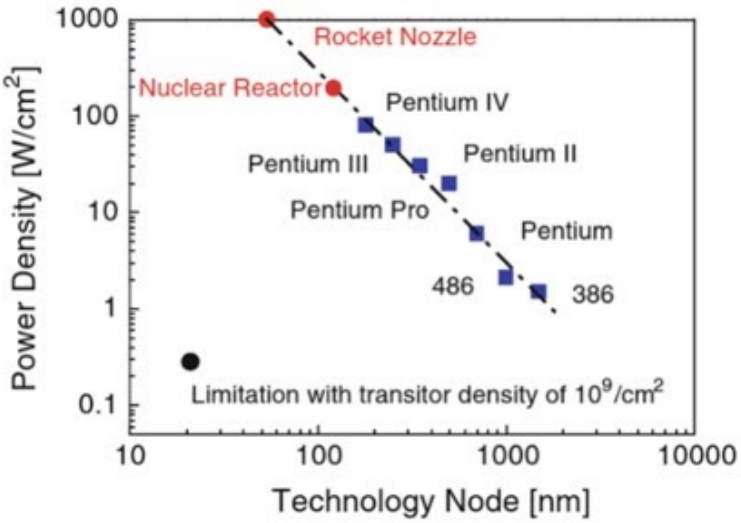

Figure 1.5) Plot of trends in power density for microprocessors vs. transistor node dimensions [16, p. 2].

Finally, power consumption has emerged as one of the most significant limitations. As the use of computational systems becomes more pervasive in our daily lives and the connectivity of our devices continues to grow, the volume of data available to be mined for actionable insights has exploded. The need for energy efficient computation has come to the forefront and can be thought of as being driven by two trends.

The first trend has been the emergence of the internet of things (IoT) and mobile applications. With improved internet connectivity it has become feasible to gather information about the world with remote computing devices that are able to communicate with the wireless networks with which they are connected. In this way, mobile devices are able to collect information about the world, communicate with and utilize applications running elsewhere which may be too computationally intensive to be completed by the mobile device via its network connection (colloquially referred to as the Cloud), and act on the world locally. The energy density of energy storage devices such as electrochemical batteries has not scaled as drastically as computational power and, as a result, power management is often a key consideration in the design of such devices. These mobile devices are also regularly in dormant states for much longer periods than in active states, therefore Off current or leakage power dissipation is very important.

The second major trend is the growth of compute power required for modern applications. Data Centers, which regularly house tens or hundreds of thousands of CPU cores, are illustrative of the massive power requirements that this growth has necessitated with data centers using a cumulative 200 TWh of energy annually as of 2018 [17]. These facilities are rarely in standby as compute jobs will be efficiently shuffled to maximize utilization of the available hardware, therefore On power consumption or dynamic power dissipation is the primary driver for these applications.

The primary contributor to leakage power dissipation in MOSFETs is subthreshold current which is defined as I_{DS} when $V_{DS} = V_{DD}$ and $V_{GS} = 0$ where V_{DD} is defined as the supply voltage. Many short channel effects previously discussed such as DIBL or charge carrier tunneling through the gate oxide as it becomes thin will enhance the leakage current of these devices [18]. It is valuable to appreciate that with ICs typically containing billions of FETs, even very modest Off currents on the order of nano amps can become quite large at scale.

One way to decrease I_{OFF} is to choose a larger V_{TH}. This is typically not done because it reduces I_{ON}, how quickly the next gate in a combinational logic circuit can be charged, and the overall speed of the device. Semiconductors with large direct bandgaps can exhibit much higher I_{ON} currents enabling fast devices with very low leakage currents. This continues to be an active area of research with the primary wide gap semiconductors of interest being III-V compound semiconductors [19].

Dynamic switching energy is the principal component of total power dissipated from operation of a CMOS based IC and it can be shown this value follows the relationship below:

$$P_d \propto V_{DD}(V_{DD} - V_{TH})^{\eta}$$

Where V_{DD} is the supply voltage, V_{TH} is the threshold voltage and η is the subthreshold slope factor [20]. From this relationship, it becomes apparent that if V_{TH} cannot be substantively increased then reductions in power dissipated must come from scaling down V_{DD} or decreasing η. Operating at lower values of V_{DD} increases the propagation delay (low-to-high or high-to-low) through a CMOS gate limiting device switching frequency and as a result this competing factor has constrained even more aggressive V_{DD} scaling [21].

Subthreshold slope affects both V_{DD} and leakage current and for this reason finding novel device architectures that don't rely on thermionic emission-like processes has been a major area of interest. One of the more promising approaches has been tunneling field effect transistors (TFETs). First proposed by Chang et al. at IBM in 1977, the TFET relies on band to band tunneling (BTBT) instead of thermionic emission as the charge transport mechanism. In its prototypical construction, a TFET would consist of a P-type and N-type source and drain regions separated by a gated intrinsic channel region. As there is greater accumulation in the intrinsic region due to gate biasing, eventually the tunneling width is reduced sufficiently to enable BTBT between the P-type and N-type source and drain regions [22]. Figure 1.6 demonstrates typical TFET operation.

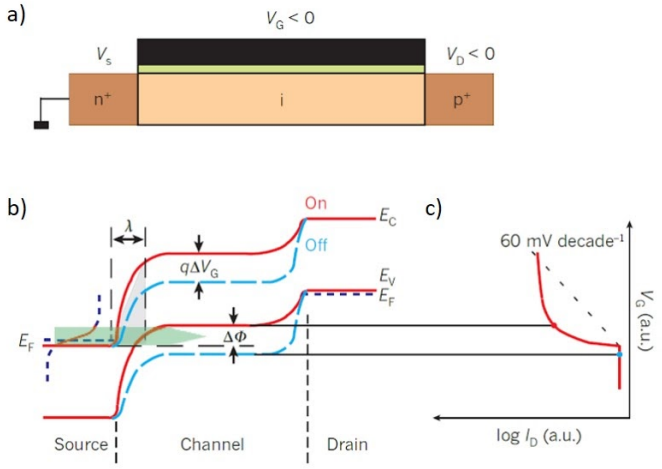

Figure 1.6) a) Schematic cross-sectional representation of a P-type TFET. b) Band diagram of the TFET in the Off state (dashed blue line) and in the On state (solid red). c) Plot of log source/drain current (I_D) vs.gate voltage (V_G) for the TFET with points indicating typical Off and On states in red and blue respectively. On this plot

the 60 mV/decade subthreshold slope of a typical MOSFET is plotted in dashed black lines for reference [23].

Significant advancement toward low subthreshold slope TFET devices has been made in recent years in a number of material systems including device architectures using SiGe, III-V semiconductors, Si and carbon nanotubes [24]–[29]. While both homojunction and heterojunction devices have been investigated, heterojunction devices possess higher On-state current densities due to the possibility of engineering very small tunneling barrier heights through the use of materials with the correct band alignments [27]. Notwithstanding tremendous progress in the field and the potential promise of TFETs, there has still been great difficulty in developing TFET devices with high On current and subthreshold slopes under 60 mV/dec over multiple current decades. Furthermore, devices with these improved performance characteristics that are also resistant to the limitations of physical scaling are required to extend Moore's Law into the next decade.

1.3 Introduction to TMDs and MoS_2

Two dimensional materials can be found in nature as bulk solids that are formed from the stacking of strongly bonded layers that are held together by weak van der Waal interactions. One of the 2D materials of great scientific interest has been graphene which exhibits a conical Dirac energy spectrum near the K point, producing charge carriers that can be described as essentially massless Dirac fermions that have important consequences for thermal conductivity and carrier mobility [30], [31]. Though the band-structure of graphene is the source of many interesting properties, there is no gap in the density of states which makes graphene incompatible with applications such as traditional electronic switching devices.

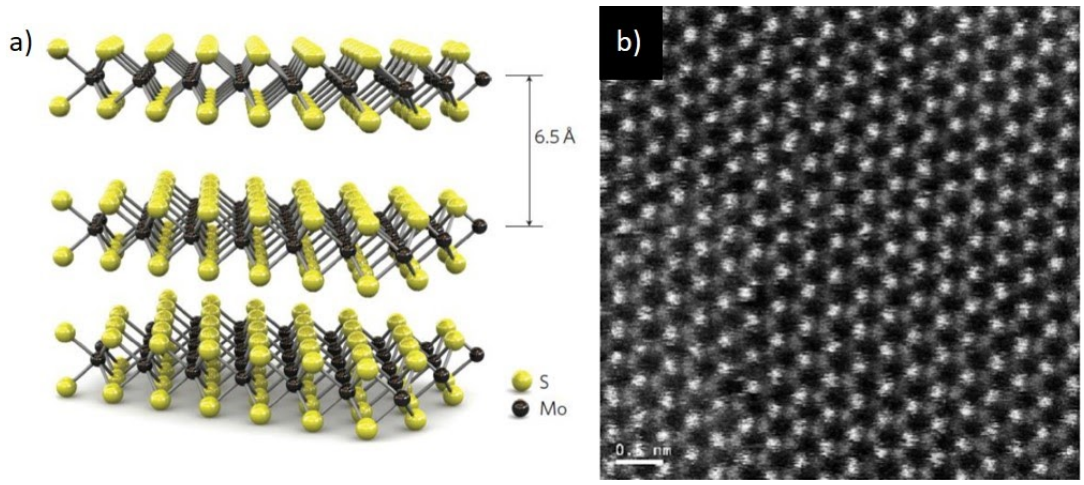

Figure 1.7) a) Schematic of the MoS_2 structure depicting the strong covalent bonds in the planar layers and weak interlayer van der Waals interactions [30]. b) Atomic resolution HAADF-STEM micrograph of single-layer MoS_2 [31].

Transition metal dichalcogenides (TMDs), in contrast to graphene, consist of stacked layers of covalently bonded transition metal and group six atoms which have large bandgaps as a result of the broken symmetry in the atomic basis set. TMDs typically have the chemical formula MX_2 where M is a transition metal such as Mo, W, Nb, Ta, Ti, or Re and X stands for chalcogenide atoms such as S, Se, or Te [32].

TMDs have been found to form many different structures such as fullerene-like nanoparticles or nanotubes [33]–[35], thin layers [36], [37] and bulk layered crystals and were significantly studied in the 1960s for applications such as catalysts and low friction coatings. As a result of the research interest in graphene, a large number of techniques were developed to isolate single layers from graphite [38]. These new techniques opened up the possibility to explore the properties of single layers of TMDs which quickly led to the discovery that single layers have electronic and optical properties that differ from the bulk materials and that TMDs could be used as the basis to form high-quality electronic devices [39].

Electronic structure calculations using density functional theory (DFT) based on a diverse set of exchange correlation functionals have played an important role in predicting the electronic and physical properties of MoS_2 and other TMDs [40]. In particular, changing the number of layers from bulk material to monolayers (ML) has shown a pronounced effect on the electronic structure. MoS_2, for example, is an indirect gap semiconductor in bulk experimentally determined to have a bandgap of 1.2 eV [41]. The shape of the conduction and valence bands undergo significant changes upon decoupling MoS_2 layers. Specifically, the valence band maximum (VBM) and conduction band minimum (CBM) go from the Γ point and another low-symmetry point of the Brillouin zone respectively to both being located at the K point with a direct gap observed by optical measurements to be 1.9 eV [42] and by DFT using local density approximation (LDA) to be 1.71 eV [40].

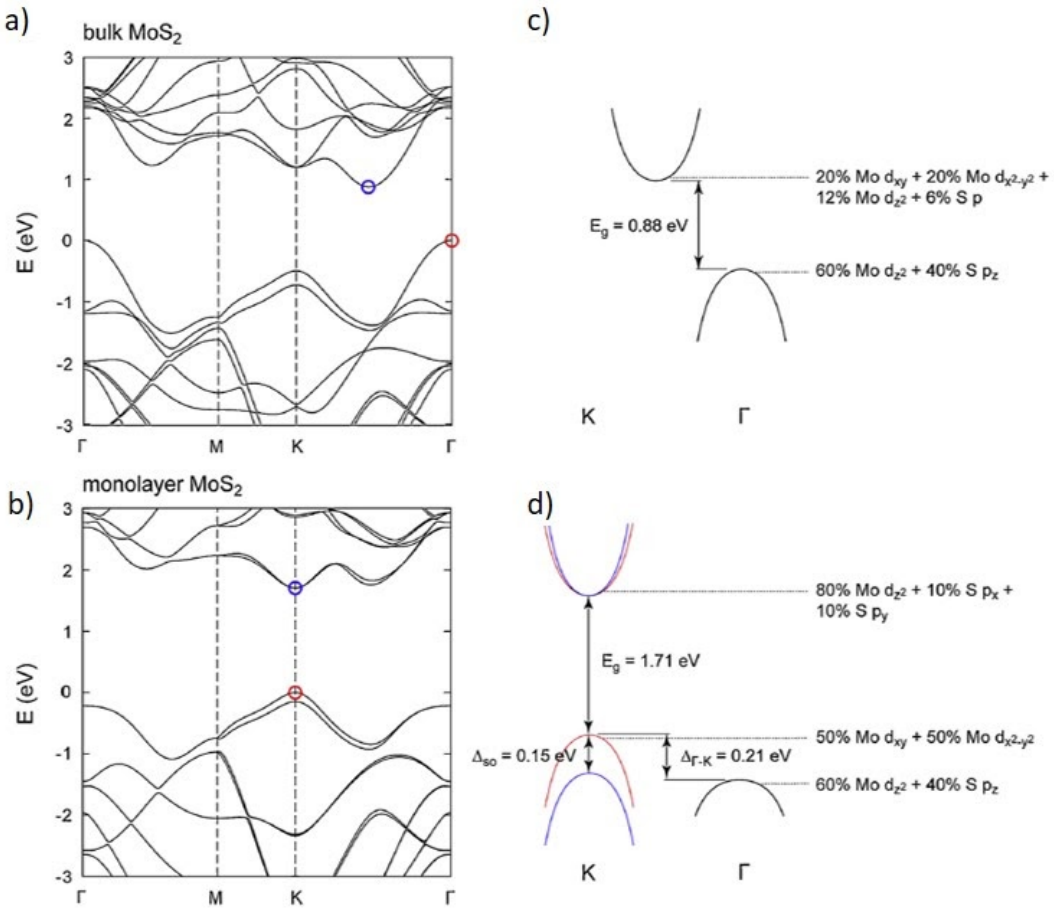

Figure 1.8) Band structure of a) bulk MoS_2 and b) monolayer MoS_2 calculated with DFT using the generalized gradient approximation (GGA). Schematic drawing of the low-energy bands depicting the valence band spin-orbit splitting and bandgap in c) bulk MoS_2 and d) monolayer MoS_2 [32].

These notable changes of the band structure that occur with a reduction in the number of layers are a result of the orbital composition of the involved electronic states. Localized d orbitals of the Mo atoms that are insensitive to interlayer spacing and experience limited coupling primarily form the conduction and valence band states. In contrast, the electronic states at the Γ point are largely composed of the p orbitals of the S atoms which do experience strong confinement effects as a result of neighboring MoS_2 layers. This results in substantial changes to the valence and conduction band upon the decoupling of MoS_2 layers which cause the K point to emerge as the VBM and CBM for a monolayer (ML) of MoS_2. Angle-resolved photoemission spectroscopy (ARPES) measurements have been successful at providing direct evidence confirming the predicted shift of the VBM from Γ to K occurring from a reduction in MoS_2 layers by accessing the dispersion of the valence band directly as highlighted in Figure 1.9 [43].

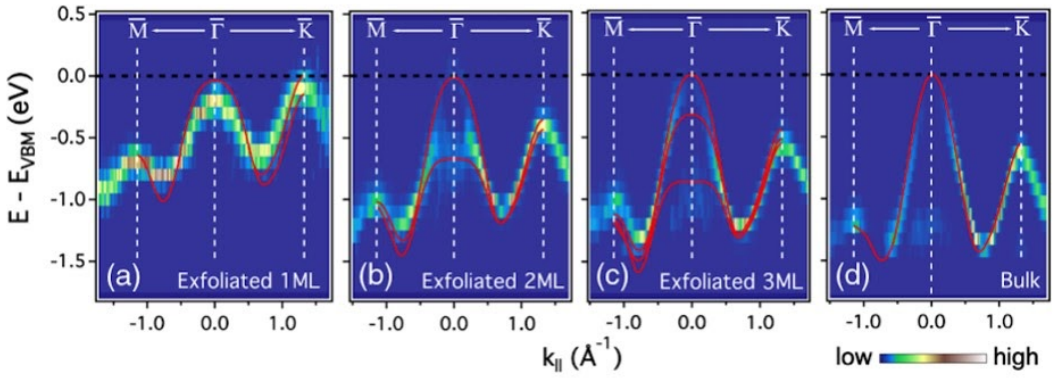

Figure 1.9) Plots of the low energy valence band of exfoliated a) monolayer, b) bilayer, c) trilayer and, d) bulk MoS_2 with overlaid red curves representing the corresponding bands calculated by DFT using GGA [43].

The other Mo and W based TMDs have been shown to possess qualitatively similar electronic properties. DFT calculations have demonstrated that all monolayer MX_2 semiconductors where M represents Mo or W have direct bandgaps between 1.06 and 2.66 eV using Heyd–Scuseria–Ernzerhof (HSE) exchange correlation functionals and GW correction [40]. Table 1.1 below gives an overview of bandgap results for this family by DFT with different exchange correlations. General trends include a reduction in the semiconductor bandgap coming from heavier chalcogenide atoms while the bandgap increases when replacing Mo with W.

	PBE (eV)	LDA (eV)	HSE (eV)	GW (eV)
MoS_2	1.67	1.86	2.25	2.66
$MoSe_2$	1.44	1.63	1.99	2.31
$MoTe_2$	1.07	1.23	1.59	1.77
WS_2	1.81	1.94	2.32	2.91
WSe_2	1.55	1.74	2.10	2.51
WTe_2	1.06	1.14	1.55	1.79

Table 1.1) Calculated bandgaps at the K-point of various TMDs calculated with DFT using Perdew–Burke-Ernzerhof (PBE), LDA, Heyd–Scuseria–Ernzerhof (HSE) exchange correlation functionals and GW correction [40].

1.4 MoS_2 Based Switching Devices

In addition to the presence of a bandgap, the atomic scale thickness or 2D nature of the material family is advantageous when compared to bulk or 3D materials because

of the reduced susceptibility of TMDs to short-channel effects such as DIBL which occur in FETs when they are miniaturized. The natural length λ, also referred to as the penetration length of the electric field induced from contacts into the semiconducting channel, can be characterized by the following relation:

$$\lambda = \sqrt{\frac{\varepsilon_{ch}}{\varepsilon_{ox}} t_{ox} t_{ch}}$$

Where ε_{ch} and ε_{ox} are dielectric constants of the channel and oxide, and t_{ch} and t_{ox} are the thickness of the channel and oxide, respectively. FET designs typically try to achieve channel lengths approximately four times longer than λ to ensure the device is not dominated by short channel effects; from this consideration it is clear that the atomic thickness of monolayer TMDs can enable very small λ values as a result of the very small value of t_{ch} [44].

Even while in-plane mobility of > 100 cm^2/Vs at room temperature in bulk MoS_2 and WSe_2 had been observed as early as the 1960s [45], TMDs were not seriously considered for electronics applications until the mid 2000s. The first transistors based on TMDs were fashioned from bulk WSe_2 in 2004 but demonstrated very poor On/Off ratios [46]. Shortly following the groundbreaking work of Novoselov and Geim to isolate and measure the properties of graphene [47] came the first demonstration of a transistor based on a single layer of MoS_2, though it suffered from a low On/Off ratios and low mobilities around 3 cm^2/Vs [38].

The room temperature mobility of MoS_2 is expected to have an upper limit in the range of 130 to 410 cm^2/Vs based on theoretical models and is thought to be limited by the mechanism of phonon scattering [48], [49]. Traditionally architected MoS_2 FETs have also been limited in performance by band tail trapping states. AC conductance measurements have been used to quantify their presence [50] and these trapping states may also have an affect on the band mobility measurements leading to the underestimation of mobility. Finally, an additional source of scattering may be local height fluctuations or ripples of the films that could reduce film conductivity [51].

One technique identified to improve mobility by presumably removing fabrication related residues and adsorbates that act as charged impurities was vacuum annealing [52]. This technique led to MoS_2 films with 250 cm^2/Vs Hall effect and 1000 cm^2/Vs field-effect effective mobilities with charge densities greater than 10^{13} cm^{-2} at low temperatures [53].

However, the most successful technique to improve the mobility of functional MoS_2 films and the associated understanding of the underlying physical mechanism was developed by Radisvljevic et al. Using electrical transport measurements they were able to demonstrate that the dependence of mobility on temperature shows clear

evidence of the strong suppression of charged-impurity scattering in dual-gated devices with a 30nm HfO_2 top-gate dielectric vs. those devices without [54].

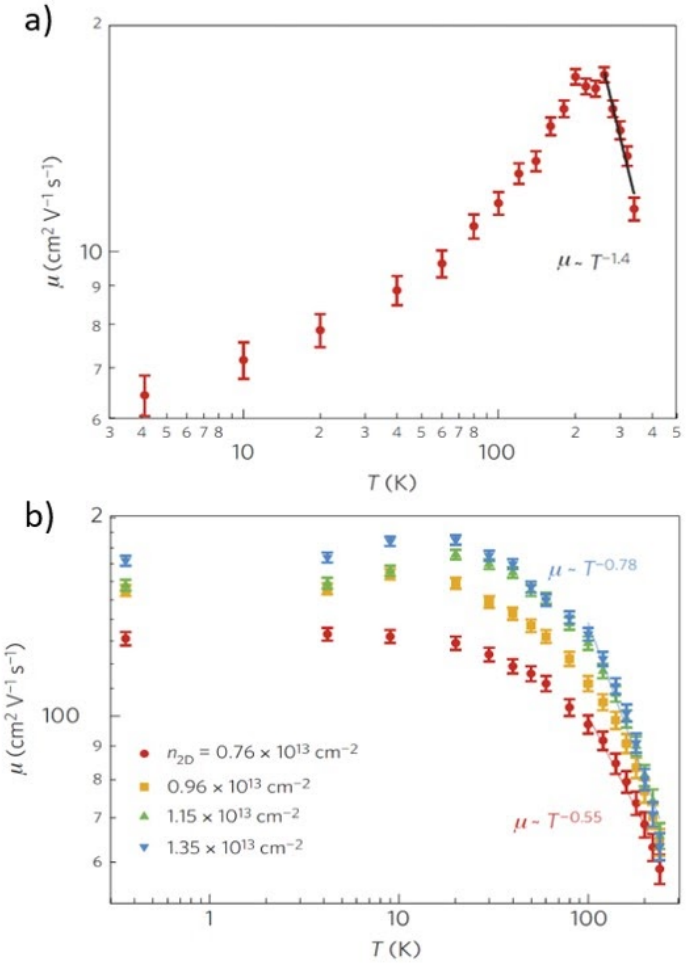

Figure 1.10) a) Plot of mobility vs.temperature showing a low-temperature regime indicative of charged impurity scattering limited transport and a phonon limited transport above ~200K. b) Plot of mobility for a HfO_2 dual gated device showing limited temperature dependence under 30K demonstrating screening of charge impurities. In addition, at higher temperatures the mobility dependence on temperature shows a strongly reduced value of the exponent demonstrating phonon mode quenching [54].

Utilizing this device architecture Radisavljevic et al. brought attention to MoS_2 and TMDs in the context of electronics, demonstrating negligible off-state current, *n*-type transport and room-temperature On/Off ratios of ~10^8 [39]. Integration of multiple devices on the same substrate was feasible due in part to the top-gaged geometry that allowed local control over conductivity in a manner comparable to commercial FETs. Similar monolayer MoS_2 FETs were later shown to exhibit maximal current densities of approximately 170 μA/μm at saturation which is more

than sufficient for devices integrated by copper vertical interconnect access pathways by more than 50x [55].

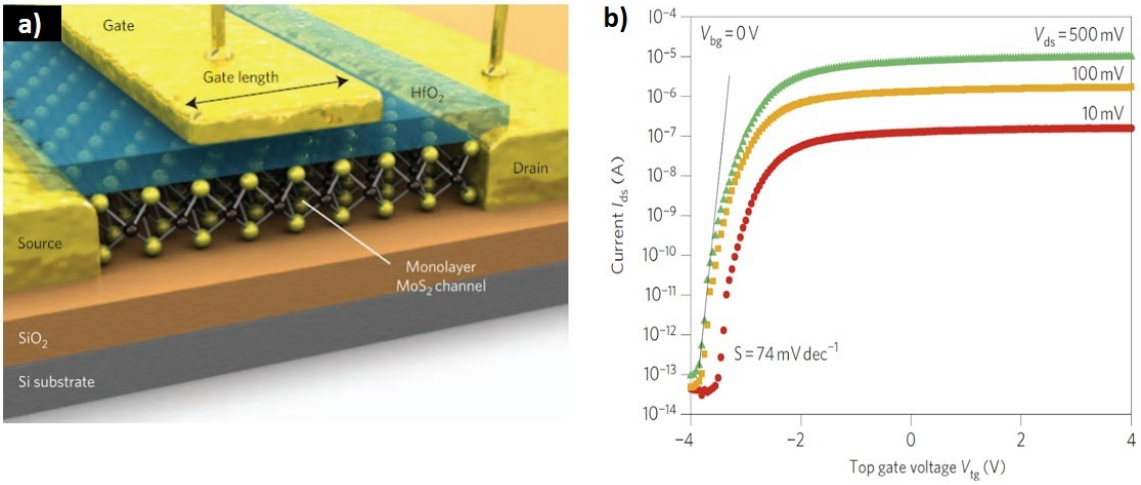

Figure 1.11) a) Schematic representation of a single layer top-gated MoS_2 FET [54]. (b) Device current vs. gate voltage. The current On/Off ratio is approximately 1×10^8. The device can be effectively turned off for gate voltages below −2 V and has a subthreshold slope of 74 mV/dec [30].

Work has been completed to evaluate the theoretical limits of MoS_2 based conventional FET performance. Y. Yoon et al. used non-equilibrium Green's function based quantum transport simulations and solved iteratively with Poisson's equation until self-consistency between charge density and electrostatic potential was achieved. Their work has indicated that excellent short channel behaviors such as DIBL as low as 10 mV/V and a subthreshold swing as low as 60 mV/decade could be achieved. While heavier electron effective mass ($m^* = 0.45m_o$) and lower mobilities appear to limit their applicability to high-performance applications when compared to state-of-the-art III-IV devices, large On/Off current ratios greater than 10^{10} make MoS_2 based FETs great candidates for applications that require exceptionally low standby power consumption [44].

To address the voltage scaling limitations that come with the inability to decrease the subthreshold slope, researchers have looked to use MoS_2 in TFET architectures. As discussed in section 1.2, TFETs fabricated from traditionally used materials such as Si, Ge and III-V semiconductors have suffered a number of limitations that have precluded their usability for high performance switching applications. Imperfections at the tunneling interface due to thickness variation, lattice mismatch, composition gradients caused by diffusion, and the random distribution of dopant atoms can reduce the band edge sharpness. These mechanisms can introduce trap states at the heterojunction interfaces and surfaces which, in practice, have limited the switching steepness of experimental devices [56].

TMDs may have the potential to overcome many of these critical limitations as they possess atomic flatness, form atomically sharp interfaces without any undesired diffusion, and various TMDs can be layered with minimal dislocation propagation due to lattice mismatch. Attempts have been made to take advantage of these properties such as in the work of Roy et al. [56] who fabricated vertical MoS_2/WSe_2 heterostructures using a dual gated device architecture that demonstrated band-to-band tunneling current.

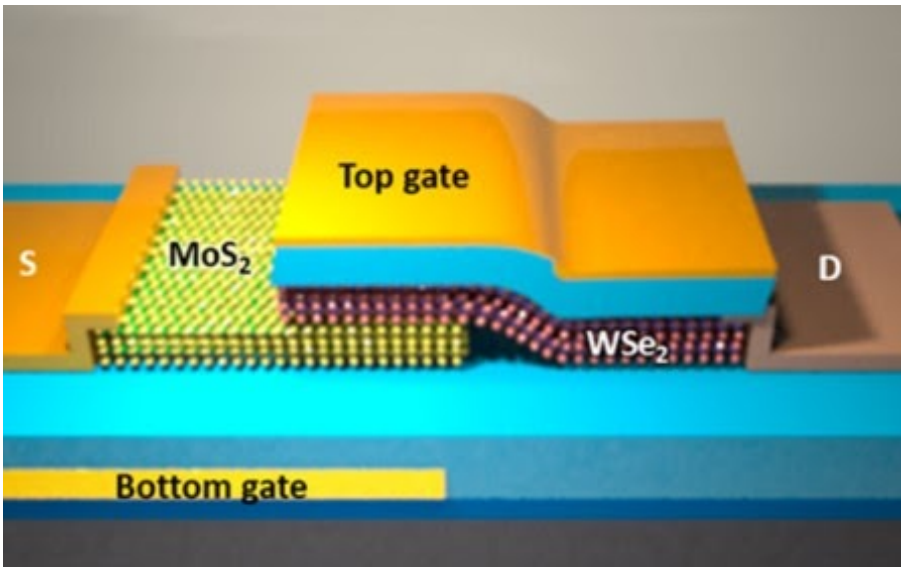

Figure 1.12) Three-dimensional schematic representation of a fabricated dual gated MoS_2/WSe_2 diode [56].

Though this device served as a good proof of concept, the approach suffered a number of performance limitations. A significant drawback of the device architecture was that it was not planar, relied on 8-10 layers of MoS_2 and 6-8 layers of WSe_2 which made it difficult to fabricate; its poor device compactness ultimately limited how it could be packaged into larger integrated circuits.

To address these challenges, Sarkar et al. [57] took a novel approach with a newly developed TFET device architecture that utilized a heterojunction between P-type Ge and intrinsic MoS_2. They named the device the atomically thin and layered semiconducting-channel tunnel-FET or ATLAS-TFET. It was the first planar TFET to demonstrate sub-thermionic subthreshold swing averaging 31 mV/decade over 4 decades. In addition, the device demonstrated a very low V_{DS} of 0.1V. Because of the device geometry, tunneling could occur over the entire overlap area and large tunneling currents could be achievable when compared to lateral junctions [57].

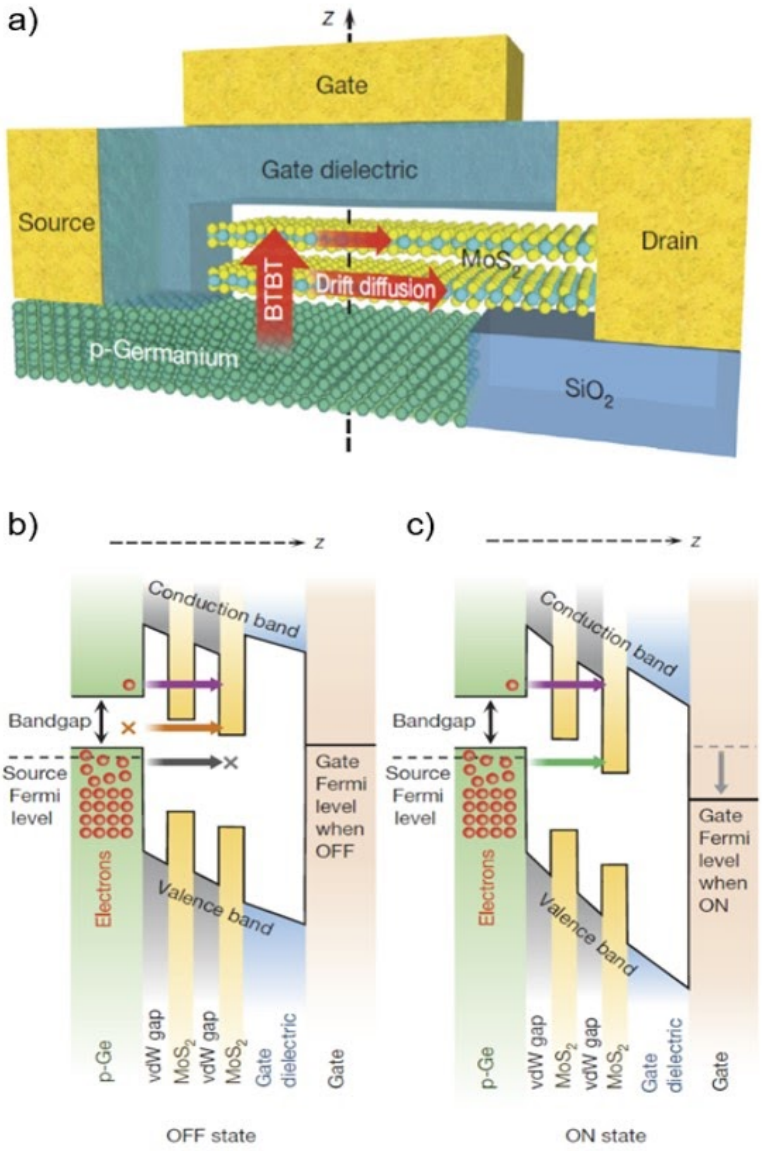

Figure 1.13) a) Schematic representation of the ATLAS-TFET device architecture utilizing MoS_2. b) Band diagram indicating limited tunneling current in the Off state. (c) Band diagram demonstrating how the reduction of gate Fermi level results in direct band-to-band tunneling between the p-Ge and MoS_2 layers [57].

From these demonstrations, it is clear that MoS_2 thin films in conjunction with new device architectures have the potential to enable next generation device scaling and low power applications.

1.5 Thesis Overview

Materials Science and Engineering is an interdisciplinary field of study focused on the design and discovery of new materials. Many introductory chapters of materials science textbooks help to describe the discipline using a schematic referred to as the "materials science tetrahedron" which places the core aspects of materials as they relate to science and engineering on the vertices of a tetrahedron. Those aspects include processing, structure, properties, and performance [58]. Their placement on the vertices helps elucidate the interrelated nature of these aspects and the relationship through which each aspect affects the other three.

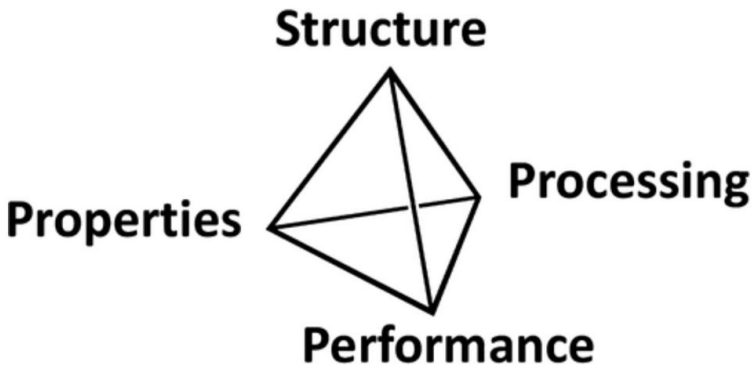

Figure 1.14) Depiction of the materials science tetrahedron showing the relationship between processing, structure, properties and performance [58].

Processing refers to the means by which the materials are synthesized or modified. Structure refers to the atomic composition, the bonding characteristics, and the spatial relationship of the atoms. In the case of less homogenous materials (not perfect single crystals), this consists of understanding different material domains and their relationships to one another such as grain structure, phases and defects present. Properties result from the structure and fall into a long list of interrelated categories such as electronic, mechanical, magnetic, optical, acoustic, thermal, chemical, etc. Finally, performance is a measure of the efficacy of a material for a particular application in relation to alternatives and is typically evaluated along the axes of an appropriate application specific figure-of-merit, cost, environmental and health impact, and scalability.

In many engineering focused investigations, the motivation for the synthesis of a particular material is driven by a desired application. Given the modern tools available for materials science and engineering, such as property and device performance investigation using computational methods, it is typical for materials selection and device architecture design to occur in a closely coupled iterative design

loop. Once these are established, the program focus moves toward the investigation of means of fabrication. This thesis is focused on the synthesis and characterization of large area crystalline MoS_2 thin films by pulsed laser deposition (PLD). Having established the motivation for MoS_2 thin films, this thesis is primarily centered around the processing and structure vertices of the materials science tetrahedron.

Chapter 1 introduces the historical context for the development of ICs and transistors, limitations to future development following established paradigms, and past work done to establish MoS_2 thin film based devices as an interesting avenue for investigation. Chapter 2 discusses the growth and characterization techniques used in the investigation. Chapter 3 covers past work to grow MoS_2 thin films, theoretical considerations, and results from attempts to establish repeatable high quality film growths by PLD. Chapter 4 focuses on results from characterization of the highest quality films grown during the investigation. Chapter 5 evaluates MoS_2 thin films in the context of a top-gated transistor. Finally, Chapter 6 provides a discussion about subsequent directions that may be explored to extend the work presented.

References

[1] K. Wong, "Archaeologists Take Wrong Turn, Find World's Oldest Stone Tools [Update]," *Scientific American Blog Network*, May 20, 2015. https://blogs.scientificamerican.com/observations/archaeologists-take-wrong-turn-find-world-s-oldest-stone-tools-update/ (accessed Apr. 13, 2020).

[2] H. J. Greenfield, "The Origins of Metallurgy: Distinguishing Stone from Metal Cut-marks on Bones from Archaeological Sites," *Journal of Archaeological Science*, vol. 26, no. 7, pp. 797–808, Jul. 1999, doi: 10.1006/jasc.1998.0348.

[3] S. Milisauskas, Ed., *European prehistory: a survey*. New York: Kluwer Academic/Plenum Publishers, 2002.

[4] C. Hu, *Modern semiconductor devices for integrated circuits*. Upper Saddle River, N.J: Prentice Hall, 2010.

[5] L. Liu, W. Tang, and P. Lai, "Advances in La-Based High-k Dielectrics for MOS Applications," *Coatings*, vol. 9, no. 4, p. 217, Mar. 2019, doi: 10.3390/coatings9040217.

[6] N. Arora, *Mosfet Modeling for VLSI Simulation: Theory and Practice*. World Scientific, 2007.

[7] G. E. Moore, "Cramming more components onto integrated circuits," *IEEE Solid-State Circuits Society Newsletter*, vol. 11, no. 3, pp. 33–35, Sep. 2006, doi: 10.1109/N-SSC.2006.4785860.

[8] D. Laws, "Moore's Law@50: 'The most important graph in human history,'" *Computer History Museum*. https://computerhistory.org/blog/moores-law50-the-most-important-graph-in-human-history/.

[9] S. Ellis, Y. Gao, and C. Wang, "TSMC Ready to Spend $20 Billion on its Most Advanced Chip Plant," *Bloomberg.com*, Oct. 06, 2017.

[10] K. M. Cham, S.-Y. Oh, J. L. Moll, K. Lee, P. Vande Voorde, and D. Chin, "Drain-Induced Barrier Lowering in Short Channel Transistors," in *Computer-Aided Design and VLSI Device Development*, K. M. Cham, S.-Y. Oh, J. L. Moll, K. Lee, P. Vande Voorde, and D. Chin, Eds. Boston, MA: Springer US, 1988, pp. 197–209.

[11] W. Muller, L. Risch, and A. Schutz, "Short-channel MOS transistors in the avalanche-multiplication regime," *IEEE Transactions on Electron Devices*, vol. 29, no. 11, pp. 1778–1784, Nov. 1982, doi: 10.1109/T-ED.1982.21026.

[12] V. K. Khanna, "Short-Channel Effects in MOSFETs," in *Integrated Nanoelectronics*, New Delhi: Springer India, 2016, pp. 73–93.

[13] G. W. Taylor, "Velocity-saturated characteristics of short-channel MOSFETs," *AT&T Bell Laboratories Technical Journal*, vol. 63, no. 7, pp. 1325–1404, Sep. 1984, doi: 10.1002/j.1538-7305.1984.tb00039.x.

[14] J. Keane and C. H. Kim, "Transistor Aging," *IEEE Spectrum*. https://spectrum.ieee.org/semiconductors/processors/transistor-aging (accessed Oct. 16, 2019).

[15] K. Rupp, "40 Years of Microprocessor Trend Data | Karl Rupp." https://www.karlrupp.net/2015/06/40-years-of-microprocessor-trend-data/ (accessed Jan. 04, 2020).

[16] L. Zhang, J. Huang, and M. Chan, "Steep Slope Devices and TFETs," in *Tunneling Field Effect Transistor Technology*, L. Zhang and M. Chan, Eds. Cham: Springer International Publishing, 2016, pp. 1–31.

[17] N. Jones, "How to stop data centres from gobbling up the world's electricity," *Nature*, vol. 561, pp. 163–166, Sep. 2018, doi: 10.1038/d41586-018-06610-y.

[18] K. Roy and S. Prasad, *Low-Power CMOS VLSI Circuit Design*, 1 edition. New York: Wiley-Interscience, 2000.

[19] Y. Liu, H. S. Pal, M. S. Lundstrom, D.-H. Kim, J. A. del Alamo, and D. A. Antoniadis, "Device Physics and Performance Potential of III-V Field-Effect Transistors," in *Fundamentals of III-V Semiconductor MOSFETs*, S. Oktyabrsky and P. Ye, Eds. Boston, MA: Springer US, 2010, pp. 31–50.

[20] J. W. Nilsson and S. Riedel, *Electric Circuits*, 10 edition. Boston: Pearson, 2014.

[21] A. P. Chandrakasan and R. W. Brodersen, *Low Power Digital CMOS Design*, 1995 edition. Boston: Kluwer Academic Publishers, 1995.

[22] L. L. Chang and L. Esaki, "Tunnel triode—a tunneling base transistor," *Appl. Phys. Lett.*, vol. 31, no. 10, pp. 687–689, Nov. 1977, doi: 10.1063/1.89505.

[23] A. M. Ionescu and H. Riel, "Tunnel field-effect transistors as energy-efficient electronic switches," *Nature*, vol. 479, no. 7373, pp. 329–337, Nov. 2011, doi: 10.1038/nature10679.

[24] K. K. Bhuwalka, J. Schulze, and I. Eisele, "Performance Enhancement of Vertical Tunnel Field-Effect Transistor with SiGe in the δp+ Layer," *Jpn. J. Appl. Phys.*, vol. 43, no. 7R, p. 4073, Jul. 2004, doi: 10.1143/JJAP.43.4073.

[25] G. Dewey *et al.*, "Fabrication, characterization, and physics of III–V heterojunction tunneling Field Effect Transistors (H-TFET) for steep sub-threshold swing," in *2011 International Electron Devices Meeting*, Dec. 2011, pp. 33.6.1-33.6.4, doi: 10.1109/IEDM.2011.6131666.

[26] A. C. Ford *et al.*, "Ultrathin body InAs tunneling field-effect transistors on Si substrates," *Appl. Phys. Lett.*, vol. 98, no. 11, p. 113105, Mar. 2011, doi: 10.1063/1.3567021.

[27] H. Lu and A. Seabaugh, "Tunnel Field-Effect Transistors: State-of-the-Art," *IEEE Journal of the Electron Devices Society*, vol. 2, no. 4, pp. 44–49, Jul. 2014, doi: 10.1109/JEDS.2014.2326622.

[28] W. Y. Choi, B.-G. Park, J. D. Lee, and T.-J. K. Liu, "Tunneling Field-Effect Transistors (TFETs) With Subthreshold Swing (SS) Less Than 60 mV/dec," *IEEE Electron Device Letters*, vol. 28, no. 8, pp. 743–745, Aug. 2007, doi: 10.1109/LED.2007.901273.

[29] J. Appenzeller, Y.-M. Lin, J. Knoch, and Ph. Avouris, "Band-to-Band Tunneling in Carbon Nanotube Field-Effect Transistors," *Phys. Rev. Lett.*, vol. 93, no. 19, p. 196805, Nov. 2004, doi: 10.1103/PhysRevLett.93.196805.

[30] A. A. Balandin *et al.*, "Superior Thermal Conductivity of Single-Layer Graphene," *Nano Lett.*, vol. 8, no. 3, pp. 902–907, Mar. 2008, doi: 10.1021/nl0731872.

[31] A. S. Mayorov *et al.*, "Micrometer-Scale Ballistic Transport in Encapsulated Graphene at Room Temperature," *Nano Lett.*, vol. 11, no. 6, pp. 2396–2399, Jun. 2011, doi: 10.1021/nl200758b.

[32] O. V. Yazyev and A. Kis, "MoS 2 and semiconductors in the flatland," *Materials Today*, vol. 18, no. 1, pp. 20–30, Jan. 2015, doi: 10.1016/j.mattod.2014.07.005.

[33] R. Tenne, L. Margulis, M. Genut, and G. Hodes, "Polyhedral and cylindrical structures of tungsten disulphide," *Nature*, vol. 360, no. 6403, pp. 444–446, Dec. 1992, doi: 10.1038/360444a0.

[34] Y. Feldman, E. Wasserman, D. J. Srolovitz, and R. Tenne, "High-Rate, Gas-Phase Growth of MoS2 Nested Inorganic Fullerenes and Nanotubes," *Science*, vol. 267, no. 5195, pp. 222–225, Jan. 1995, doi: 10.1126/science.267.5195.222.

[35] R. Tenne and A. K. Zettl, "Nanotubes from Inorganic Materials," in *Carbon Nanotubes*, vol. 80, M. S. Dresselhaus, G. Dresselhaus, and P. Avouris, Eds. Berlin, Heidelberg: Springer Berlin Heidelberg, 2001, pp. 81–112.

[36] Y. Frindt, R. F. A. D., "Physical properties of layer structures : optical properties and photoconductivity of thin crystals of molybdenum disulphide," *Proc. R. Soc. Lond. A*, vol. 273, no. 1352, pp. 69–83, Apr. 1963, doi: 10.1098/rspa.1963.0075.

[37] R. F. Frindt, "Single Crystals of MoS_2 Several Molecular Layers Thick," *Journal of Applied Physics*, vol. 37, no. 4, pp. 1928–1929, Mar. 1966, doi: 10.1063/1.1708627.

[38] K. S. Novoselov *et al.*, "Two-dimensional atomic crystals," *Proceedings of the National Academy of Sciences*, vol. 102, no. 30, pp. 10451–10453, Jul. 2005, doi: 10.1073/pnas.0502848102.

[39] B. Radisavljevic, A. Radenovic, J. Brivio, V. Giacometti, and A. Kis, "Single-layer MoS 2 transistors," *Nature Nanotech*, vol. 6, no. 3, pp. 147–150, Mar. 2011, doi: 10.1038/nnano.2010.279.

[40] Y. Ding, Y. Wang, J. Ni, L. Shi, S. Shi, and W. Tang, "First principles study of structural, vibrational and electronic properties of graphene-like MX2 (M=Mo, Nb, W, Ta; X=S, Se, Te) monolayers," *Physica B: Condensed Matter*, vol. 406, no. 11, pp. 2254–2260, May 2011, doi: 10.1016/j.physb.2011.03.044.

[41] K. K. Kam and B. A. Parkinson, "Detailed photocurrent spectroscopy of the semiconducting group VIB transition metal dichalcogenides," *J. Phys. Chem.*, vol. 86, no. 4, pp. 463–467, Feb. 1982, doi: 10.1021/j100393a010.

[42] K. F. Mak, C. Lee, J. Hone, J. Shan, and T. F. Heinz, "Atomically Thin MoS 2 : A New Direct-Gap Semiconductor," *Phys. Rev. Lett.*, vol. 105, no. 13, p. 136805, Sep. 2010, doi: 10.1103/PhysRevLett.105.136805.

[43] W. Jin *et al.*, "Direct Measurement of the Thickness-Dependent Electronic Band Structure of MoS 2 Using Angle-Resolved Photoemission Spectroscopy," *Phys. Rev. Lett.*, vol. 111, no. 10, p. 106801, Sep. 2013, doi: 10.1103/PhysRevLett.111.106801.

[44] Y. Yoon, K. Ganapathi, and S. Salahuddin, "How Good Can Monolayer MoS $_2$ Transistors Be?," *Nano Lett.*, vol. 11, no. 9, pp. 3768–3773, Sep. 2011, doi: 10.1021/nl2018178.

[45] R. Fivaz and E. Mooser, "Mobility of Charge Carriers in Semiconducting Layer Structures," *Phys. Rev.*, vol. 163, no. 3, pp. 743–755, Nov. 1967, doi: 10.1103/PhysRev.163.743.

[46] V. Podzorov, M. E. Gershenson, Ch. Kloc, R. Zeis, and E. Bucher, "High-mobility field-effect transistors based on transition metal dichalcogenides," *Appl. Phys. Lett.*, vol. 84, no. 17, pp. 3301–3303, Apr. 2004, doi: 10.1063/1.1723695.

[47] K. S. Novoselov, "Electric Field Effect in Atomically Thin Carbon Films," *Science*, vol. 306, no. 5696, pp. 666–669, Oct. 2004, doi: 10.1126/science.1102896.

[48] X. Li, J. T. Mullen, Z. Jin, K. M. Borysenko, M. Buongiorno Nardelli, and K. W. Kim, "Intrinsic electrical transport properties of monolayer silicene and MoS 2 from first principles," *Phys. Rev. B*, vol. 87, no. 11, p. 115418, Mar. 2013, doi: 10.1103/PhysRevB.87.115418.

[49] K. Kaasbjerg, K. S. Thygesen, and A.-P. Jauho, "Acoustic phonon limited mobility in two-dimensional semiconductors: Deformation potential and piezoelectric scattering in monolayer MoS 2 from first principles," *Phys. Rev. B*, vol. 87, no. 23, p. 235312, Jun. 2013, doi: 10.1103/PhysRevB.87.235312.

[50] W. Zhu *et al.*, "Electronic transport and device prospects of monolayer molybdenum disulphide grown by chemical vapour deposition," *Nat Commun*, vol. 5, no. 1, p. 3087, May 2014, doi: 10.1038/ncomms4087.

[51] P. Miró, M. Ghorbani-Asl, and T. Heine, “Spontaneous Ripple Formation in MoS_2 Monolayers: Electronic Structure and Transport Effects,” *Adv. Mater.*, vol. 25, no. 38, pp. 5473–5475, Oct. 2013, doi: 10.1002/adma.201301492.

[52] V. K. Sangwan, H. N. Arnold, D. Jariwala, T. J. Marks, L. J. Lauhon, and M. C. Hersam, “Low-Frequency Electronic Noise in Single-Layer MoS_2 Transistors,” *Nano Lett.*, vol. 13, no. 9, pp. 4351–4355, Sep. 2013, doi: 10.1021/nl402150r.

[53] B. W. H. Baugher, H. O. H. Churchill, Y. Yang, and P. Jarillo-Herrero, “Intrinsic Electronic Transport Properties of High-Quality Monolayer and Bilayer MoS_2,” *Nano Lett.*, vol. 13, no. 9, pp. 4212–4216, Sep. 2013, doi: 10.1021/nl401916s.

[54] B. Radisavljevic and A. Kis, “Mobility engineering and a metal–insulator transition in monolayer MoS2,” *Nature Mater*, vol. 12, no. 9, pp. 815–820, Sep. 2013, doi: 10.1038/nmat3687.

[55] D. Lembke and A. Kis, “Breakdown of High-Performance Monolayer MoS_2 Transistors,” *ACS Nano*, vol. 6, no. 11, pp. 10070–10075, Nov. 2012, doi: 10.1021/nn303772b.

[56] T. Roy *et al.*, “Dual-Gated MoS_2/WSe_2 van der Waals Tunnel Diodes and Transistors,” *ACS Nano*, vol. 9, no. 2, pp. 2071–2079, Feb. 2015, doi: 10.1021/nn507278b.

[57] D. Sarkar *et al.*, “A subthermionic tunnel field-effect transistor with an atomically thin channel,” *Nature*, vol. 526, no. 7571, pp. 91–95, Oct. 2015, doi: 10.1038/nature15387.

[58] C. J. Donahue, “Reimagining the Materials Tetrahedron,” *J. Chem. Educ.*, vol. 96, no. 12, pp. 2682–2688, Dec. 2019, doi: 10.1021/acs.jchemed.9b00016.

Chapter 2

Growth and Characterization Techniques

This chapter provides an overview of the growth and characterization techniques used in this investigation. In particular, pulsed laser deposition (PLD) is introduced as the primary growth technique employed in the synthesis of MoS_2 thin films. The working principles and use cases for characterization techniques including variations of X-ray diffraction, transmission electron microscopy, wave dispersive spectroscopy, atomic force microscopy and Raman spectroscopy are presented.

2.1 Thin Film Growth Techniques

There are a wide array of thin film growth techniques that have been developed over the last century and there are a number of ways to categorize them. One common approach is to organize the methods by the phase the film precursors are introduced to the thin film surface. Figure 2.1 depicts a taxonomy of techniques with a focus on gas/vacuum and solution based methods [1] as those are the most commonly employed for electronically, magnetically, or optically functional thin because of the higher degrees of thickness control typically afforded by the techniques. Among these families, vacuum or low pressure gas phase techniques have the benefit of a reduced density of unwanted atoms that could serve as contaminants. However, because of the need for a clean low pressure environment for film deposition, these techniques tend to be limited to smaller area depositions. There has been significant work to mitigate this drawback, such as the development of roll-to-roll processing whereby the substrate moves through a low pressure region where the thin film is deposited on a continuous basis or in extra large vacuum chambers where substrates are moved into the deposition chamber by way of air lock (as commonly used for LCD displays). Nevertheless, this family of techniques tends to be better suited to applications requiring small areas such as those in the semiconductor industry.

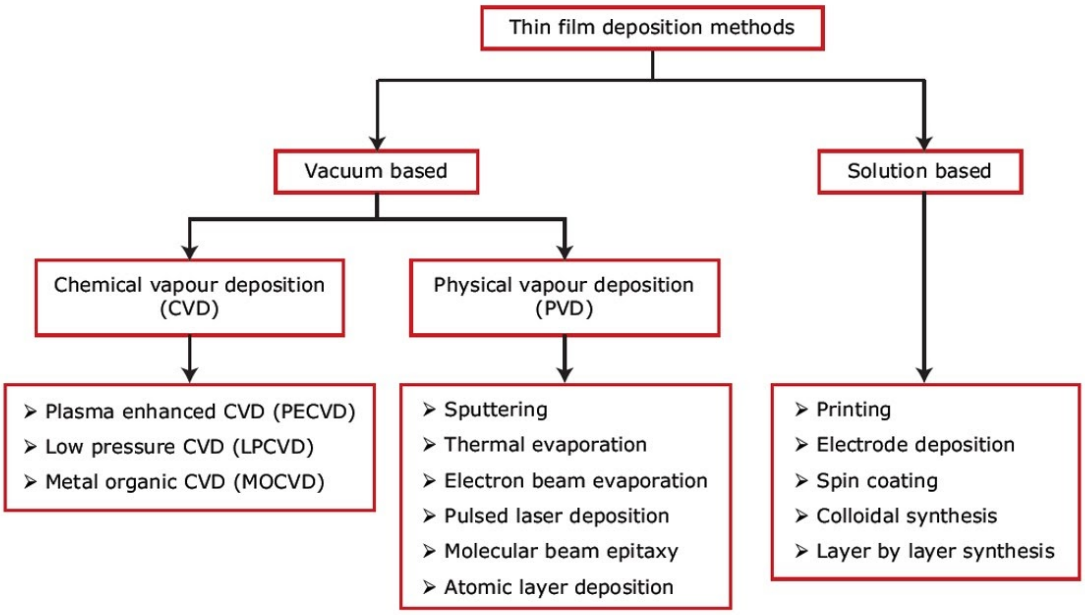

Figure 2.1) Taxonomy of thin film growth techniques with an emphasis on gas/vacuum and solution based methods [1].

Within the gas/vacuum family, techniques can be further categorized as physical vapor deposition (PVD) or chemical vapor deposition (CVD) techniques. In PVD techniques, the vapor is made up of atoms or molecules that condense on the substrate while CVD methods rely upon a chemical reaction on the substrate resulting in a thin film. Film quality during CVD is primarily controlled by the nature of the chemical reaction, reactant flow rates, reaction pressures and temperature, reactor geometry, and chemical species [2], [3]. Many types of reactions can be employed in CVD such as oxidation, reduction, pyrolysis, disproportionation, compound formation and reversible transfer [4].

Major advantages of the CVD family of techniques are their ability to grow both simple and complex compounds easily with high growth rates. Additionally, CVD has the ability to synthesize films of materials that could otherwise be difficult to deposit by PVD because of porosity of the source material [5]. CVD techniques can take advantage of selectivity of the chemical reaction to target only specific materials present on the substrate rather than covering it with a blanket layer. The nature of the deposition mechanism allows for conformal coating and because the source material flows in from an external source, it can be replaced without contamination risk of the growth environment which is valuable for high throughput applications. Drawbacks include the need for high substrate temperatures often higher than 600 deg C which can be unsuitable for structures already fabricated. Additionally, many

precursors or by-products may be toxic requiring extra steps to be taken to ensure safety [6].

PVD methods give great control for tuning the energy distribution of the vaporized species in transport that impinge on the substrate and reside on the surface before bonding thus giving control over the properties and structure of the films. PVD methods utilize different procedures to vaporize a precursor material from a solid or liquid phase that condenses after transport by diffusion through a diluted background gas or as a molecular beam; this must be on a suitable substrate below that of the melting point of the thin film phase desired [7, p. 298]. PVD has a number of advantages such as its ability to deposit almost any inorganic material and many organic materials using a pollution free deposition process. Since impinging atoms can be imbued with energy independent of thermal conduction from the substrate, many phases that are thermodynamically unfavorable can be synthesized where the vapor is essentially quenched at the substrate surface leading to the formation of kinetically limited metastable phases. As discussed with CVD, depending on the application, the line of sight nature of the PVD process can be considered an advantage or disadvantage. PVD suffers from larger capital costs and low deposition rates. Nevertheless, the excellent control that can be exhibited makes the family of techniques extremely popular for thin film synthesis in the materials research community [8].

The two main vaporization methods used for PVD are sputtering and thermal evaporation. Sputtering based PVD techniques transfer the solid target material into the vapor phase by the impulse transfer mechanism whereby ions with energies between a few eV to 1 keV are accelerated to the surface of the target. The resulting bombardment causes ion implantation, trapping and lattice destruction in the target material as well as the emission of sputtered atoms, ions or molecules in single or multi-step impulse transfer [7, p. 302]. Some of the most typical sputtering techniques include glow discharge diode sputtering, triode and RF-sputtering, ion beam sputtering and magnetron sputtering. Magnetron sputtering in particular is frequently used for applications requiring the high rate sputtering of metals as the configuration is able to generate a region of high plasma density near the target surface and subsequently high ion currents at moderate voltages [7, p. 305]. For the purpose of this investigation DC magnetron sputtering was used for the deposition of Ti/Au ohmic contacts.

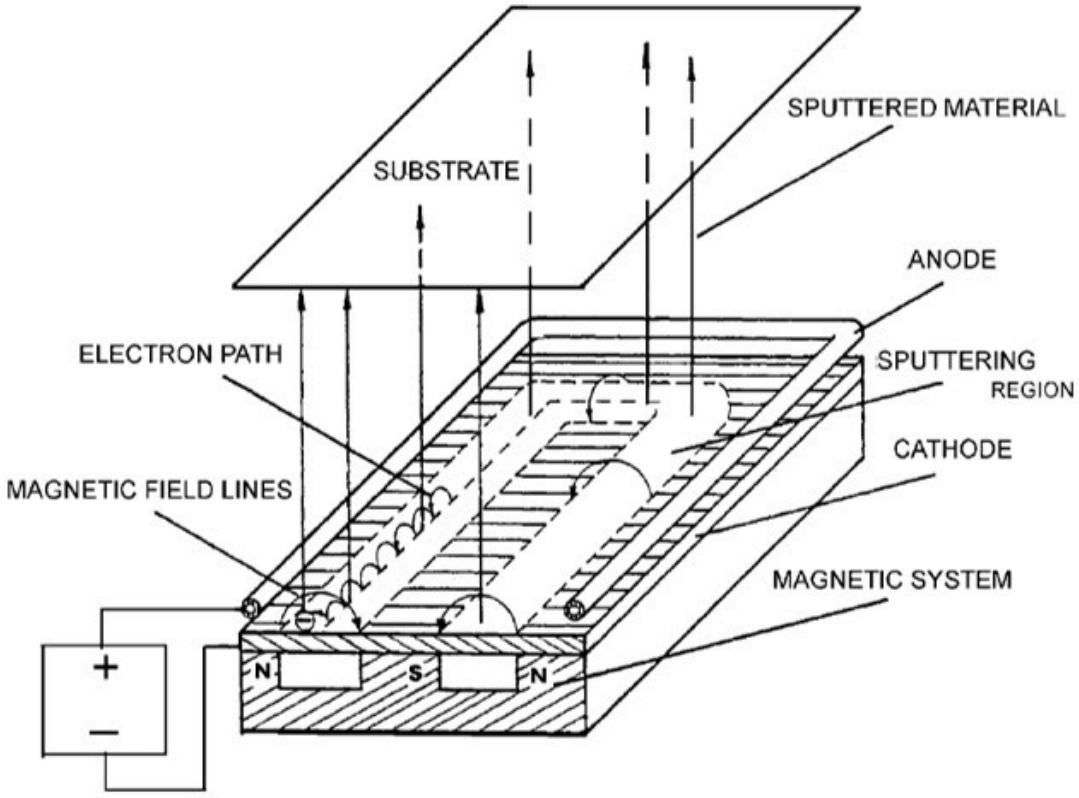

Figure 2.2) Schematic of magnetron sputtering [7, p. 306].

The other vaporization method employed by PVD techniques is thermal evaporation whereby a solid precursor for the thin film is melted and evaporated by a heating source. This family embodies a wide variety of techniques such as simple thermal evaporation using resistance heating sources, e-beam evaporation, ion plating, molecular beam epitaxy and laser ablation. The largest advantage of these methods is the reduction of contaminants that can occur in sputtering systems as a result of the trapping of plasma particles in the target, followed by short-circuiting filament growth which ejects target contaminants into the plasma and onto the substrate [9].

2.1.1 Pulsed Laser Deposition

The use of pulsed laser deposition (PLD) as a thin film growth technique has been explored since the advent of the laser [10], however it wasn't until the late 1980s that the technique experienced a resurgence. Due to its ability to reproducibly grow oxide films quickly and grow in-situ epitaxial high-temperature superconducting oxide thin films [11], PLD was readily adopted by the scientific community. The most attractive features of the PLD deposition process for growing complex oxides consisting of cations with a variety of vapor pressures that needed to react with an oxidant were stoichiometric transfer, the simplicity of initial setup, and the

generation of excited oxidizing species [12, p. 3]. Development of the PLD technique has continued to evolve into a mainstream method used for the deposition of semiconductors, metals, polymers, insulators and biological materials.

As shown in Figure 2.3, during the PLD process, a laser of sufficiently high energy density is pulsed. The generated light passes through a laser window into the vacuum system and is focused on a puck of material called the target. Each laser pulse ablates the target material generating a plume of plasma which is directed toward a substrate mounted on a heater. Commonly, an ultraviolet laser is used with a pulse width on the order of nanoseconds in order to create an ablation plume consisting primarily of low mass species such as atomic elements and diatomic molecules. In PLD, the density distribution of the plume generated is generally highly non-uniform with a distribution that, to the first order, follows $cos^n(\theta)$ where n can vary from 4 to 30 [12, p. 5]. To avoid the growth of non-uniform films, the target is rotated and/or the beam is rastered over the target surface.

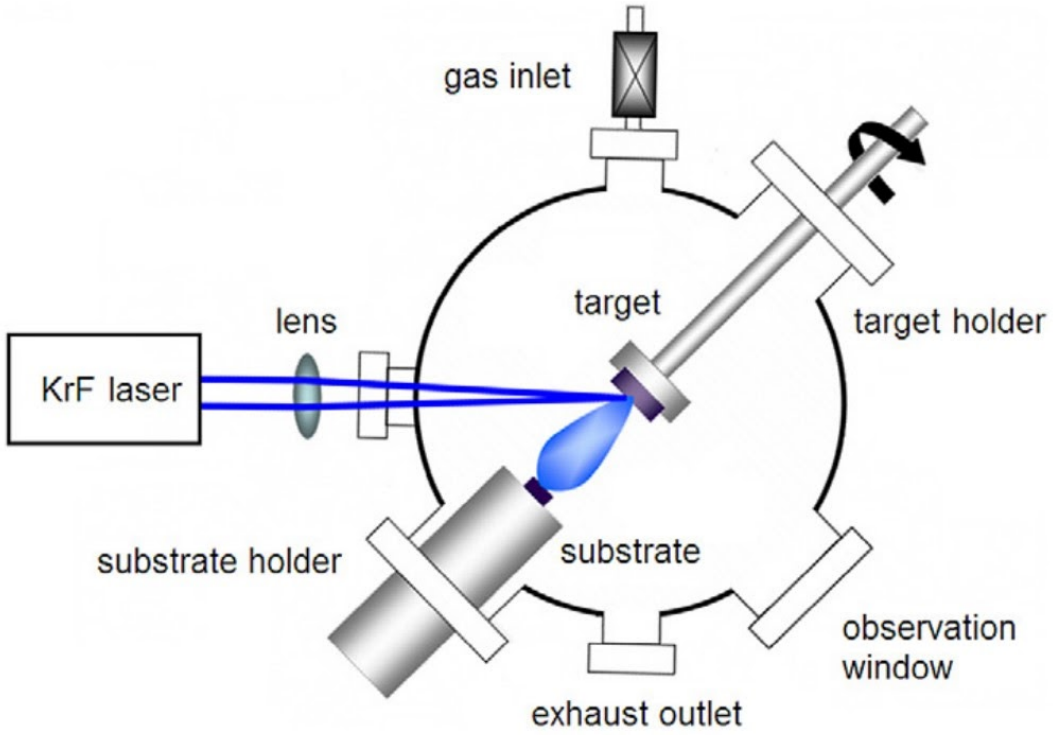

Figure 2.3) Schematic of a pulsed laser deposition system [13].

Control of stoichiometric transfer is one of the most important characteristics of PLD. The non-equilibrium ablation process enables this characteristic. At high laser fluences, absorption of the laser energy by the ablated species occurs leading to generation of a plasma at the target surface. The fluence of the laser is defined as the integral of the laser flux during the duration of the pulse and is the energy absorbed

by the target per unit area. As the laser fluence is decreased, an ablation threshold is reached below which the laser energy absorbed is less than the energy required to ablate the material. As the laser fluence is reduced further, low absorption of the laser energy by the target material results in local heating of the target causing the ejection of species due to thermal evaporation alone [12, p. 5]. The laser energy absorption process is dependent on the laser wavelength but less so on target material bandgap and electronic states because, at the high electric fields generated by the laser, dielectric breakdown occurs and all materials absorb a significant fraction of the radiation [14].

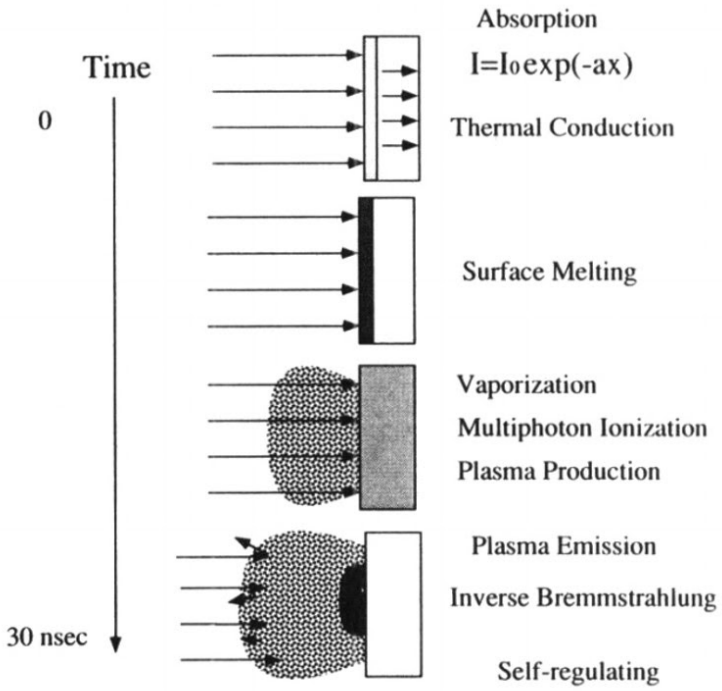

Figure 2.4) Schematic representation of high-powered laser-target interactions [14].

Figure 2.4 shows a schematic representation of the processes that occur during ablation. Initially, laser light is absorbed by the target surface which results in surface heating. The surface temperature is dependent on the laser pulse width, optical penetration depth of the laser frequency, and thermal diffusivity of the target. For small bandgap and metallic materials, the thermal diffusion distance is long compared to the optical absorption distance which reduces surface temperature. Surface heating is then succeeded by surface melting and evaporation. The high temperature occurring at the target surface causes thermionic emission of ions, electrons, neutral atoms and molecules that are dissociated. Further interaction between the laser pulse and the evaporated material leads to photoionization and the formation of a directed plasma above the surface. The plasma then absorbs energy from the radiation field

directly which induces further plasma heating as well as moderates additional laser light incident on the target surface [14].

Precise control of the ablation plume is required for the deposition of high quality materials. The ablation process requires target atoms to absorb more energy than their binding energies. Typical ablation thresholds are on the order of 0.1-1 J/cm^2 depending on the laser wavelength and the target material [12, p. 101]. For lasers with a pulse width of 10 ns intensities are between 10^8 and 10^9 W/cm^2 [15]. One major advantage for laser ablative techniques is this capability of the target to absorb higher energies locally than achievable through other thermal evaporation methods which leads to the generation of a plasma that is not dependent on the vapor pressures of the constituent cations [12, p. 6].

PLD regularly employs a background gas to reduce the kinetic energies of ablated materials and to help in the formation of high quality multi-cation thin films by providing an anion source. It has been observed by time resolved spectroscopy studies of ablation plume expansion that the presence of a background gas can reduce the kinetic energy of the plume from several hundred electron volts to much less than 1 eV [16]. Single crystal targets can be used to produce high quality thin films of the target material but new compositions and the formation of alloys can benefit from a process referred to as reactive PLD whereby the targets consist of the desired cations and the background gas acts as the anion source.

One potential disadvantage of PLD is the possible formation of subsurface damage as a result of the bombardment of the film with high energy ions and neutral species when a background gas is not utilized. The creation of interstitial defects can modulate the strain state by producing compressive strain in the films. As high energy particles impinge on the film, they collide with and transfer their kinetic energy to the underlying atoms in the film which displace them to interstitials. Additionally, recoil implantation can occur when surface atoms absorb the kinetic energy of the impinging atoms and are pushed deeper into the film. Compressive strains on the order of gigapascals have been reported [17].

Another potential drawback of PLD is the generation of micron sized particles that can occur during the ablation process when the penetration depth of the laser into the target is large at higher laser fluence. As the underlying target material is vaporized, a mini explosion occurs projecting the surrounding target material. If deposited on the substrate during the deposition process, laser particles can become embedded in the growing films, decreasing film quality and potentially destroying multilayer devices. The amount of laser particles present is affected by the density of the target material. Solutions to the problem of laser particles have commonly employed the use of velocity filters [18], line-of-sight shadow masks [19] and off-axis laser deposition [20].

Nevertheless, PLD remains an exceptional tool for thin film materials synthesis research because of the wealth of growth control parameters available, its ability to

grow metastable phases and superior thickness control. The specific PLD setup utilized as well as the growth conditions explored in this investigation are provided in detail in Chapter 3.

2.1.1.1 Target Preparation

The density of PLD targets is an important means to reduce formation of laser particles during the deposition process. As the target is vaporized, lower porosity targets have more regions for vapor to expand into. As the vapor is further heated, the internal pressure in these pores increases until it provides sufficient mechanical stress to cause the target to locally fracture, expelling a portion of the non-vaporized target toward the substrate as a laser particle.

To minimize target porosity, targets formed from feed powder sources are typically fabricated by a combination of pressing and sintering, especially in the case of ceramic and semiconductor materials. Unfortunately, when there is a discrepancy in the melting point of target components, sintering cannot be employed without meaningfully altering the composition of the target. In some cases this can be mitigated by firing the target in an ambient environment that minimizes outgassing. When this is not viable, targets can be formed by cold isostatic pressing (CIP) alone.

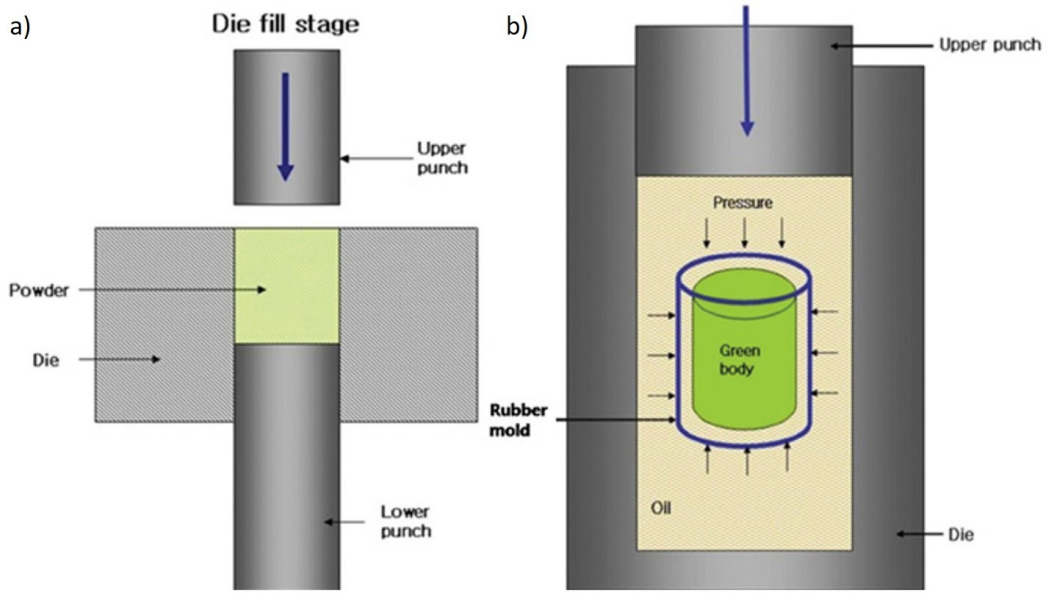

Figure 2.5) Schematic representation of a two-stage cold isostatic pressing process. a) Diagram of billet formation using a die press. b) Diagram of wet bag pressing of formed billet [21].

Sometimes referred to as hydrostatic pressing, CIP is a simple process which is capable of producing high-integrity billets with little dimensional distortion. The process is usually broken into two processes referred to as dry bag and wet bag [22].

For the formation of targets in this investigation, both processes were employed to form MoS_2 targets from Mo and S powder feeds. As seen in Figure 2.5 [21], powders sufficient to make a target of the desired composition were first filled into a die pressed and formed into a billet that was mechanically fragile and insufficient for laser ablation. The billet was then placed into a latex balloon serving as a wet bag and loaded into a wet bag press where it was suspended in oil. The surrounding oil was compressed to a pressure of 40,000 psi and held at the pressure for a few minutes. The resulting compact billets were used as PLD targets.

2.2 Characterization Techniques

In this investigation, a host of characterization techniques were used to gain understanding of the MoS_2 films grown. Compositional analysis was accomplished using wavelength-dispersive spectroscopy. Phase stabilization was probed with a series of techniques belonging to the x-ray diffractometry and transmission electron microscopy families. Further understanding of surface morphology was evaluated using atomic force microscopy. Finally, Raman spectroscopy was used to understand film thickness variation. This section provides an introduction to those techniques as well as discusses the specific setup used for the purposes of this investigation.

2.2.1 X-Ray Diffractometry

The discovery of X-rays by Wilhelm Roentgen in 1895 opened up a wide array of developments in many scientific fields [23]. New capabilities for the identification and characterization of crystalline materials through the technique of X-ray diffraction (XRD) were first developed by the work of von Laue, Knipping and Friedrich in 1912 [24]. Since then the list of available techniques that take advantage of X-rays has ballooned.

There are three primary families of X-ray experimental methods used in material science: X-ray radiography, X-ray fluorescence and XRD. X-ray radiography is a technique whereby X-rays are directed toward a sample and those that are transmitted through it are measured behind the sample, either by a modern detector or film plate. X-ray absorption is indicative of high atomic number elements and density and the local variation of absorption reveals information about the internal structure of the sample. X-ray fluorescence is used broadly as a chemical analysis technique. X-rays are used as a pump radiation source to excite a sample material which later relaxes and releases X-rays characteristics of elements present. The mechanism of this technique is discussed in more detail below [25].

XRD methods are based on the ability of crystalline materials to act as a diffraction grating for electromagnetic radiation with wavelengths similar to the periodic spacing of atoms. The well defined geometric conditions for diffraction allow for a precise study of the structure of crystalline phases. Captured diffraction patterns contain signal contributions from micro and macrostructural features of the sample.

Peak shape can provide information about microstrains and crystallite size while peak position can give insight into space group, lattice parameter, macrostresses and qualitative phase analysis [26]. Finally, peak intensity can give information relating to atomic position, occupancy, temperature factor as well as quantitative phase analysis [27, p. 81].

X-rays typically have wavelengths between 10^{-3} and 10^{1} nm. For standard materials characterization equipment, X-rays are generated by rotating anode or sealed tube sources whereby an electron beam is produced by thermionic emission of electrons from a tungsten filament or LiB_6 crystal in vacuum. The incident electrons induce X-ray generation through two mechanisms. The first is called bremsstrahlung radiation which is produced from the rapid deceleration of electrons and characteristically has a broad continuous distribution of wavelengths [28]. The second occurs as a result of the ionization of inner shell electrons of the impinged atoms. As atoms relax back toward their ground state, the holes present in the inner shell electrons are filled by outer shell electrons transitioning to a lower energy state. These transitions have characteristic energies which are well defined for all atoms as the outer and inner orbital state energies are also well defined, and the energy given up in the transition is emitted as electromagnetic radiation as depicted in Figure 2.6 (a). For transitions occurring between M, L and K shells, emissions typically reside in the X-ray band. A representative spectrum from a X-ray source can be seen in Figure 2.6 (b) and is a combination of a continuous bremsstrahlung spectrum and characteristic radiation [27, pp. 82–83]. XRD methods typically employ a monochromator or filter material which acts as a bandpass filter for the highest intensity characteristic X-ray produced by the source. For the purposes of this investigation a Panalytical X'Pert Pro diffractometer was used which employs a Cu X-ray source material with a monochromator to select $K_{\alpha 1}$ = 1.54059 Å.

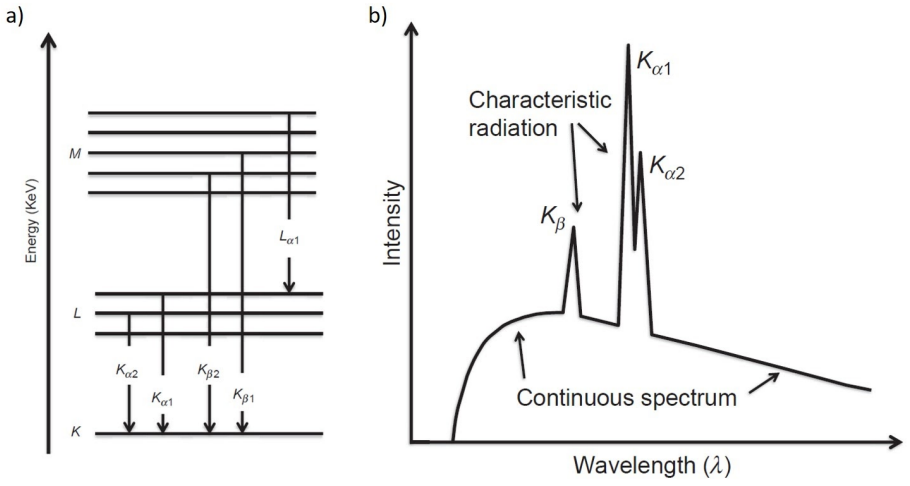

Figure 2.6 a) Schematic representation of characteristic X-ray emission from inner shell electron transitions. b) Plot of intensity vs. wavelength of the spectral distribution of X-ray radiation produced by a sealed-tube generator [27, pp. 82–83].

When X-ray photons impinge on a sample, a number of scattering and absorption interactions occur. Most importantly for the purpose of XRD, Rayleigh scattering takes place between incident X-rays and electrons surrounding the atomic nuclei of atoms present in the sample. In this interaction, scattering occurs elastically with the phase of the re-emitted photons being conserved relative to the incident photons and the incident X-ray beam is scattered in all directions by the sample. Because of the periodic nature of crystalline structure, however, scattered radiation will interfere constructively or destructively depending on the orientation of its wave vector relative to the lattice. These diffraction patterns can be studied to understand the crystal structure of the material [27, p. 84]. The geometric interpretation of diffraction was first given by Lawrence and William Henry Bragg in 1913 by Bragg's Law which takes the form of

$$n\lambda = 2d_{hkl}sin(\theta)$$

where n is the order of diffraction, λ is the wavelength of the incident beam, d_{hkl} is the lattice spacing and θ is the angle of the diffracted beam [29]. A schematic representation of this condition can be seen in Figure 2.7 [25].

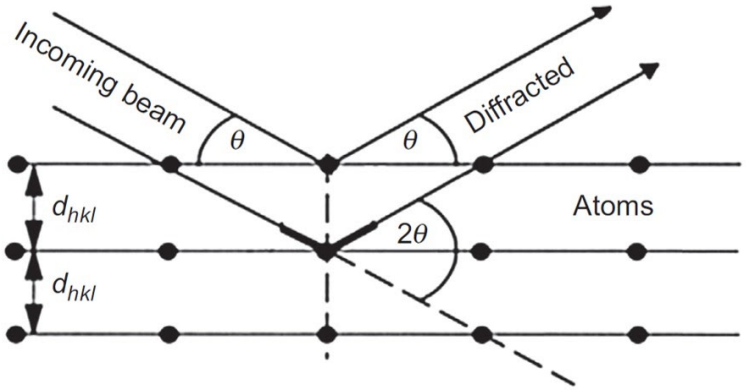

Figure 2.7) Schematic of the geometrical relationship for diffraction from lattice planes following Bragg's Law [25].

Bragg-Brentano geometry, where the distance between the sample and detector remains constant for all θ angles, was used along with a 2Theta-Omega goniometer where the X-ray source remains fixed while the sample and detector are moved [27, p. 90]. A schematic of the Eulerian cradle configuration used in this investigation can be seen in Figure 2.8 [30]. 2Theta-Omega scans were used to probe out-of-plane film texture while a qualitative analysis of crystallite size, crystal defects, and inhomogeneous strains were probed by determining peak widths via omega scans. Finally, of the line scans executed (where a single coordinate parameter is scanned), phi scans helped to reveal in-plane film inhomogeneities.

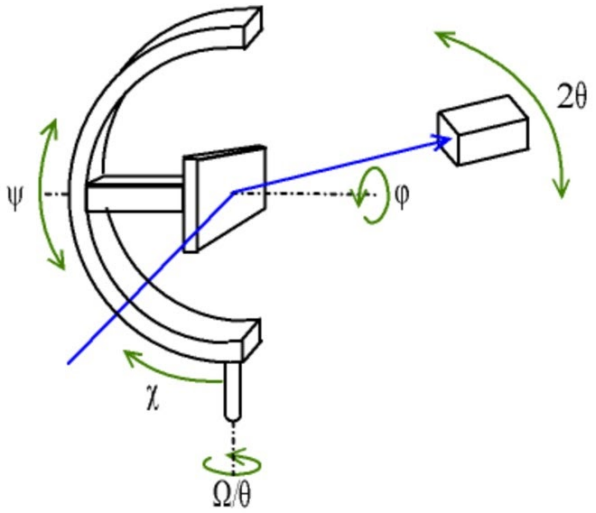

Figure 2.8) Diagram of a Eulerian cradle used to control orientation of samples in modern XRD systems [30].

X-ray reflectivity (XRR) is a technique where the intensity of an X-ray beam reflected from the sample of a surface is monitored relative to the intensity of the incident beam. XRR is a specular reflectivity technique where the incident and reflected angles are the same. If the interface between the film and substrate is sharp and there is variation in the index of refraction for the substrate and film material, reflection from both the air-film interface and film-substrate interface will occur according to the Fresnel equations based on Snell's Law. Reflected rays will constructively or destructively interfere with each other depending on the phase relationship of the two rays. As a result, when the incident angle is scanned, there will be peaks and troughs in reflected intensity with the angular periodicity being dependent on the film thickness. Thickness, surface roughness and the film's density profile can be quantified from XRR scans. Figure 2.9 (a) shows the typical geometric relationships for XRR setup as well as the ray optics which lead to the development of interference fringes. Figure 2.9 (b) shows a representative XRR scan where thickness fringes can be observed [31].

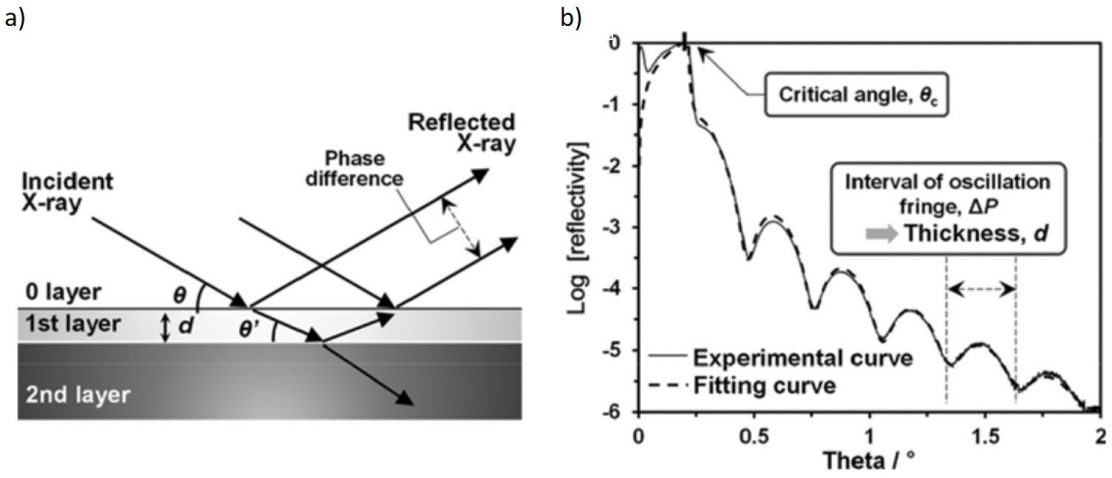

Figure 2.9 a) Representative ray diagram of the configuration used for XRR analysis. b) A representative XRR profile and fitting profile calculated by software [31].

Reciprocal space mapping (RSM) is an XRD technique whereby reciprocal space is locally probed in high fidelity. This is of particular importance for highly perfect crystals which only diffract over small angular ranges. A more thorough evaluation of reciprocal space can provide insights on microstructural deviations and crystalline imperfections such as twinning, relaxation studies and more sensitive phase identification [32]. RSMs are typically used to help with the exposition of peak broadening, peak overlap or peak displacement that may be observed in high resolution line scans.

2.2.2 Wave Dispersive Spectroscopy

As discussed with the typical methods used to generate X-rays for XRD methods, electrons of sufficient energy interacting with a sample lead to the production of X-rays from the elements present. These characteristic X-rays act as an elemental fingerprint for the elements present in a sample. While energy dispersive spectroscopy (EDS) aims to measure the broad X-ray spectrum radiating from a sample in a scanning electron microscope (SEM) or electron probe micro-analyzer (EPMA) [33, p. 336], wave dispersive spectroscopy (WDS) has significantly higher spectral resolution and potential for quantitative analysis.

WDS utilizes an analytical crystal with precisely characterized lattice spacing as a diffraction grating for the incident X-rays. In operation, the WDS system will maintain a constant takeoff angle between the X-rays emanating from the sample and the analytical crystal. When X-rays impinge on the analytical crystal at a specific angle θ, only wavelengths that satisfy Bragg's Law will be diffracted to the detector. The relative positions and angles of the detector to the analytical crystal enable the

wavelength required for diffraction to be scanned [33, p. 273]. Figure 2.10 shows a comparison of the resolution of EDS and WDS spectral lines for a MoS_2 sample [34].

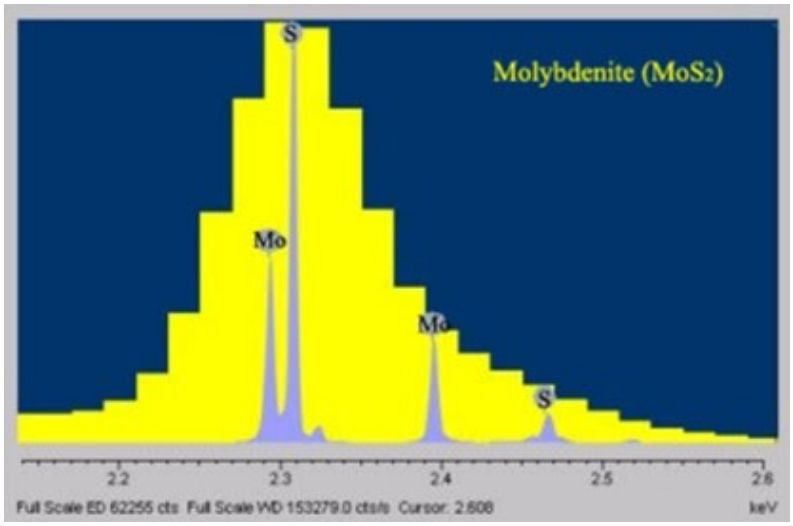

Figure 2.10) Plot of X-ray spectrum captured by EDS (yellow) and WDS (blue) for a MoS_2 sample [34].

As the appropriate geometry for a specified energy range is scanned, X-ray intensities for each resolved wavelength range are counted and a spectrum is collected. With knowledge of the beam current as well as a reference database containing standard values for characteristic X-rays for elements of interest, the X-ray intensities can be correlated to an atomic percentage of elements in the sample. Intensities must be corrected for a host of different interdependent element specific effects related to atomic number (Z), absorption (A), and fluorescence (F) before a final ZAF corrected estimate can be provided [35]. For this investigation, a JEOL JSM-6490LV SEM equipped with Oxford INCAx-Sight was used to evaluate film composition.

2.2.3 Transmission Electron Microscopy

Transmission electron microscopy (TEM) is a technique employed for materials characterization that uses a beam of electrons transmitted through a specimen and collected on a detector to form micrographs. The Rayleigh criterion for visible light microscopy states that the smallest distance that can be resolved, δ, is given by

$$\delta = \frac{0.61\,\lambda}{\eta\, sin(\theta)}$$

where λ is the wavelength of the radiation, η is the refractive index and θ is the semi-angle of collection of the magnifying lens [36, p. 5]. In 1924, Louis de Broglie postulated the wave nature of electrons and provided his famous equation relating the wavelength of an electron to its energy:

$$\lambda = \frac{h}{p}$$

where h is Planck's constant and p is the electron's momentum [37]. With accelerating voltages in the 100-500 keV range, it can be shown that electron wavelengths on the picometer scale are achievable which are much smaller than the diameter of an atom. Consequently, the TEM takes advantage of this property along with the ability of magnetic or electrostatic fields to act as optics to shape and direct the electron beam to generate an image and characterize materials at very small distance scales.

A TEM system is comprised of a number of components including an electron emission source, electron lenses, apertures, a specimen stage and manipulator and detectors all housed in the vacuum system. The electron emission source usually takes the form of a pointed tungsten filament or a LaB_6 crystal. This element thermionically emits electrons following Richardson's Law and is heated to achieve sufficient current density [36, p. 74]. Tungsten is typically used because of its refractory nature and LaB_6 because of its very low work function. The element is biased in order to pump emitted electrons into the microscope column. Electron lenses act to focus and shape the electron beam mimicking optical lenses using electrostatic or magnetic fields [38]. Apertures exclude portions of the electron beam some defined distance away from the optic axis and typically take the form of a small metallic disc that is not electron transparent. The specimen stage is typically a small metallic grid which prevents overcharging of the sample by providing a conduction path for excess electrons while remaining electron transparent. The stage allows translation and rotation of the sample to enable the region of interest to be adequately inserted into the beam path and stay oriented. CMOS detectors have been used as a superior means of electron detection since 2005 [39]. Finally, the entire beam column and all the components discussed above are housed in vacuum which is essential to extend the mean free path of electrons in the beam, reduce scattering and supporting clear signal formation and capture.

As discussed in the XRD section describing X-ray generation, an impinging electron beam has a diverse set of interactions with a sample. Beyond bremsstrahlung and characteristic X-Ray generation, there are elastically and inelastically scattered electrons, Auger electrons, backscattered electrons, secondary electrons, etc. Figure 2.11 schematically represents these various interactions [36, p. 7].

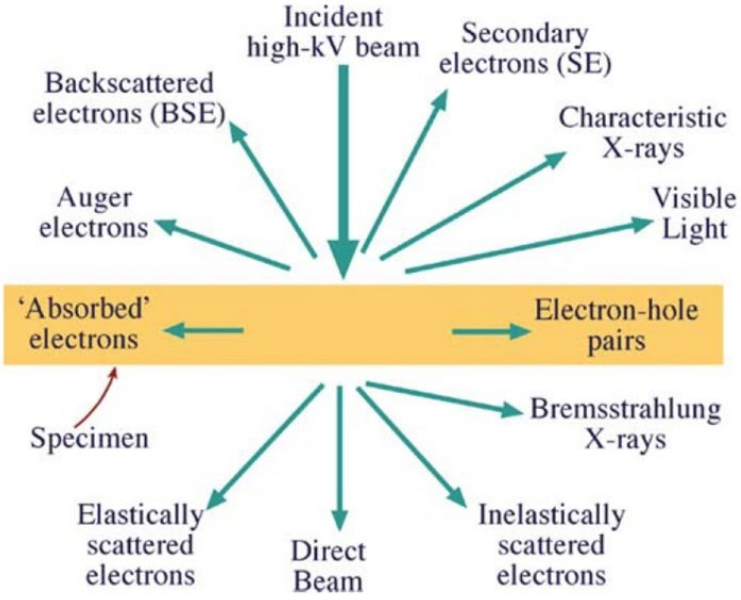

Figure 2.11) Diagram depicting the types of measurable signals generated from the interaction of an electron beam of sufficient energy with a sample [36, p. 7].

TEM has a large array of possible operating modes including scanning TEM (STEM), conventional imaging, diffraction and spectroscopy. Within the category of conventional imaging, there is further variation in image contrast mechanisms. Depending on the mode variation, contrast can be generated as a result of differences in atomic number, crystal structure, crystal orientation, phase of transmitted electrons, and sample thickness. TEM produces many different characteristic signals all localized with sub-nanometer scale spatial resolution. When these techniques are used in combination, TEM emerges as an extremely powerful tool for qualitative and quantitative materials analysis and characterization. For the purposes of this investigation, TEM characterization was limited to conventional imaging using the phase contrast mechanism, selected area electron diffraction (SAED) and high-angle annular dark-field imaging (HAADF) utilizing an aberration corrected FEI Titan 80-300 TEM/STEM operating at an acceleration voltage of 300 kV.

In the mode of image formation using the phase contrast mechanism, contrast arises from the interaction of the electron wave with itself at the image plane. Above the sample, the incident electrons can be approximated as plane waves. When they interact with the sample, electrons are attracted to the electrostatic potentials of the atomic nuclei and are funneled along the atom columns of the lattice. Concordantly, electrons are diffracted from adjacent atomic columns. Consequently, the electron exit wave from the sample at a given position is a superposition of the plane waves and diffracted beams where the amplitude peaks beneath the atomic columns [40]. The relationship between the exit wave and image wave captured by the detector is a function of the aberrations in the TEM imaging lenses and the limiting aperture

described by the contrast transfer function. Figure 2.12 (a) shows a ray diagram of TEM optics generating the phase contrast mechanism [41] while Figure 2.12 (b) depicts an example image.

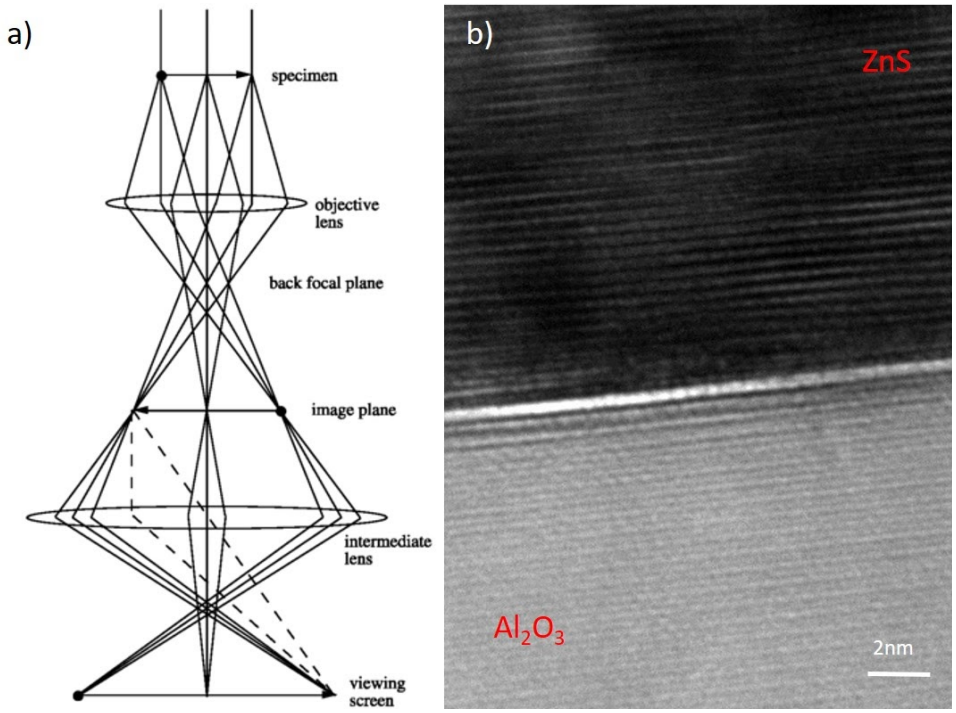

Figure 2.12) a) Ray diagram of TEM configuration required for the phase contrast mechanism [41]. b) A phase contrast TEM micrograph of ZnS on Al_2O_3.

SAED is a technique effective for the characterization of the crystallinity, crystal structure, and orientation of a sample by electron diffraction. As incident electrons interact with the periodic structure of a crystalline material, the atoms of the sample act like a diffraction grating. For this technique, diffracted electrons are collected by the TEM optics to form a diffraction pattern at the imaging plane. Figure 2.13 (a) shows a ray diagram of TEM optics for SAED while Figure 2.13 (b) depicts an example of a selected area diffraction pattern. The technique is referred to as "selected area" electron diffraction because of the ability to control the area irradiated with the electron beam and from which the diffraction pattern is formed. This is very powerful because it allows for the direct characterization of different phases that may be present in a sample without having to significantly alter the TEM's configuration. By selecting two adjoining crystalline regions, their relative crystallographic orientation can be characterized. Unlike XRD methods, SAED is able to obtain diffraction patterns for areas as small as several hundred nanometers in diameter [42].

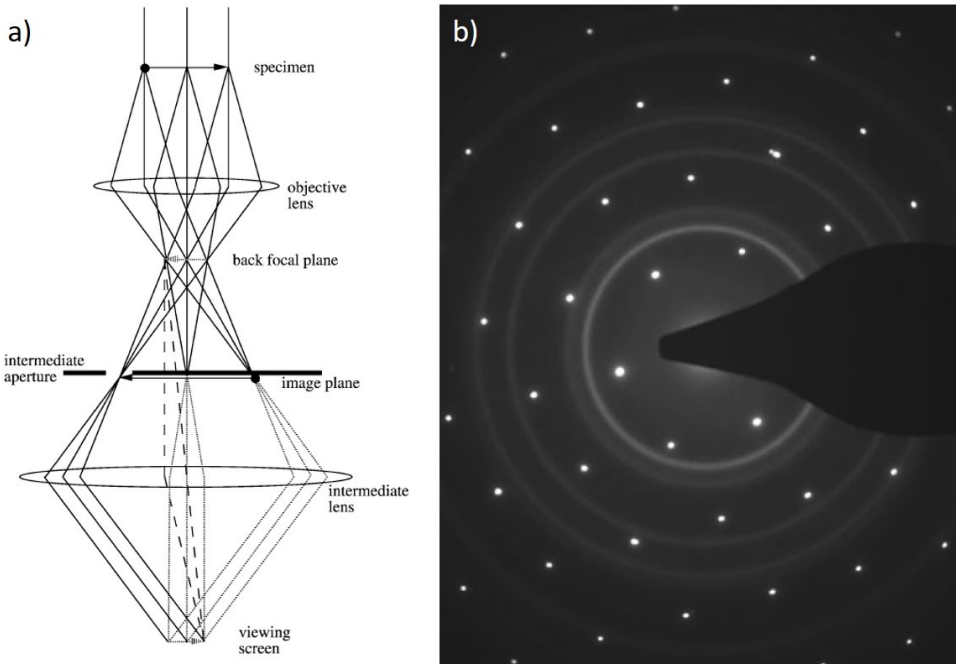

Figure 2.13) a) Ray diagram of TEM configuration required for SAED where the intermediate aperture is placed around a bright spot in the image plane [41]. b) A representative SAED pattern of polycrystalline Au thin film on crystalline Si [42].

HAADF is a scanning transmission electron microscopy technique (STEM) which produces dark field images where contrast is generated by the collection of electrons incoherently scattered at high angles from the atomic nuclei of atoms in the sample via Rutherford scattering. The electron probe is rastered over the sample surface allowing information to be progressively collected. Image resolution for this technique is principally a result of the size of the electron probe and, if spherical aberration of the objective lens can be minimized, very high resolution images can be obtained. An annular detector is used which allows for more electrons to be collected than could otherwise pass through an objective aperture [43].

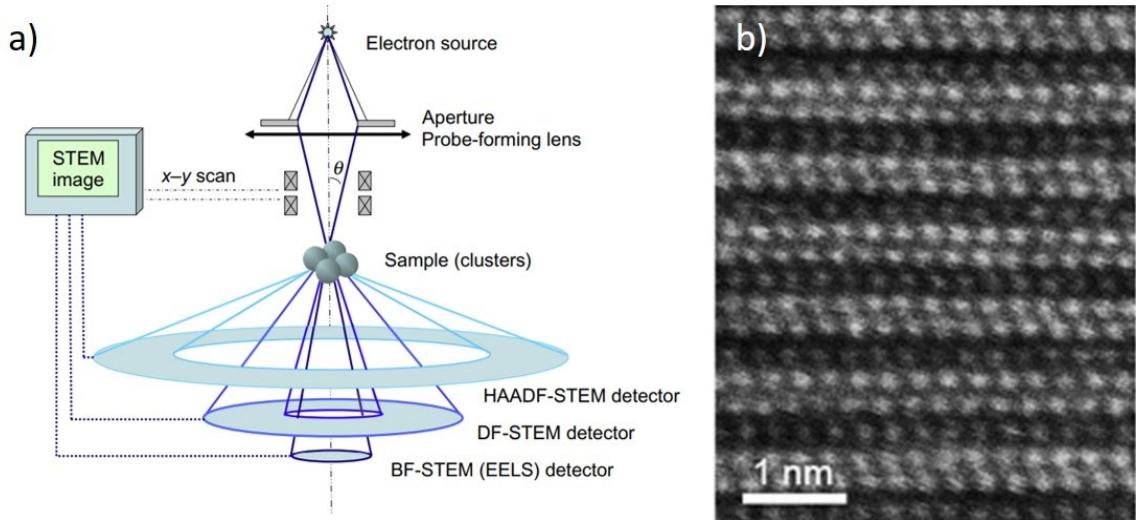

Figure 2.14) a) Schematic diagram of the configuration used for HAADF STEM measurements [44]. b) A representative image of Cr_2AlC thin films captured using HAADF STEM [45].

Scattering angle for Rutherford scattering is very dependent on the atomic number as heavier elements have nuclei with greater charge leading to more prominent electrostatic interactions with the electron beam. As a result, contrast approximately scales with $Z^{1.6-1.7}$ and the technique is very useful in identifying regions of high Z elements in a lower Z matrix [43]. Typically, scattering angles greater than 5 degs along with a small distance between the sample and detector are used to minimize the overlap between Bragg diffracted and Rutherford scattered electrons. Since the central beam is not needed for the HAADF-STEM measurement it can be used in tandem for electron energy loss spectroscopy or brightfield imaging. Figure 2.14 (a) depicts a schematic representation of the typical imaging geometry used for HAADF [44] while Figure 2.14 (b) shows an example image of Cr_2AlC thin films captured using HAADF-STEM [45]. From the image, Z dependent contrast makes identification of elements easy by visual inspection.

2.2.4 Atomic Force Microscopy

Atomic force microscopy (AFM) is a family of techniques that rely on the mechanical interaction between a probe and sample surface to gather information pertaining to the topology and mechanical properties of the sample. An AFM system in its most basic configuration is composed of a small cantilever which has a sharp tip on its free end, a sample stage capable of translational movement in three dimensions, and a detector which records the deflection of the cantilever. During operation, the sample stage moves the sample in relation to the cantilever tip resulting in the scanning or rasterization of the tip over the sample surface.

In practice, displacement of the tip can be precisely measured by piezoresistive methods, piezoelectric methods, or interferometry. However, the most common

method relies on bouncing light from a laser diode off of a thin metallic foil layer present on the top surface of the cantilever and measuring movement of the reflected beam with a position sensitive photodiode (PSPD). The small changes in the cantilever deflection angle are multiplied by the distance the reflected beam travels resulting in a larger, detectable change in beam position on the PSPD [46]. Figure 2.15 (a) shows a schematic of a typical AFM setup while Figure 2.15 (b) shows a representative AFM scan of a Cr alloyed ZnSe thin film.

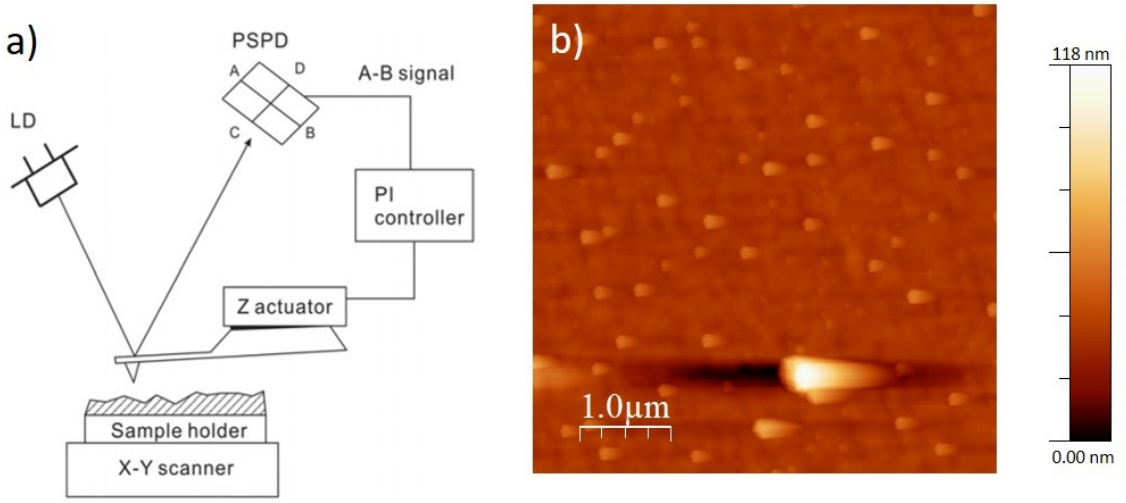

Figure 2.15) a) Schematic diagram of a configuration used for AFM [46]. b) AFM micrograph of a Cr alloyed ZnSe thin film.

In tapping mode, an additional cantilever oscillator made of a piezoelectric material is used to induce vibration with amplitude greater than 100 nm at the cantilever tip. When the AFM scans the sample, the amplitude change is measured and used as a feedback signal to control the amplitude. Tapping mode was a major development in AFM which allows for high resolution scans without the issues resulting from tip friction, adhesion or electrostatic forces which can damage the tip or sample and distort the captured micrograph [47]. For the purposes of this investigation, a Veeco-DI equipped with a Nanoscope IV Controller and silicon tip from MikroMasch was used in tapping mode for surface roughness measurements.

2.2.5 Raman Spectroscopy

Raman spectroscopy is a technique whereby the vibrational or rotational modes of atomic bonds can be probed using the inelastic scattering of light. First predicted in 1923 by Adolf Smekal, the Raman effect was experimentally observed initially in 1928 by Sir Chandrasekhara Venkata Raman [48]. Incident light reflected by a sample can be shifted down (Stokes) or up (anti-Stokes) in energy before being collected. The magnitude of this shift corresponds to the polarization potential of the electrons in the material to form an induced dipole moment in the external electric

field of the monochromatic light. The difference in wavelength between the incident photons and photons collected after the scattering process correlate to the energy imbued to or from molecular transition in the rotational or vibrational modes of the material [49].

Raman spectroscopy possesses a number of advantages over IR absorption spectroscopy such as the ability to use a probe wavelength that is not absorbed by the surrounding medium, scattering symmetry selection rules which allow otherwise forbidden photon only transitions during the absorption process, and small probe areas. However, due to Raman scattering being less probable than Rayleigh scattering, the signal is weaker and the method sensitivity is lower. In addition, fluorescence of the sample may further contaminate the Raman signal [48]. Figure 2.16 shows an example of Raman spectra collected for a composition series of $Cu_xZn_{1-x}S$ films demonstrating the presences of Cu_2S at Cu concentrations above X=10.

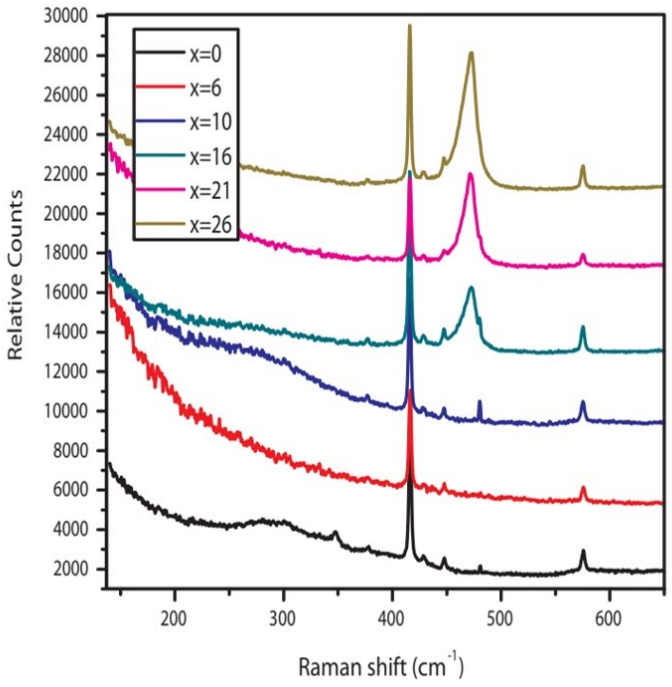

Figure 2.16) An example of Raman spectra collected for a composition series of $Cu_xZn_{1-x}S$ films demonstrating the presences of Cu_2S at Cu concentrations above X=10.

A typical configuration for Raman spectroscopy consists of a light source, optics to direct the beam to a suitably sized optical probe and to collect the scattered light, filters to remove the probe frequency, and a sensitive detector. Usually, a monochromatic continuous wave laser source is used as the optical probe. A beam

splitter acts to direct the beam along the optical axis of the objective (focusing and collecting) lens. The Raman scattered light next passes through a notch or optical long-pass filter to remove the probe wavelength and improve the detector sensitivity to the surrounding wavelengths.

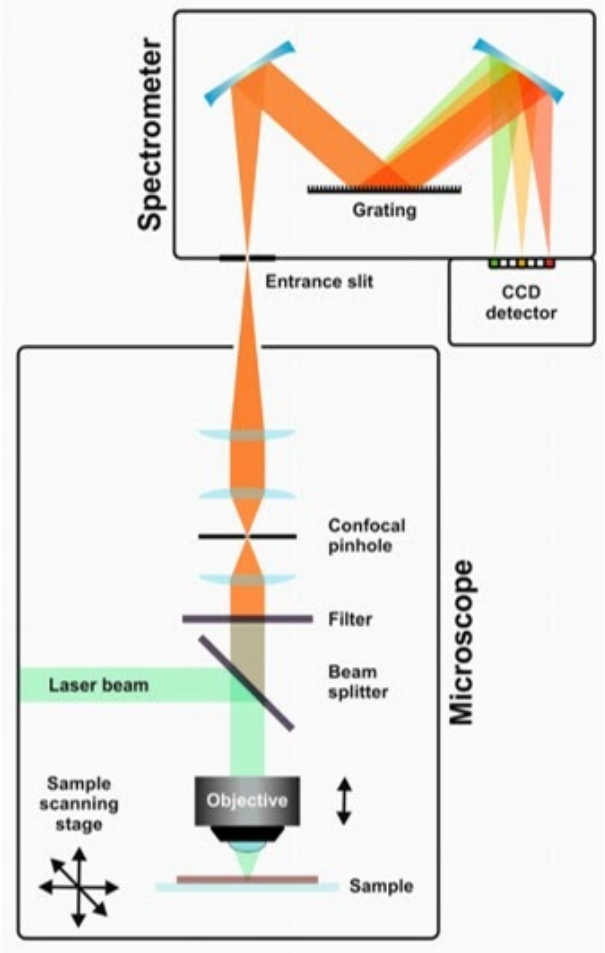

Figure 2.17) A schematic of a representative Raman spectroscopy setup [49].

The detector in modern Raman spectroscopy systems consists of various types of CCDs optimized for different wavelength ranges. The scattered beam impinges on a diffraction grating which enables the reflected beam to be spatialized depending on wavelength such that the most appropriate CCD sensor can be used for the different portions of the spectrum. Figure 2.17 shows a schematic of a representative Raman spectroscopy setup. Also, as the optical probe can be scanned over the sample, spectra can be captured at each point of interest larger than a few square microns on sample thin films [49]. For this investigation Raman measurements were executed using a JYHoriba LabRAM with an excitation wavelength of 472.95 nm.

References

[1] S. Vyas, "A Short Review on Properties and Applications of Zinc Oxide Based Thin Films and Devices : ZnO as a promising material for applications in electronics, optoelectronics, biomedical and sensors," *Johnson Matthey Technology Review*, vol. 64, no. 2, pp. 202–218, Apr. 2020, doi: 10.1595/205651320X15694993568524.

[2] H. Pedersen and S. D. Elliott, "Studying chemical vapor deposition processes with theoretical chemistry," *Theor Chem Acc*, vol. 133, no. 5, p. 1476, May 2014, doi: 10.1007/s00214-014-1476-7.

[3] S. Kommu, G. M. Wilson, and B. Khomami, "A Theoretical/Experimental Study of Silicon Epitaxy in Horizontal Single-Wafer Chemical Vapor Deposition Reactors," *J. Electrochem. Soc.*, vol. 147, no. 4, p. 1538, 2000, doi: 10.1149/1.1393391.

[4] O. Oluwatosin Abegunde *et al.*, "Overview of thin film deposition techniques," *AIMS Materials Science*, vol. 6, no. 2, pp. 174–199, 2019, doi: 10.3934/matersci.2019.2.174.

[5] K. Seshan, Ed., *Handbook of thin-film deposition processes and techniques: principles, methods, equipment, and applications*, 2nd ed. Norwich, N.Y: Noyes Publications, 2002.

[6] K. Choy, "Chemical vapour deposition of coatings," *Progress in Materials Science*, vol. 48, no. 2, pp. 57–170, 2003, doi: 10.1016/S0079-6425(01)00009-3.

[7] E. Steinbeiss, "Thin Film Deposition Techniques (PVD)," in *Spin Electronics*, vol. 569, M. Ziese and M. J. Thornton, Eds. Berlin, Heidelberg: Springer Berlin Heidelberg, 2001, pp. 298–315.

[8] A. S. H. Makhlouf and I. Tiginyanu, Eds., *Nanocoatings and ultra-thin films: technologies and applications*. Oxford: Woodhead Publishing, 2011.

[9] G. S. Selwyn, C. A. Weiss, F. Sequeda, and C. Huang, "Particle contamination formation in magnetron sputtering processes," *Journal of Vacuum Science & Technology A: Vacuum, Surfaces, and Films*, vol. 15, no. 4, pp. 2023–2028, Jul. 1997, doi: 10.1116/1.580674.

[10] H. M. Smith and A. F. Turner, "Vacuum Deposited Thin Films Using a Ruby Laser," *Appl. Opt.*, vol. 4, no. 1, p. 147, Jan. 1965, doi: 10.1364/AO.4.000147.

[11] A. Inam *et al.*, "As-deposited high T_c and J_c superconducting thin films made at low temperatures," *Appl. Phys. Lett.*, vol. 53, no. 10, pp. 908–910, Sep. 1988, doi: 10.1063/1.100155.

[12] R. Eason, Ed., *Pulsed Laser Deposition of Thin Films: Applications-Led Growth of Functional Materials*, 1 edition. Hoboken, N.J: Wiley-Interscience, 2006.

[13] S. C. Xu *et al.*, "Direct synthesis of graphene on any nonmetallic substrate based on KrF laser ablation of ordered pyrolytic graphite," *Laser Phys. Lett.*, vol. 11, no. 9, p. 096001, Sep. 2014, doi: 10.1088/1612-2011/11/9/096001.

[14] J. Cheung and J. Horwitz, "Pulsed Laser Deposition History and Laser-Target Interactions," *MRS Bull.*, vol. 17, no. 2, pp. 30–36, Feb. 1992, doi: 10.1557/S0883769400040598.

[15] E. G. Gamaly, A. V. Rode, and B. Luther-Davies, "Ultrafast ablation with high-pulse-rate lasers. Part I: Theoretical considerations," *Journal of Applied Physics*, vol. 85, no. 8, pp. 4213–4221, Apr. 1999, doi: 10.1063/1.370333.
[16] K. R. Chen *et al*., "Mechanisms affecting kinetic energies of laser-ablated materials," *Journal of Vacuum Science & Technology A: Vacuum, Surfaces, and Films*, vol. 14, no. 3, pp. 1111–1114, May 1996, doi: 10.1116/1.580278.
[17] D. P. Norton, C. Park, J. D. Budai, S. J. Pennycook, and C. Prouteau, "Plume-induced stress in pulsed-laser deposited CeO2 films," *Appl. Phys. Lett.*, vol. 74, no. 15, pp. 2134–2136, Apr. 1999, doi: 10.1063/1.123780.
[18] E. V. Pechen, A. V. Varlashkin, S. I. Krasnosvobodtsev, B. Brunner, and K. F. Renk, "Pulsed-laser deposition of smooth high- T_c superconducting films using a synchronous velocity filter," *Appl. Phys. Lett.*, vol. 66, no. 17, pp. 2292–2294, Apr. 1995, doi: 10.1063/1.113264.
[19] Z. Trajanovic, S. Choopun, R. P. Sharma, and T. Venkatesan, "Stoichiometry and thickness variation of YBa2Cu3O7−x in pulsed laser deposition with a shadow mask," *Appl. Phys. Lett.*, vol. 70, no. 25, pp. 3461–3463, Jun. 1997, doi: 10.1063/1.119201.
[20] B. Holzapfel, B. Roas, L. Schultz, P. Bauer, and G. Saemann-Ischenko, "Off-axis laser deposition of $YBa_2Cu_3O_{7-\delta}$ thin films," *Appl. Phys. Lett.*, vol. 61, no. 26, pp. 3178–3180, Dec. 1992, doi: 10.1063/1.107951.
[21] Y.-J. Seo, K.-D. Yun, H.-S. Kim, and S.-W. Park, "Adaptability of zirconia core fabricated by cold isostatic pressing," *J Korean Acad Prosthodont*, vol. 48, no. 2, p. 143, 2010, doi: 10.4047/jkap.2010.48.2.143.
[22] K. J. Morris, "Cold Isostatic Pressing," in *Concise Encyclopedia of Advanced Ceramic Materials*, Elsevier, 1991, pp. 84–88.
[23] W. C. Röntgen, "Ueber eine neue Art von Strahlen," *Ann. Phys.*, vol. 300, no. 1, pp. 12–17, 1898, doi: 10.1002/andp.18983000103.
[24] W. Friedrich, P. Knipping, and M. Laue, "Interferenzerscheinungen bei Röntgenstrahlen," *Ann. Phys.*, vol. 346, no. 10, pp. 971–988, 1913, doi: 10.1002/andp.19133461004.
[25] L. Spieß, G. Teichert, R. Schwarzer, H. Behnken, and C. Genzel, *Moderne Röntgenbeugung*. Wiesbaden: Vieweg+Teubner, 2009.
[26] R. E. Dinnebier and S. J. L. Billinge, Eds., *Powder Diffraction: Theory and Practice*. Cambridge: Royal Society of Chemistry, 2008.
[27] J. Epp, "X-ray diffraction (XRD) techniques for materials characterization," in *Materials Characterization Using Nondestructive Evaluation (NDE) Methods*, Elsevier, 2016, pp. 81–124.
[28] L. H. Schwartz and J. B. Cohen, *Diffraction from Materials*. Berlin, Heidelberg: Springer Berlin Heidelberg, 1987.
[29] W. L. Bragg, "The diffraction of short electromagnetic waves by a crystal," *Proceedings of the Cambridge Philosophical Society*, vol. 17, p. 43, 1913.
[30] "Texture (crystalline)," *Wikipedia*. Apr. 17, 2020, [Online]. Available: https://en.wikipedia.org/w/index.php?title=Texture_(crystalline)&oldid=951469333.

[31] S. Ogawa and I. Takahashi, "Glass Transition of Ultrathin Sugar Films Probed by X-Ray Reflectivity," in *Carbohydrate*, M. Caliskan, I. H. Kavakli, and G. C. Oz, Eds. InTech, 2017.
[32] P. F. Fewster, "Reciprocal space mapping," *Critical Reviews in Solid State and Materials Sciences*, vol. 22, no. 2, pp. 69–110, Jun. 1997, doi: 10.1080/10408439708241259.
[33] J. I. Goldstein *et al.*, "X-Ray Spectral Measurement: WDS and EDS," in *Scanning Electron Microscopy and X-Ray Microanalysis*, Boston, MA: Springer US, 1992, pp. 273–339.
[34] D. Henry and J. Goodge, "Wavelength-dispersive spectroscopy (WDS)," *Geochemical Instrumentation and Analysis*. https://serc.carleton.edu/research_education/geochemsheets/wds.html.
[35] A. Boekestein, A. M. Stadhouders, A. L. H. Stols, and G. M. Roomans, "A comparison of ZAF-correction methods in quantitative X-ray microanalysis of light-element specimens," *Ultramicroscopy*, vol. 12, no. 1–2, pp. 65–68, Jan. 1983, doi: 10.1016/0304-3991(83)90306-6.
[36] D. B. Williams and C. B. Carter, *Transmission electron microscopy: a textbook for materials science*, 2nd ed. New York: Springer, 2008.
[37] R. P. Feynman, *QED: the strange theory of light and matter*. Princeton, N.J: Princeton University Press, 1985.
[38] J. Orloff, Ed., *Handbook of charged particle optics*. Boca Raton, Fla: CRC Press, 1997.
[39] A. R. Faruqi, R. Henderson, M. Pryddetch, P. Allport, and A. Evans, "Erratum to: 'Direct single electron detection with a CMOS detector for electron microscopy,'" *Nuclear Instruments and Methods in Physics Research Section A: Accelerators, Spectrometers, Detectors and Associated Equipment*, vol. 566, no. 2, p. 770, Oct. 2006, doi: 10.1016/j.nima.2006.07.013.
[40] P. Geuens and D. Van Dyck, "The S-state model: a work horse for HRTEM," *Ultramicroscopy*, vol. 93, no. 3–4, pp. 179–198, Dec. 2002, doi: 10.1016/S0304-3991(02)00276-0.
[41] B. Fultz and J. Howe, "The TEM and Its Optics," in *Transmission Electron Microscopy and Diffractometry of Materials*, Berlin, Heidelberg: Springer Berlin Heidelberg, 2013, pp. 59–115.
[42] W. F. Tivol, "Selected Area Electron Diffraction and its Use in Structure Determination," *Micros. Today*, vol. 18, no. 4, pp. 22–28, Jul. 2010, doi: 10.1017/S1551929510000441.
[43] K. Sohlberg, T. J. Pennycook, W. Zhou, and S. J. Pennycook, "Insights into the physical chemistry of materials from advances in HAADF-STEM," *Phys. Chem. Chem. Phys.*, vol. 17, no. 6, pp. 3982–4006, 2015, doi: 10.1039/C4CP04232H.
[44] Z. Li, "Scanning Transmission Electron Microscopy Studies of Mono- and Bimetallic Nanoclusters," in *Frontiers of Nanoscience*, vol. 3, Elsevier, 2012, pp. 213–247.

[45] Y. T. Chen, D. Music, L. Shang, J. Mayer, and J. M. Schneider, "Nanometre-scale 3D defects in Cr2AlC thin films," *Sci Rep*, vol. 7, no. 1, p. 984, Dec. 2017, doi: 10.1038/s41598-017-01196-3.
[46] Y. Seo and W. Jhe, "Atomic force microscopy and spectroscopy," *Rep. Prog. Phys.*, vol. 71, no. 1, p. 016101, Jan. 2008, doi: 10.1088/0034-4885/71/1/016101.
[47] I. Schmitz, M. Schreiner, G. Friedbacher, and M. Grasserbauer, "Tapping-Mode AFM in Comparison to Contact-Mode AFM as a Tool for in Situ Investigations of Surface Reactions with Reference to Glass Corrosion," *Anal. Chem.*, vol. 69, no. 6, pp. 1012–1018, Mar. 1997, doi: 10.1021/ac9607020.
[48] D. J. Gardiner, P. R. Graves, and H. J. Bowley, Eds., *Practical Raman spectroscopy*. Berlin ; New York: Springer-Verlag, 1989.
[49] T. Schmid and P. Dariz, "Raman Microspectroscopic Imaging of Binder Remnants in Historical Mortars Reveals Processing Conditions," *Heritage*, vol. 2, no. 2, pp. 1662–1683, Jun. 2019, doi: 10.3390/heritage2020102.

Chapter 3

Growth of MoS_2 Thin Films by PLD

This chapter provides an overview of past efforts to synthesize MoS_2 thin films followed by a detailed discussion of considerations for MoS_2 thin film synthesized by PLD. Such factors include thermodynamic and kinetic considerations for the Mo-S material system, target composition, substrate selection as well as other growth conditions. Finally, growth results are presented along with efforts to establish repeatable growth conditions for highly crystalline thin films.

3.1 Past Work to Synthesize MoS_2 Thin Films

In order to materialize the promise of MoS_2 and other TMD materials, appropriate methods for large area growth must be developed. To that end, extensive efforts have been applied recently following different approaches such as intercalation assisted exfoliation [1]–[3], micromechanical exfoliation using scotch tape [4]–[7], liquid exfoliation [8], hydrothermal synthesis [9], thermolysis of single precursors [10], [11], chemical vapor deposition [12], vapor solid epitaxy [13], and physical vapor deposition [14]–[16].

Some of the first examples of the synthesis of MoS_2 were the growth of bulk crystals by chemical vapor transport. In 1964 Schäfer developed an approach whereby a transport agent such as iodine or bromine was mixed with purified MoS_2 in the powder form in a sealed quartz ampoule [17]. The ampoule was then placed inside a zone electric furnace with a temperature gradient established along the tube length.

Liquid exfoliation was first established in 1986 by Per Joensen et al. [18]. This method involved soaking a crystal or powder of a layered TMD in a solution of butyllithium and hexane which resulted in the intercalation of Li between layers. The solution would then be mixed with water causing the release of gaseous hydrogen which would force the layers apart. While this procedure is promising for producing large quantities of exfoliated monolayer and few-layer nanosheets on the order of grams, the subsequent material is in the 1T metallic phase and needs to be

heated above 300 deg C to reform to the 2H semiconducting polytype. Finally, the use of lithium requires that the method be executed in an inert atmosphere.

Alternative liquid exfoliation approaches have relied on the ultrasonication of MoS_2 in surfactant solutions or organic solvents where the surface tension of the solutions have good correspondence with the surface energy of the material being exfoliated [19], [20]. While the resulting films created by this process are typically small flakes limiting their applicability to electronics or photonic applications where large continuous layers with few defects are required, liquid exfoliation can result in large quantities of monolayer dispersions that can be deposited by spin coating or inkjet printing.

Since first used for the production of graphene [21], micromechanical cleavage has largely been the workhorse synthesis method for 2D TMD research. Few-layer to mono-layer thick flakes of TMDs can be easily extracted from bulk crystals by applying an adhesive tape to the surface of the bulk crystal followed by peeling and applying the adhesive tape now containing the 2D material to a clean substrate free of organic residue. High quality large flakes measuring 10s of microns suitable for integration into devices for further research are identifiable by optical interference techniques [22]. Major benefits of this technique include its simplicity and extremely low cost for research purposes compared to others, requiring only an optical microscope and scotch tape. These benefits have led to its wide adoption throughout the research community; however, its lack of scalability inevitably limits this technique to research purposes.

With growing interest in 2D MoS_2, work to identify large-area growth techniques has continued to intensify. Chemical vapor deposition relying on the thermal decomposition of ammonium tetrathiomolybdate heated in the presence of sulphur developed by Liu et al. showed promising results but faced difficulty in achieving monolayer growth [23].

This control was later achieved by a number of groups utilizing an approach based on the evaporation and reaction of solid precursors of MoO_3 and S in the vapor phase [12], [24], [25]. In this method MoO_3 and S powders were placed in a furnace and heated under inert gas flow at atmospheric pressure. This technique resulted in monolayer single-grain domains approximately 100 micrometers wide and with electronic and optical properties similar to exfoliated samples, however, the flakes had poor in-plate orientation control.

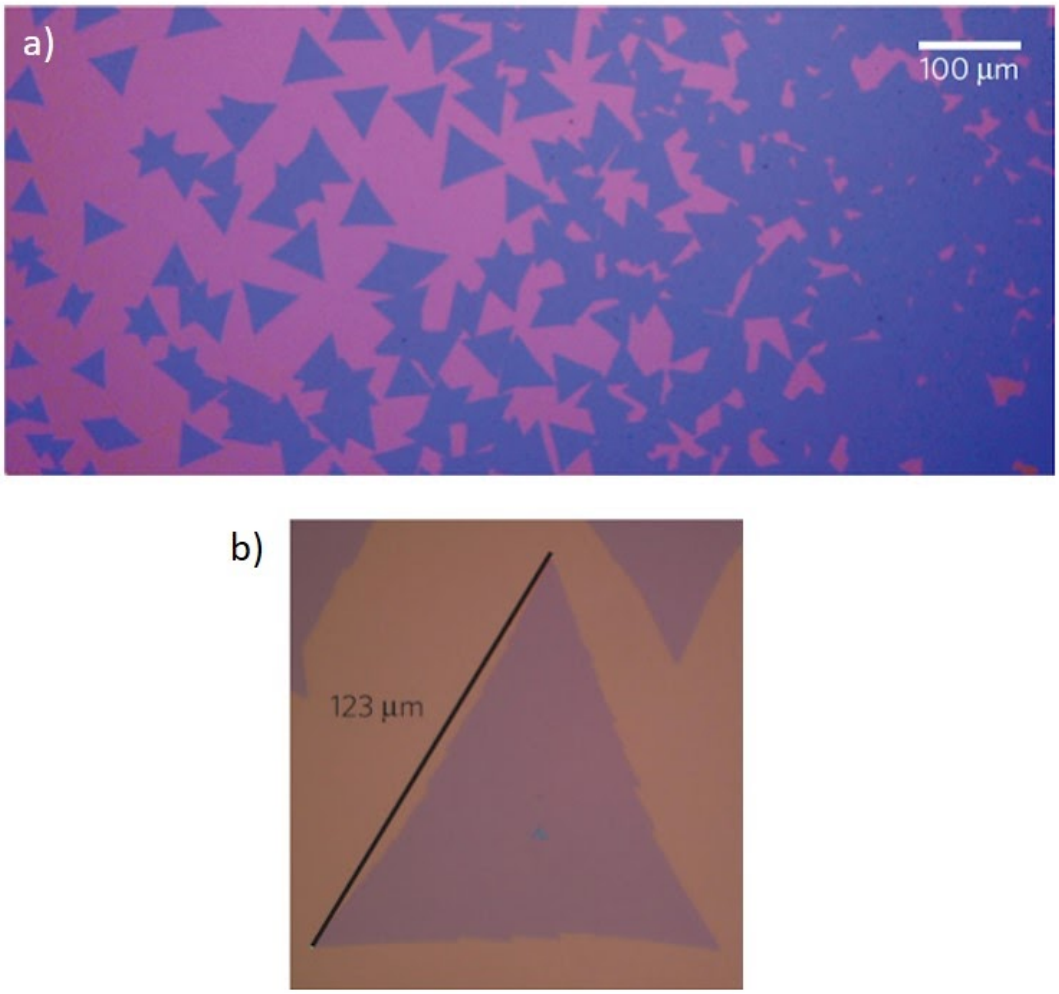

Figure 3.1) a) Optical reflection micrograph of a CVD growth of large grain MoS_2 on a SiO_2 (285 nm)/Si substrate. Monolayer MoS_2 can be seen in violet and substrate in magenta. b) Optical image of a monolayer MoS_2 triangular grain. The unconnected grain has an edge length of 123 µm [25].

Vapor phase transport has emerged as an effective technique at growing high quality films of MoS_2 over large areas. Lu Ma et al. demonstrated room temperature mobilities of 192 cm^2/Vs and good out-of-plane ordering and in-plate epitaxial relationship over 1 cm^2 areas [13]. The work focused on sulfurization of Mo thin films sputtered on single-crystal (0001) oriented sapphire substrates. The Al_2O_3 was used to serve as an epitaxial template for MoS_2 once formed. Unlike past work, this investigation used MoS_2 as the sulfur source instead of sulfur powder directly in order to achieve better control of supersaturation of sulfur vapor which reduces the nucleation of many grains and the formation of poor in-plane orientation.

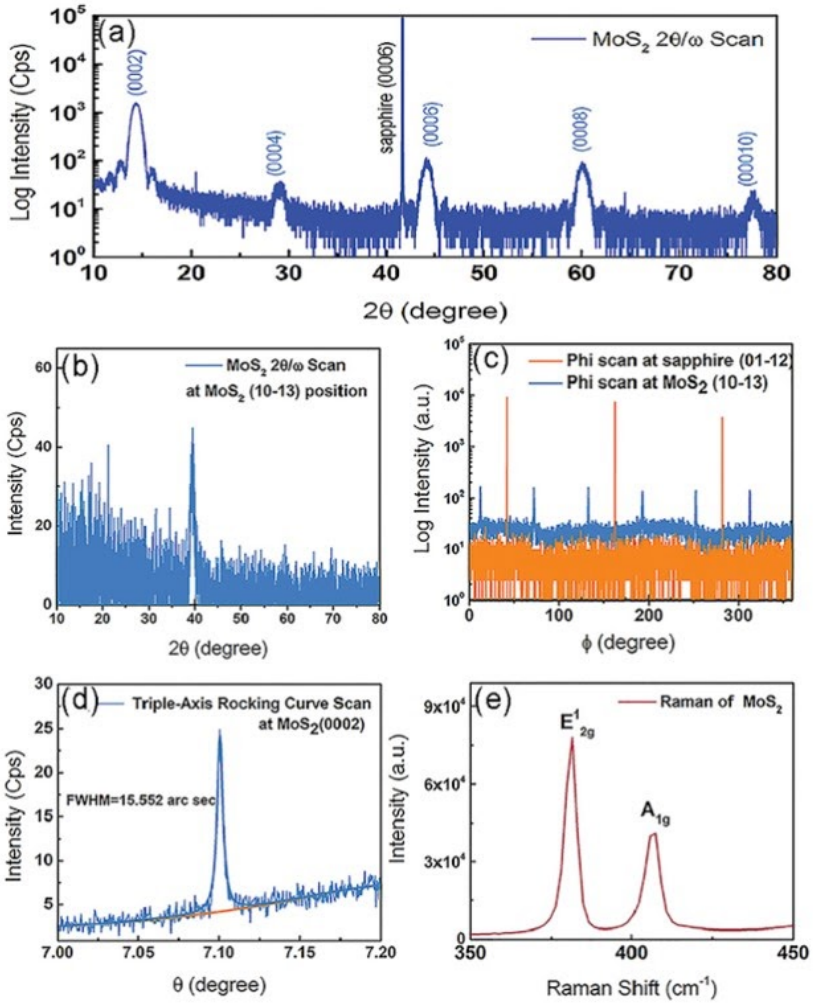

Figure 3.2) a) 2Θ/ω Scan of MoS_2 on sapphire. b) 2Θ/ω scan at MoS_2 (10-13) peak position. c) Phi scan at MoS_2 (10-13) position. d) Triple-axis rocking curve scan at MoS_2 (0002) diffraction position. e) Raman spectra of MoS_2 film [13].

Though large area high quality films have been made by this technique, control over film thickness has been limited. Thus there is still a need to develop a synthesis technique for the growth of large area highly crystalline monolayer thin films of MoS_2. Given the control offered by PLD, it remains a good candidate growth technique.

While physical vapor deposition methods, particularly PLD, have been explored less, more recently there have been a few reports of MoS_2 growth by PLD [26], [27]. Late et al. deposited films containing dense nanostructures of MoS_2 on W and Si and studied the field emission and photo-response [26]. MoS_2 growth mechanism by PLD on metal substrates like Al, Ag, Ni, and Cu have also been studied [27].

This work focuses on the use of PLD for the growth of highly crystalline MoS_2 thin films with good layer thickness control. The general program for materials synthesis in this investigation followed an iterative approach. First, applicable phase diagrams were identified to understand the phase space and identify the compositions and temperatures at which the desired phases would be thermodynamically stable. Targets were then purchased or fabricated with compositions most likely to enable the desired film stoichiometry under typical laser fluences and repetition rates. Substrates were selected to template the crystal structure of desired phase, minimize in-plane mismatch strain and induce good out-of-plane texture for the thin films. Growth conditions were then tuned to improve film quality. If film stoichiometry was not achievable across a wide range of growth conditions then target composition would be adjusted. Finally, once good growth conditions were discovered and high quality films were grown, more extensive structural characterization was undertaken.

3.2 Theoretical Considerations for the Growth of MoS_2

The phase relationships for the Mo-S system are fairly simple. Two thermodynamically stable solid phases are present, Mo_2S_3 which is monoclinic with the C^2_{2h} - $P2_1/m$ (No. 11) space group and MoS_2 which belongs to Hexagonal D^4_{6h} - $P6_3/mmc$ (No. 194) space group. Compositions between MoS_2 and MoS_3 have been synthesized by the decomposition of sulfomolybdates with the more sulfur rich compounds being shown to have the *hP6* structure with lattice distortion and expansion up to a Mo:S ratio of 2.59, above which a metastable amorphous phase has been shown to arise [28].

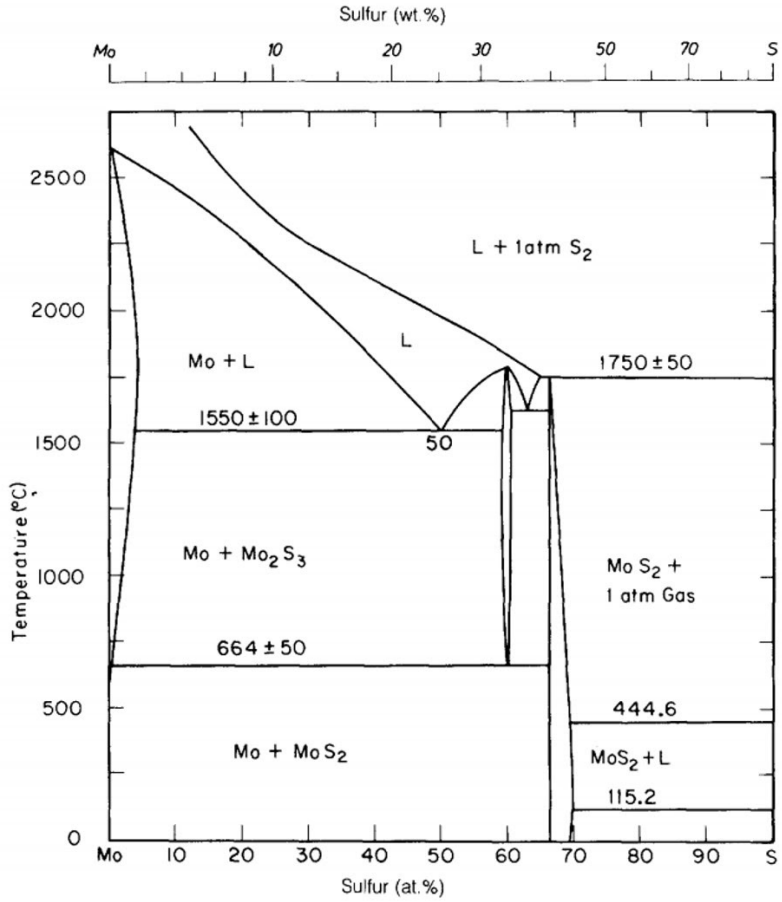

Figure 3.3) Depiction of the Mo-S phase diagram at 1 atm [28].

Sulfur has been shown to have three phases at atmospheric pressure, transitioning from a solid rhombic to a solid monoclinic phase at approximately 95.39 deg C before transitioning to liquid at 115.2 deg C [29]. Due to limitations of past work mapping the Mo-S system, both solid phases of sulfur are not properly depicted however the congruent melting transition temperature of approximately 115 deg C is correct. MoS_2 forms mixed phases with sulfur under sulfur rich conditions. Above 444.6 deg C this mixed phase is between MoS_2 and gaseous sulfur. Under sulfur poor conditions below a temperature of approximately 664 deg C MoS_2 forms a mixed solid phase with Mo. Above this temperature a two phase region with phase separation between MoS_2 and Mo_2S_3 exists. In general, as sulfur is very volatile in comparison to molybdenum, special considerations were needed to ensure that outgassing of sulfur is limited at the growth temperatures targeted (well above the concentric melting temperature of sulfur). While sulfur poor conditions may lead to the nucleation of the Mo_2S_3 phase, this can be discouraged through substrate selection.

MoS_2 has been shown to have a congruent melting temperature of approximately 1750 deg C under 1 atm of S [28]. It has been determined that the nucleation rate N of critically sized nuclei forming on a substrate grown through the direct impingement of gas-phase atoms has the following dependency on temperature at typical thin film growth conditions [30, p. 388]:

$$N \propto \frac{1}{\sqrt{T}} exp(\frac{1}{T})$$

As a result, lower growth temperatures are expected to introduce higher grain density and reduce the quality of obtained thin films. While the approach of growing with higher substrate temperatures helps to rectify this problem, it suggests the likelihood that films will be grown that are sulfur poor. Therefore it was of particular consideration to identify ways to ensure a sulfur rich growth environment.

3.3 Target Preparations and Substrate Selection

The first of two methods employed to achieve a sulfur rich growth environment was sulfur enrichment of the PLD targets. One inch diameter targets were fabricated by the CIP process using commercially obtained powders. MoS_2 and S powders were obtained from Sigma-Alderich and used as received. Targets corresponding to Mo:S composition ratios of 1:2, 2:7 and 1:4 were fabricated.

Since the molybdenum $L\alpha_1$ characteristic X-ray at 2.293 keV [31, pp. I–9] is indistinguishable from the $K\alpha_1$ X-ray at 2.3078 [31, pp. I–11] by EDS, composition was confirmed using WDS. Targets were polished in isopropyl alcohol with silicon carbide sandpaper reducing in grit from 600 to 6000 prior to being mounted on the SEM stage. Because WDS has very high spatial resolution, compositions for the targets were estimated by taking measurements at a minimum of three locations corresponding to the most likely area of laser impingement during growth.

It is noted that the hypothesis of preferential S ablation from the target was confirmed by WDS measurements which showed a significant departure from the target composition on unsanded targets directly after growths. Once the top layer of the target was removed to a depth greater than the laser interaction depth and ablation marks were no longer visible, the expected bulk composition was once again observed.

Substrate selection also plays an important role for phase stabilization and thin film texture. MoS_2 belongs to the Hexagonal D^4_{6h} - $P6_3/mmc$ (No. 194) space group with lattice constants of a = 3.16-3.18 Å and c = 12.29 Å [32]. A number of structurally suitable substrates were identified belonging to the hexagonal crystal family with similar lattice constants whereby the [1000] directions align.

Substrate	Crystal Family	Space Group	Lattice Constant [Å]	Strain (positive is tensile)
SiC - 6H (0001) [33]	Hexagonal	C^4_{6v}-$P6_3mc$ (No. 186)	a = 3.081	-2.2
AlN (0001) [34]	Hexagonal	C^4_{6v}-$P6_3mc$ (No. 186)	a = 3.11	-1.9
GaN (0001) [35, pp. 1–30]	Hexagonal	C^4_{6v}-$P6_3mc$ (No. 186)	a = 3.186	0.5
Al_2O_3 [36, p. 165], [37]	Hexagonal	D^6_{3d}-$R\bar{3}c$ (No. 167)	a = 4.785	0.63
ZnO (0001) [38]	Hexagonal	C^4_{6v}-$P6_3mc$ (No. 186)	a = 3.2495	1.5

Table 3.1) Substrates evaluated for the growth of MoS_2.

While Al_2O_3 doesn't have a lattice constant that directly matches that of MoS_2, epitaxy is achievable because three lattice constants along the [1000] direction of MoS_2 are roughly equivalent in length to two lattice constants along the [1000] direction for Al_2O_3. Figure 3.4 depicts the relative interfacial strain introduced by the various substrates considered.

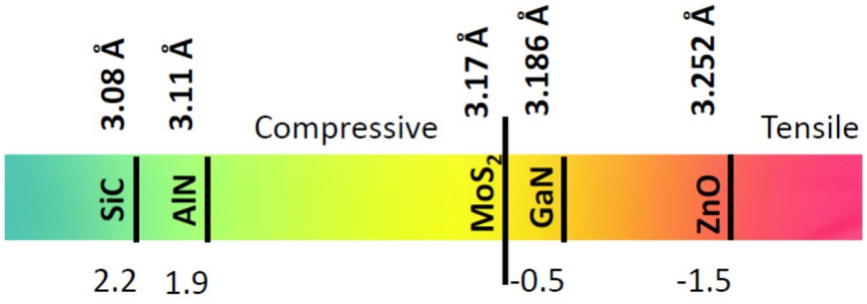

Figure 3.4) Diagram of relative compressive and tensile strain introduced by potential substrates selections for MoS_2.

Of the possibilities listed, substrates of single-side polished Al_2O_3 (0001), GaN (0001), GaN templated on Al_2O_3 (0001) (herein referred to as GaN-t), and SiC-6H (0001) were primarily used for thin film depositions as they were readily available and provided suitable diversity in surface chemistry and introduced low enough compressive or tensile mismatch strain to establish favorable growth conditions.

Substrates were cleaned in preparation of film growths through a series of ultrasonication and air drying steps. Initially the substrates were fully submerged in a small beaker of trichloroethylene (TCE) and ultrasonicated for two minutes. Next, the substrates were removed and dried with compressed air. These steps were then repeated using acetone and isopropyl alcohol before the substrate was mounted to the sample stage with silver thermal paste.

3.4 Growth of MoS_2

A significant number of growth conditions were common to all depositions carried out in this investigation. These included chamber geometry, the positioning and selection of optical elements in the beam path, the laser type and pulse width, target motion, pump down procedure and chamber base pressure, and temperature ramp-down rate after depositions.

MoS_2 film growths were carried out in a PLD chamber primarily used for the deposition of sulfides. In preparation for all growths, the chamber was evacuated to a base pressure of 10^{-6} Torr using a Pfeiffer HiPace 300 turbomolecular pump backed by a Pfeiffer DUO 2.5 rotary vane pump. The laser source was a pulsed KrF excimer laser operating at 248 nm maintained at a 30 ns pulse width. The laser beam was reflected at a 90 deg angle off of a UV mirror prior to passing through a circular mask, a UV transparent lens with a focal length of 16.5 cm and the UV transparent window of the PLD chamber. The beam was focused to a spot 4 mm^2 in area on the target surface.

Targets were mounted to a Neocera multi-target carousel which was operated at 20 RPM during depositions. The surface normal of the target formed a 45 deg angle with the incident beam. Samples were mounted with a slight offset (1-2 in) relative to the axis of rotation of the target so as to avoid positioning samples at the center of the ablative plume and getting a high density of laser particles. The samples were not mounted so far off-axis as to produce major thickness variation over the surface of the substrate. The substrates were mounted 5 cm away from the target within the chamber. While the substrate-target distance can be finely adjusted to change the density of incoming plasma, many aspects of the plume can be adjusted by the laser fluence and therefore this parameter was not adjusted. Substrates varied in size from 0.25 cm^2 to 1.0 cm^2. For all growths, irrespective of substrate temperature during the deposition, films were cooled down to room temperature after the deposition at a rate of 10 deg C/min.

Beyond these static growth conditions and those discussed previously such as target composition and substrate selection, a host of other parameters were explored that meaningfully affected phase stabilization including chamber background pressure and composition, substrate temperature, laser fluence and laser repetition rate.

Along with sulfur enrichment of targets, the second of two methods employed to achieve a sulfur rich growth environment was maintaining a sulfurous residual background ambient from target ablation during depositions. This was accomplished by partially closing the gate value of the turbomolecular pump until the desired chamber pressure was obtained. Background pressure varied from base pressure to as high as 1.0 mTorr. These chamber conditions worked synergistically with substrate temperature allowing much higher growth temperatures and improved crystallinity while maintaining stoichiometry. Figure 3.5 shows the relationship between the full width half maximum (FWHM) of the MoS_2 (002) film peak rocking curve and background pressure at a growth temperature of 700 deg C.

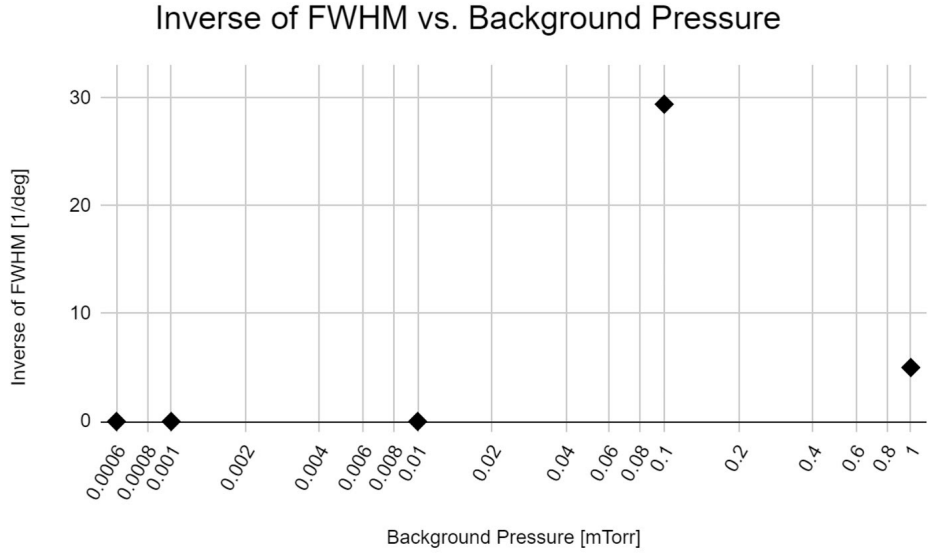

Figure 3.5) Scatter plot of MoS_2 (002) film peak omega scan FWHM vs.chamber background pressure during growth for films grown on GaN substrates.

Depositions carried out at low background pressures where target ablation ambient was actively pumped out resulted in amorphous films that were significantly sulfur poor and followed the general trend of decreasing sulfur content with increasing substrate temperature. This was found to be the case for films grown between 300 deg C and 750 deg C. Depositions carried out in the ablation ambient with a background chamber pressure greater than 0.1 mTorr resulted in films with the proper stoichiometry at substrate temperatures as high as 750 deg C.

Crystalline MoS_2 thin films were first observed from a ten minute deposition that yielded 26 nm films as confirmed by XRR with the following growth conditions:

Parameter	Value
Target Composition	1:4 Mo:S ratio
Substrates	GaN, GaN-t, Al_2O_3, SiC
Growth Temperature	690 deg C
Chamber Pressure	1.0 mTorr
Fluence	1.25 J/cm^2
Repetition Rate	8 Hz

Table 3.2) Growth conditions under which the first crystalline MoS_2 thin films were obtained.

Film peaks were extremely faint and observed as a result of increasing the incident X-ray intensity by removing the beam monochromator. Figure 3.6 shows a 2Theta-Omega scan of the film grown on GaN-t. The extra intensity around the GaN-t substrate peak is a result of the lack of a monochromator. The FWHM of the rocking curve of the MoS_2 (002) peak was 0.2 deg.

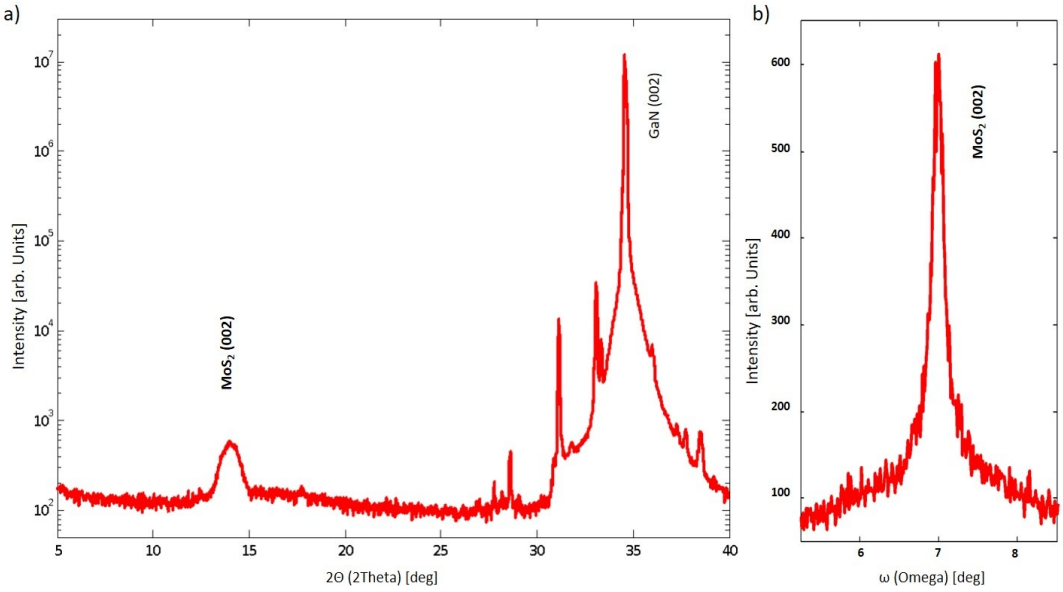

Figure 3.6) a) 2Theta-Omega scan of a MoS_2 thin film grown on GaN from 5 to 40 deg. b) Omega scan of the MoS_2 (002) film peak demonstrating a FWHM of approximately 0.2 deg.

Laser fluence can be an important consideration. If the laser fluence is too low, stoichiometric transfer from the target will not occur and if it is too high, the density of laser particles or clumps of target also ablated along with the plasma plume will be high. Laser fluences from 0.75 J/cm^2 to 3 J/cm^2 were explored. At the high end of the fluence range a high density of laser particles was observed and at low fluences, films demonstrated more prominent sulfur deficiency. It is noteworthy that these growths were completed prior to discovering the importance of maintaining a chamber background ambient. Nonetheless, early on in the investigation a laser fluence of 1.25 J/cm^2 was identified to be sufficient for the purposes of growing highly crystalline MoS_2 films and used for all depositions thereafter.

Laser repetition rate can also be tuned to enhance the growth process. While it is generally appreciated that lower pulse rates provide more time for adatom motion on the surface of the film resulting in lower defect densities, preferential desorption of sulfur atoms under a range of substrate temperatures and chamber pressures is also a major consideration. While crystalline films were grown with repetition rates varying from 2 Hz to 8 Hz, the films with the lowest root mean squared (RMS) surface roughness were synthesized with a repetition rate of 4 Hz.

Once repeatable growth conditions were identified, more fundamental trends relating to growth temperatures could be probed. Figure 3.7 shows FWHM of MoS_2 (002) film peak rocking curves and film composition vs.growth temperature. At lower temperatures it was found that crystallinity suffered but composition was near stoichiometric. At lower temperatures, higher grain densities were expected as the critical nucleation rate would be higher. At higher growth temperatures, films suffered from sulfur deficiency and it is hypothesized that increased defect density resulted in poorer crystallinity.

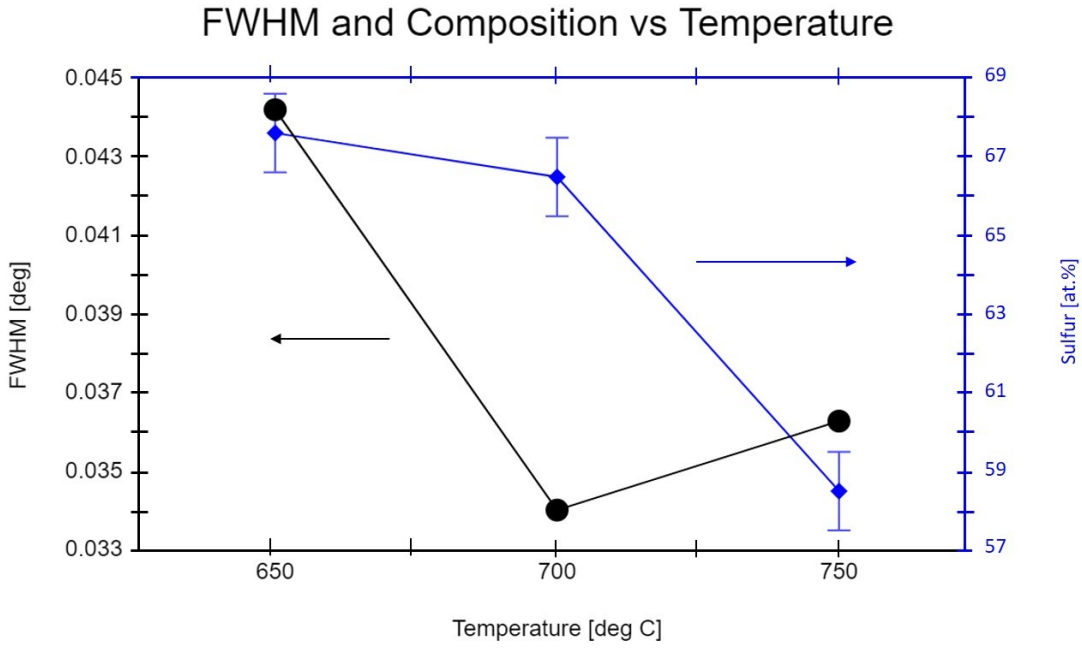

Figure 3.7) Scatter plot of sulfur composition and MoS_2 (002) film peak omega scan FWHM vs.growth temperature for films grown on GaN-t.

Surface treatments were also employed as a means to enhance epitaxy. In particular, hydrochloric acid (HCl) and hydrofluoric acid (HF) surface etches were both employed on GaN-t substrates. As can be seen from Figure 3.8, these surface treatments were found to be ineffective at improving crystallinity. This can most clearly be seen in the omega scans of the MoS_2 (002) peaks which showed the lowest FWHM for films grown on the untreated GaN-t substrates.

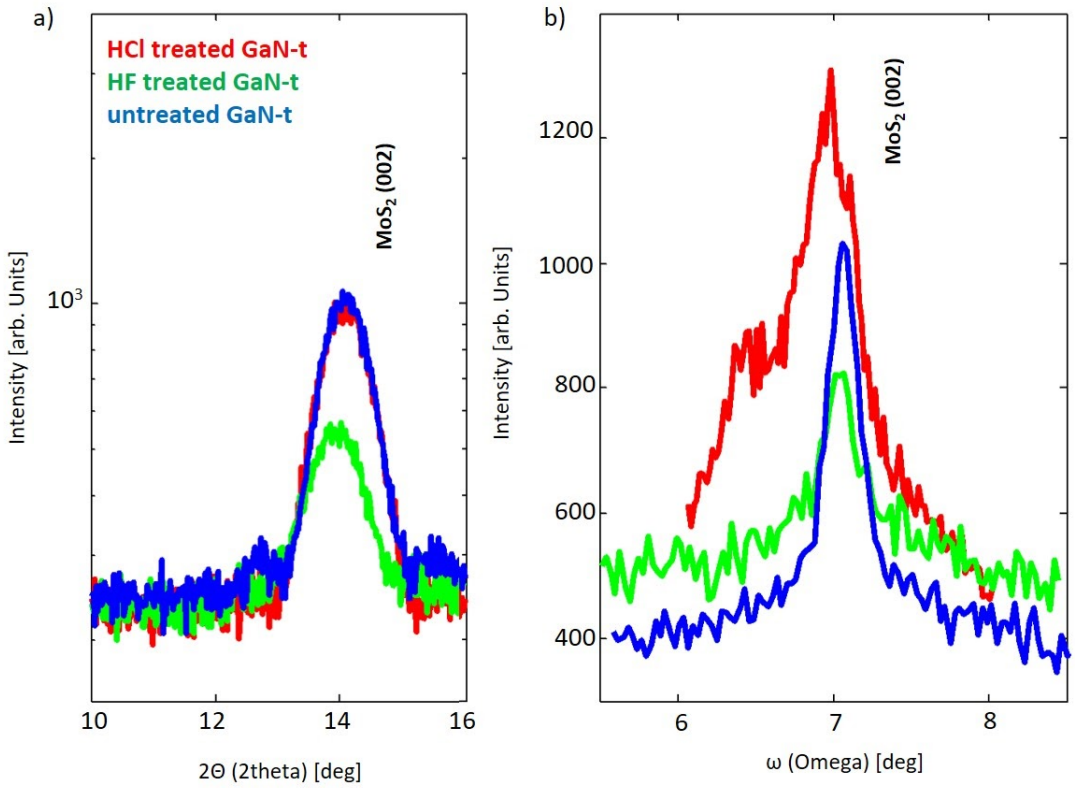

Figure 3.8) a) 2Theta-Omega scan of MoS_2 thin films grown on GaN-t with different surface treatments. b) Omega scans of the MoS_2 (002) film peaks demonstrating a smaller FWHM for films grown on untreated GaN-t.

Finally, in situ annealing was also briefly explored as a means to improve crystallinity. Thicker (26 nm) films and thin films (2ML) were annealed at 700 or 800 deg C for 3 hours in the chamber post growth ambient combined with argon at a chamber pressure of 1 atm. As seen in Figure 3.9 and Figure 3.10, annealing of the 26 nm films resulted in reduction of the out-of-plane lattice constant from c = 12.669 Å to c = 12.454 Å and an increase in the rocking curve FWHM of the MoS_2 (002) film peak from 0.03 deg to 0.04 deg. The reduction in the out-of-plane lattice constant is hypothesized to be a result of film relaxation as the expected bulk lattice parameter is expected to be 12.29 Å [32]. The increase in FWHM is thought to be caused by increased defect density resulting from sulfur outgassing during the annealing process. WDS confirmed the annealed films to be sulfur poor.

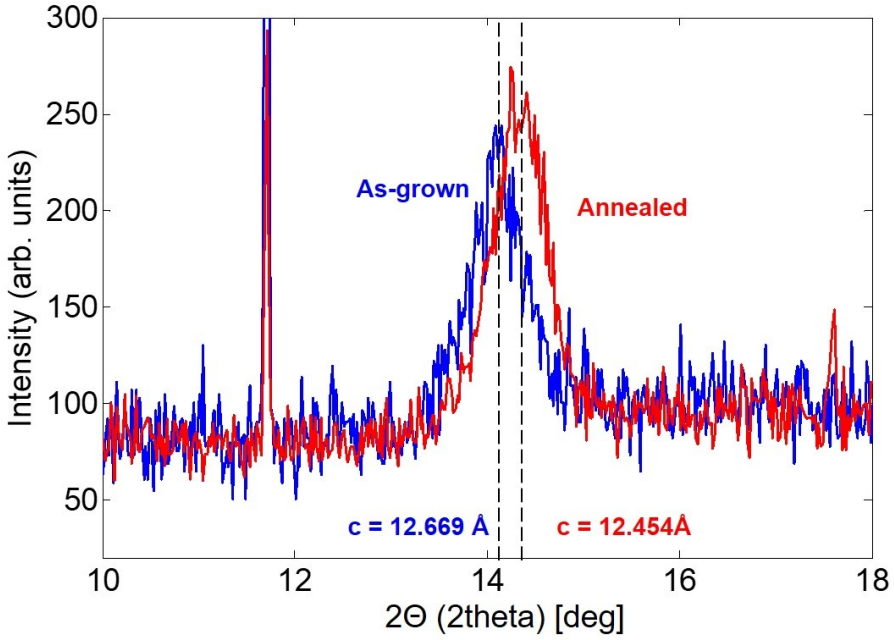

Figure 3.9) Comparison of 2Theta-Omega scans of MoS_2 thin films grown on SiC with and without annealing treatment.

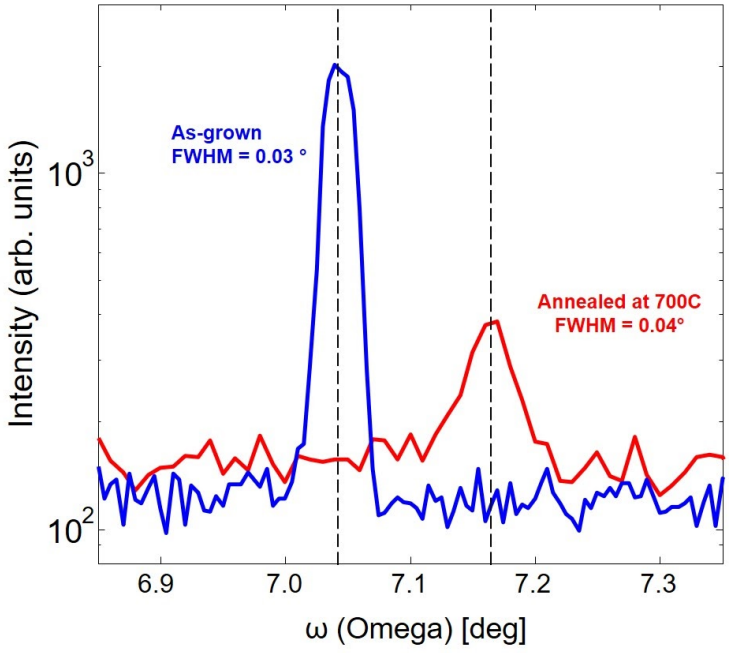

Figure 3.10) Omega scans of the MoS_2 (002) film peaks demonstrating a smaller FWHM for as-grown films on SiC without annealing treatment.

As seen in Figure 3.11, which shows the Raman spectra for annealed and as-grown 2ML films, annealing appears to quench the spectra associated with MoS_2. This evidence seems to suggest that thinner films are less robust to the annealing treatment and have decomposed as a result.

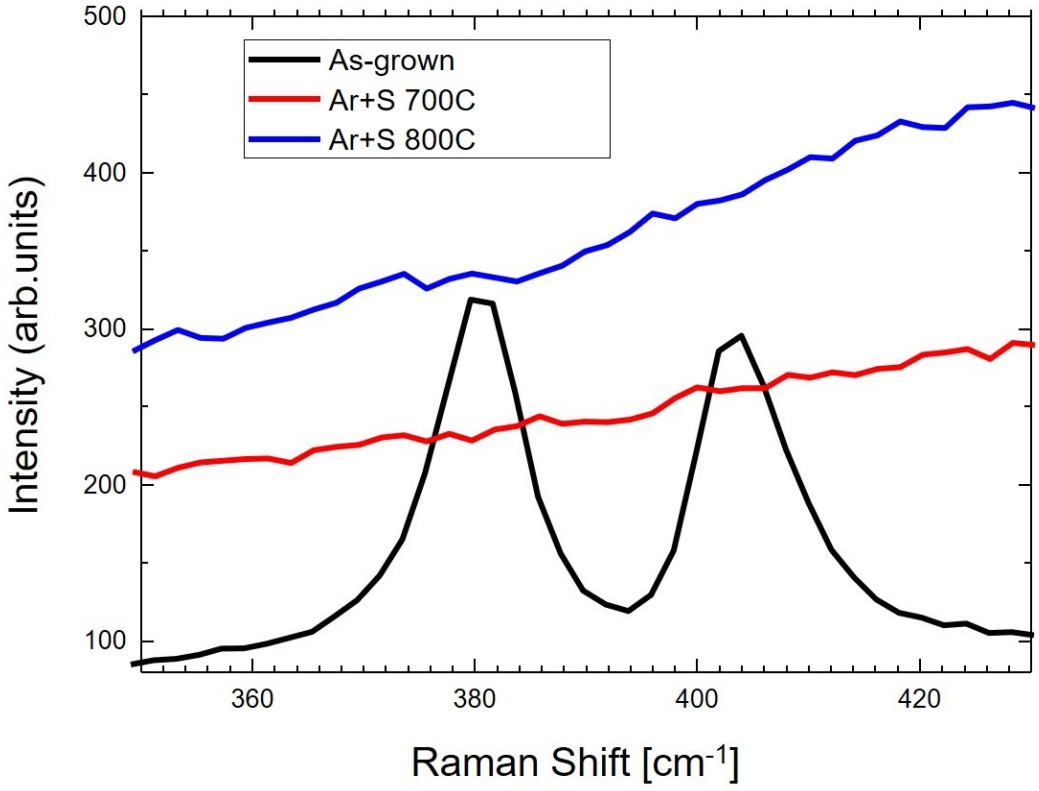

Figure 3.11) Raman spectra showing possible decomposition of 2ML thick MoS_2 films after annealing treatments.

The growth conditions for the highest quality films obtained in this investigation are summarized in Table 3.3 below. These conditions were used in conjunction with those conditions previously discussed which remained unchanged for all growths to yield films with the best out-of-plane and in-plane texture. The data reported and discussed further in Chapter 4 relates to the characterization of these best films. Depositions with these conditions were found to yield a growth rate of 2.0 nm/min as confirmed by X-ray reflectivity measurements.

Parameter	Value
Target Composition	1:4 Mo:S ratio
Substrates	GaN, Al_2O_3, SiC
Growth Temperature	700 deg C
Chamber Pressure	0.1 mTorr
Fluence	1.25 J/cm^2
Repetition Rate	4 Hz

Table 3.3) Growth conditions used to obtain the highest quality films synthesized in this investigation.

References

[1] H. S. S. Ramakrishna Matte *et al.*, "MoS2 and WS2 Analogues of Graphene," *Angewandte Chemie International Edition*, vol. 49, no. 24, pp. 4059–4062, Jun. 2010, doi: 10.1002/anie.201000009.

[2] Z. Zeng *et al.*, "Single-Layer Semiconducting Nanosheets: High-Yield Preparation and Device Fabrication," *Angew. Chem. Int. Ed.*, vol. 50, no. 47, pp. 11093–11097, Nov. 2011, doi: 10.1002/anie.201106004.

[3] G. Eda, H. Yamaguchi, D. Voiry, T. Fujita, M. Chen, and M. Chhowalla, "Photoluminescence from Chemically Exfoliated MoS $_2$," *Nano Lett.*, vol. 11, no. 12, pp. 5111–5116, Dec. 2011, doi: 10.1021/nl201874w.

[4] K. F. Mak, C. Lee, J. Hone, J. Shan, and T. F. Heinz, "Atomically Thin MoS 2 : A New Direct-Gap Semiconductor," *Phys. Rev. Lett.*, vol. 105, no. 13, p. 136805, Sep. 2010, doi: 10.1103/PhysRevLett.105.136805.

[5] W. M. R. Divigalpitiya, R. F. Frindt, and S. R. Morrison, "Inclusion Systems of Organic Molecules in Restacked Single-Layer Molybdenum Disulfide," *Science*, vol. 246, no. 4928, pp. 369–371, Oct. 1989, doi: 10.1126/science.246.4928.369.

[6] C. Lee, H. Yan, L. E. Brus, T. F. Heinz, J. Hone, and S. Ryu, "Anomalous Lattice Vibrations of Single- and Few-Layer MoS $_2$," *ACS Nano*, vol. 4, no. 5, pp. 2695–2700, May 2010, doi: 10.1021/nn1003937.

[7] A. Splendiani *et al.*, "Emerging Photoluminescence in Monolayer MoS $_2$," *Nano Lett.*, vol. 10, no. 4, pp. 1271–1275, Apr. 2010, doi: 10.1021/nl903868w.

[8] K.-G. Zhou, N.-N. Mao, H.-X. Wang, Y. Peng, and H.-L. Zhang, "A Mixed-Solvent Strategy for Efficient Exfoliation of Inorganic Graphene Analogues," *Angew. Chem. Int. Ed.*, vol. 50, no. 46, pp. 10839–10842, Nov. 2011, doi: 10.1002/anie.201105364.

[9] Y. Peng *et al.*, "Hydrothermal Synthesis and Characterization of Single-Molecular-Layer MoS_2 and $MoSe_2$," *Chem. Lett.*, vol. 30, no. 8, pp. 772–773, Aug. 2001, doi: 10.1246/cl.2001.772.

[10] C. Altavilla, M. Sarno, and P. Ciambelli, "A Novel Wet Chemistry Approach for the Synthesis of Hybrid 2D Free-Floating Single or Multilayer Nanosheets of MS_2 @oleylamine (M=Mo, W)," *Chem. Mater.*, vol. 23, no. 17, pp. 3879–3885, Sep. 2011, doi: 10.1021/cm200837g.

[11] J. Pütz and M. A. Aegerter, "MoS x Thin Films by Thermolysis of a Single-Source Precursor," *Journal of Sol-Gel Science and Technology*, vol. 19, no. 1/3, pp. 821–824, 2000, doi: 10.1023/A:1008728604305.

[12] Y.-H. Lee *et al.*, "Synthesis of Large-Area MoS_2 Atomic Layers with Chemical Vapor Deposition," *Adv. Mater.*, vol. 24, no. 17, pp. 2320–2325, May 2012, doi: 10.1002/adma.201104798.

[13] L. Ma *et al.*, "Epitaxial growth of large area single-crystalline few-layer MoS_2 with high space charge mobility of 192 $cm^2 V^{-1} s^{-1}$," *Appl. Phys. Lett.*, vol. 105, no. 7, p. 072105, Aug. 2014, doi: 10.1063/1.4893143.

[14] S. Helveg *et al.*, "Atomic-Scale Structure of Single-Layer MoS 2 Nanoclusters," *Phys. Rev. Lett.*, vol. 84, no. 5, pp. 951–954, Jan. 2000, doi: 10.1103/PhysRevLett.84.951.

[15] J. V. Lauritsen *et al.*, "Size-dependent structure of MoS2 nanocrystals," *Nature Nanotech*, vol. 2, no. 1, pp. 53–58, Jan. 2007, doi: 10.1038/nnano.2006.171.

[16] C. Muratore *et al.*, "Continuous ultra-thin MoS_2 films grown by low-temperature physical vapor deposition," *Appl. Phys. Lett.*, vol. 104, no. 26, p. 261604, Jun. 2014, doi: 10.1063/1.4885391.

[17] H. Schafer, *Chemical Transport Reactions.* Saint Louis: Elsevier Science, 2016.

[18] P. Joensen, R. F. Frindt, and S. R. Morrison, "Single-layer MoS2," *Materials Research Bulletin*, vol. 21, no. 4, pp. 457–461, Apr. 1986, doi: 10.1016/0025-5408(86)90011-5.

[19] J. N. Coleman *et al.*, "Two-Dimensional Nanosheets Produced by Liquid Exfoliation of Layered Materials," *Science*, vol. 331, no. 6017, pp. 568–571, Feb. 2011, doi: 10.1126/science.1194975.

[20] R. J. Smith *et al.*, "Large-Scale Exfoliation of Inorganic Layered Compounds in Aqueous Surfactant Solutions," *Adv. Mater.*, vol. 23, no. 34, pp. 3944–3948, Sep. 2011, doi: 10.1002/adma.201102584.

[21] K. S. Novoselov *et al.*, "Two-dimensional atomic crystals," *Proceedings of the National Academy of Sciences*, vol. 102, no. 30, pp. 10451–10453, Jul. 2005, doi: 10.1073/pnas.0502848102.

[22] M. M. Benameur, B. Radisavljevic, J. S. Héron, S. Sahoo, H. Berger, and A. Kis, "Visibility of dichalcogenide nanolayers," *Nanotechnology*, vol. 22, no. 12, p. 125706, Mar. 2011, doi: 10.1088/0957-4484/22/12/125706.

[23] K.-K. Liu *et al.*, "Growth of Large-Area and Highly Crystalline MoS_2 Thin Layers on Insulating Substrates," *Nano Lett.*, vol. 12, no. 3, pp. 1538–1544, Mar. 2012, doi: 10.1021/nl2043612.

[24] S. Najmaei *et al*., "Vapour phase growth and grain boundary structure of molybdenum disulphide atomic layers," *Nature Mater*, vol. 12, no. 8, pp. 754–759, Aug. 2013, doi: 10.1038/nmat3673.
[25] A. M. van der Zande *et al*., "Grains and grain boundaries in highly crystalline monolayer molybdenum disulphide," *Nature Mater*, vol. 12, no. 6, pp. 554–561, Jun. 2013, doi: 10.1038/nmat3633.
[26] D. J. Late *et al*., "Pulsed Laser-Deposited MoS_2 Thin Films on W and Si: Field Emission and Photoresponse Studies," *ACS Appl. Mater. Interfaces*, vol. 6, no. 18, pp. 15881–15888, Sep. 2014, doi: 10.1021/am503464h.
[27] T. A. J. Loh and D. H. C. Chua, "Growth Mechanism of Pulsed Laser Fabricated Few-Layer MoS_2 on Metal Substrates," *ACS Appl. Mater. Interfaces*, vol. 6, no. 18, pp. 15966–15971, Sep. 2014, doi: 10.1021/am503719b.
[28] L. Brewer and R. H. Lamoreaux, "The Mo-S system (Molybdenum-Sulfur)," *Bulletin of Alloy Phase Diagrams*, vol. 1, no. 2, pp. 93–95, Sep. 1980, doi: 10.1007/BF02881201.
[29] A. G. M. Ferreira and L. Q. Lobo, "The low-pressure phase diagram of sulfur," *The Journal of Chemical Thermodynamics*, vol. 43, no. 2, pp. 95–104, Feb. 2011, doi: 10.1016/j.jct.2010.07.007.
[30] M. Ohring, *The Materials Science of Thin Films*, 2nd edition. San Diego, CA: Academic Press, 2001.
[31] A. C. Thompson, *X-ray Data Booklet*. Lawrence Berkeley National Laboratory, University of California, 2001.
[32] B. Radisavljevic, A. Radenovic, J. Brivio, V. Giacometti, and A. Kis, "Single-layer MoS2 transistors," *Nature Nanotech*, vol. 6, no. 3, pp. 147–150, Mar. 2011, doi: 10.1038/nnano.2010.279.
[33] G. C. Capitani, S. D. Pierro, and G. Tempesta, "The 6H-SiC structure model: Further refinement from SCXRD data from a terrestrial moissanite," *American Mineralogist*, vol. 92, no. 2–3, pp. 403–407, Feb. 2007, doi: 10.2138/am.2007.2346.
[34] N. S. VanDamme, S. M. Richard, and S. R. Winzer, "Liquid-Phase Sintering of Aluminum Nitride by Europium Oxide Additives," *Journal of the American Ceramic Society*, vol. 72, no. 8, pp. 1409–1414, 1989, doi: 10.1111/j.1151-2916.1989.tb07662.x.
[35] M. E. Levinshtein, S. L. Rumyantsev, and M. S. Shur, Eds., *Properties of Advanced Semiconductor Materials: GaN, A1N, InN, BN, SiC, SiGe*, 1st edition. New York: Wiley-Interscience, 2001.
[36] E. Murad and J. Cashion, *Mössbauer Spectroscopy of Environmental Materials and Their Industrial Utilization*. Springer Science & Business Media, 2011.
[37] H. Morkoç, S. Strite, G. B. Gao, M. E. Lin, B. Sverdlov, and M. Burns, "Large-band-gap SiC, III-V nitride, and II-VI ZnSe-based semiconductor device technologies," *Journal of Applied Physics*, vol. 76, no. 3, pp. 1363–1398, Aug. 1994, doi: 10.1063/1.358463.
[38] W. M. Haynes, Ed., *CRC Handbook of Chemistry and Physics, 92nd Edition*, 92 edition. Boca Raton, Fla.: CRC Press, 2011.

Chapter 4

Characterization of MoS_2 Thin Films

This chapter provides a detailed discussion of characterization results of the best MoS_2 thin films synthesized in this investigation. XRD, TEM, AFM and Raman Spectroscopy results are presented and discussed as well as used in conjunction to develop an inclusive understanding of the thin films grown. Highly crystalline MoS_2 thin films with good thickness control and very good large area uniformity are presented herein.

4.1 XRD

XRD patterns in the 2Theta-Omega mode were obtained for films grown on various substrates. Figure 4.1 shows a typical XRD pattern for a MoS_2 thin film grown on GaN. The scans were done using the MoS_2 film (002) peak as the reference. The occurrence of only (00l) peak confirms good out-of-plane texture. In addition, thickness fringes around the MoS_2 (002) peak are indicative of a clean interface between MoS_2 and GaN with minimal interdiffusion.

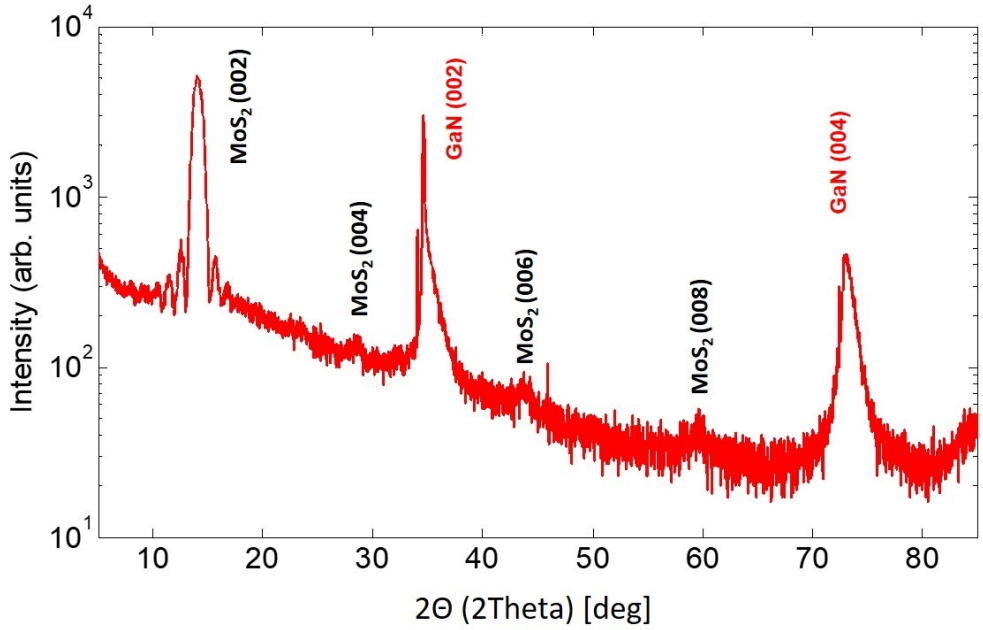

Figure 4.1) 2Theta-Omega scan of a MoS_2 thin film grown on GaN from 5 to 85 deg with dialed in growth conditions.

To estimate the crystallinity of films, rocking curves around the MoS_2 (002) peak were measured. Figure 4.2(a) shows the omega scan for the MoS_2 (002) film peak demonstrating a FWHM of 0.034 deg. The XRR measurement depicted in Figure 4.2(b) again demonstrates clean interfaces and indicates a film thickness of 12.2 nm.

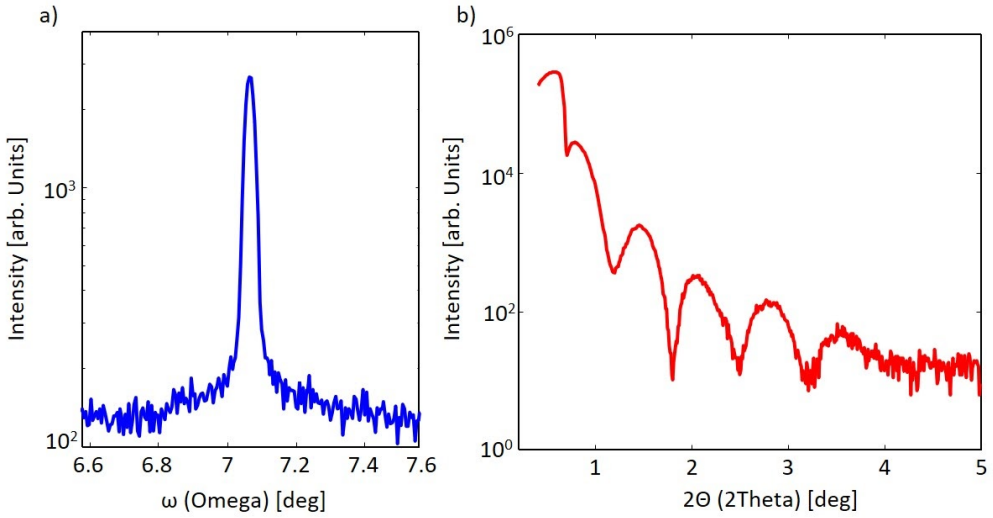

Figure 4.2) a) Rocking curve of the MoS_2 (002) film peak grown on GaN demonstrating a FWHM of 0.034 deg. b) XRR scan of the MoS_2 film indicating a thickness of 12.2 nm.

For films grown on SiC, rocking curves with FWHM values as low as 0.01 deg were observed suggesting a high degree of crystallinity in a given region as seen in Figure 4.3(a). To gain information about the crystallinity of the PLD deposited MoS_2 films, rocking curves at varying φ angles about the MoS_2 (002) peaks were measured. As can be seen in Figure 4.3(b), the measurements show that two peaks exist and their relative peak positions vary with φ, characteristic of the presence of at least two facets in the MoS_2 films. Figure 4.3(b) shows rocking curves about the MoS_2 (002) peak for a film grown on SiC (001) at different φ angles. At φ =0 deg, only one facet of MoS_2 is observed, however, for φ=90 deg two peaks are observed, representing the offset angles of the two facets with respect to the crystallographic (001) axis of SiC. Unsurprisingly, when φ=180 deg, only one clear facet film peak is observed identical to the case when φ is 0 deg. Furthermore, the measurement at φ=270 deg is a mirror image of the scan when φ is 90 deg.

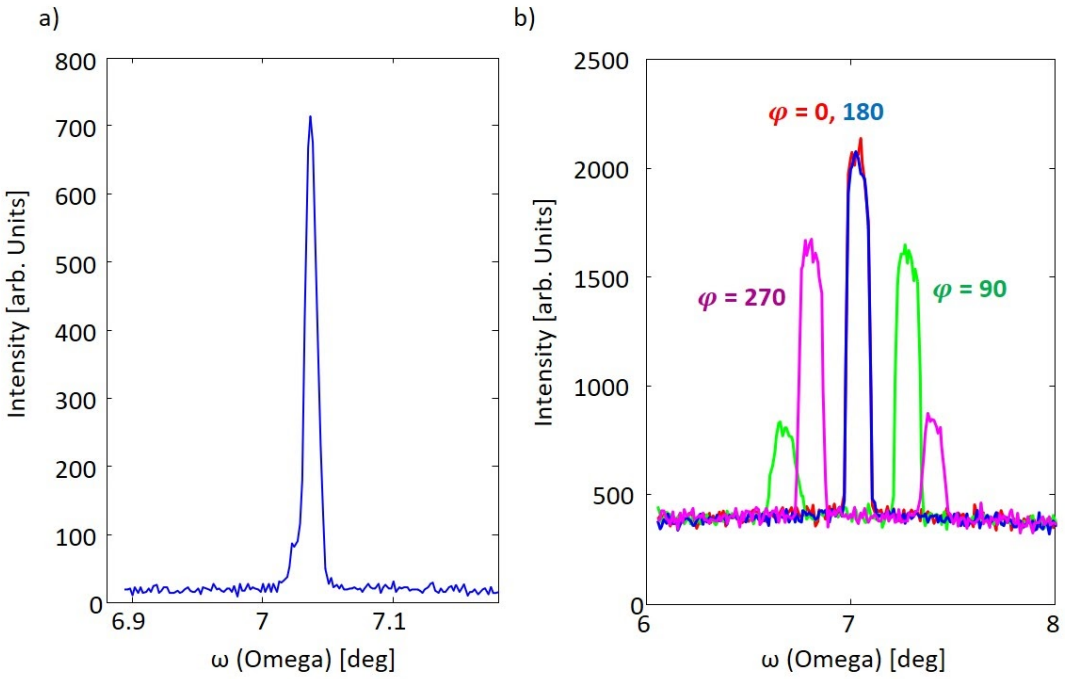

Figure 4.3) a) Rocking curve of the MoS_2 (002) film peak grown on SiC demonstrating a FWHM of 0.01 deg [1]. b) Rocking curves of the MoS_2 (002) film peak at a phi angle of 0, 90, 180 and 270 deg.

Reciprocal space maps (RSM) of the two positions (φ = 0°, 90°) are shown in Figure 4.4 for MoS_2 on SiC and for φ = 90° for MoS_2 on GaN in Figure 4.5. The RSMs clearly show the presence of two facets for φ=90° for both substrates. This confirms the presence of two different facets in the MoS_2 films. Similar corrugations were also observed in graphene films when supported on oxide substrates due to the van der Waals interaction coupled with in-plane mismatch strain [2].

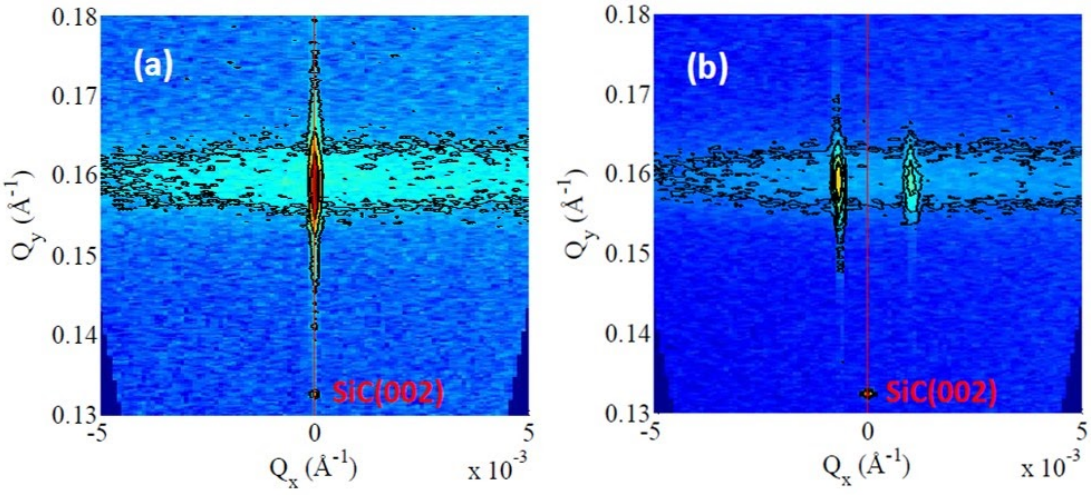

Figure 4.4) A reciprocal space map of the MoS_2 (002) film peak grown on SiC for a) φ = 0 deg and b) φ = 90 deg [1].

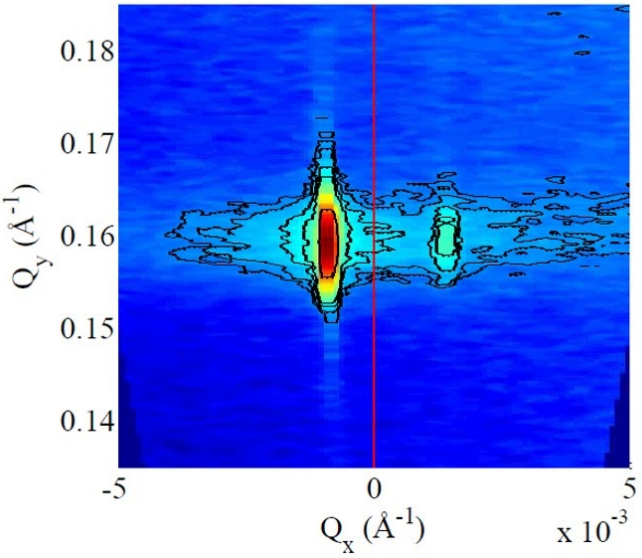

Figure 4.5) A reciprocal space map of the MoS_2 (002) film peak grown on GaN [1].

4.2 TEM

Regular and reverse contrast SAED micrographs were captured for the MoS_2 film on GaN substrate. Figure 4.6(b) shows the SAED pattern with only MoS_2 film peaks indexed. For both MoS_2 and GaN, the [010] direction serves as the zone axis and for both layers the out-of-plane direction is [001] and the in-plane direction is [100]. The lack of ring patterns along with the RSM scans indicate the existence of [001] prefered texture. The in-plane quasi-epitaxial relationship of MoS_2 (10-10)||GaN (10-10) can be distinguished.

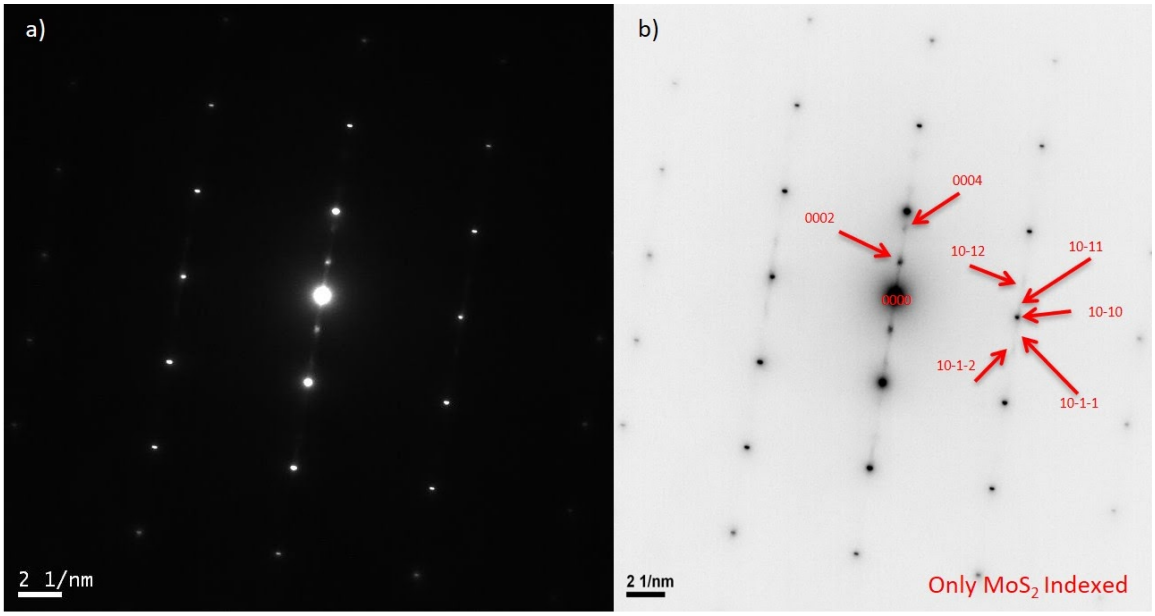

Figure 4.6) a) Regular and b) reverse contrast selected area electron diffraction micrograph with peaks indexed for MoS_2 showing in-plane quasi-epitaxial relationship $(10\bar{1}0)MoS_2 \| (10\bar{1}0)GaN$ [1].

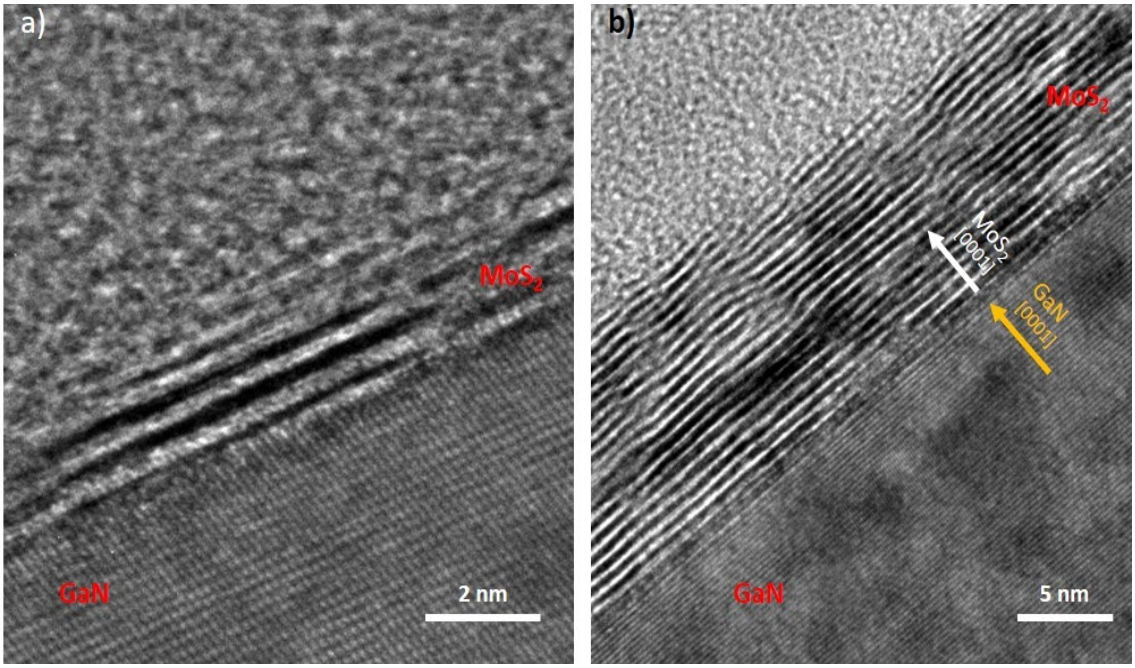

Figure 4.7) Cross-sectional TEM micrographs of samples a) 4ML in thickness and b) 14ML in thickness showing the [0001]||[0001] epitaxial relationship between MoS_2 and GaN.

The out-of-plane prefered texture can be further distinguished by the cross-sectional TEM micrograph of as-grown MoS_2 thin films on GaN-t seen in Figure 4.7. The stacking of MoS_2 (001) planes on GaN (001) is clearly visible for both thicker (14ML) and thinner (4ML) films.

HAADF-STEM micrographs provide additional insight into the apparent structure of the MoS_2 film. The covalently bonded Mo-S layers appear to be corrugated or wavy which corroborates the interpretation provided by XRD scans. Inter-layer growth is visible as well as incomplete Mo-S layers.

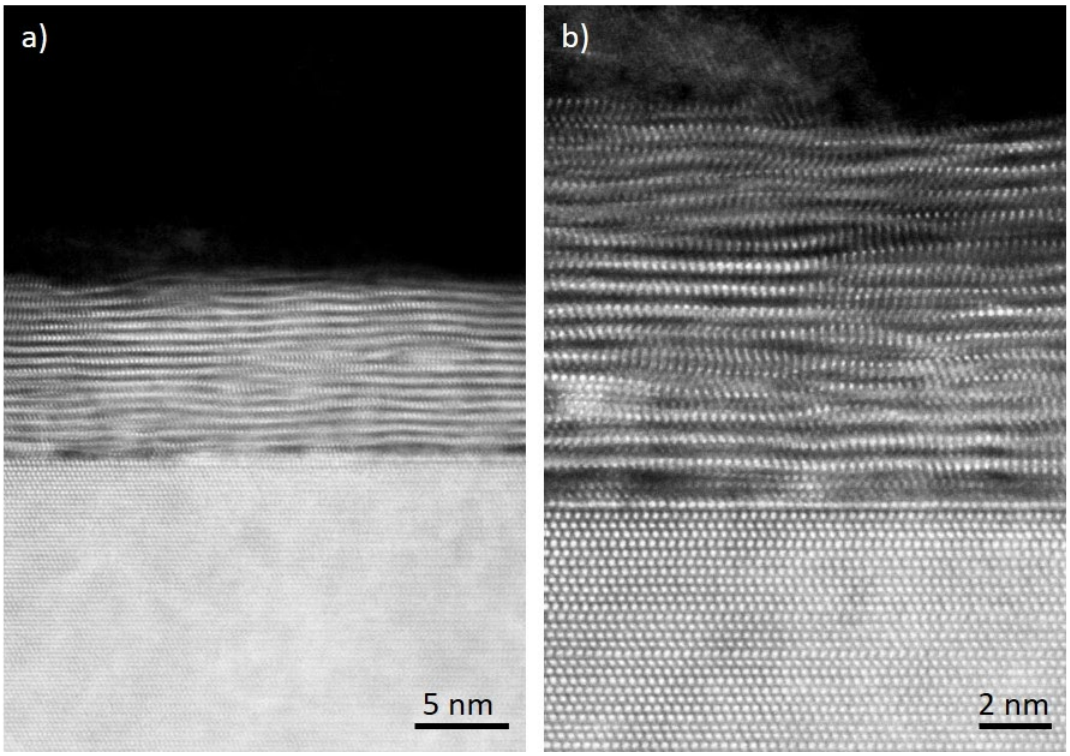

Figure 4.8) HAADF-STEM of a MoS_2 film at a) lower and b) higher magnification.

4.3 AFM

Large area AFM scans (225 μm^2) revealed a moderate density of laser particles. Smaller scan areas (25 μm^2) more representative of film roughness without laser particles identified increasing film roughness with increasing film thickness. For 1ML films a RMS surface roughness of 0.27 nm was measured. At 2ML the RMS surface roughness was found to be 1.04 nm and for 10 nm thick MoS_2 film RMS surface roughness was found to be 7.6 nm.

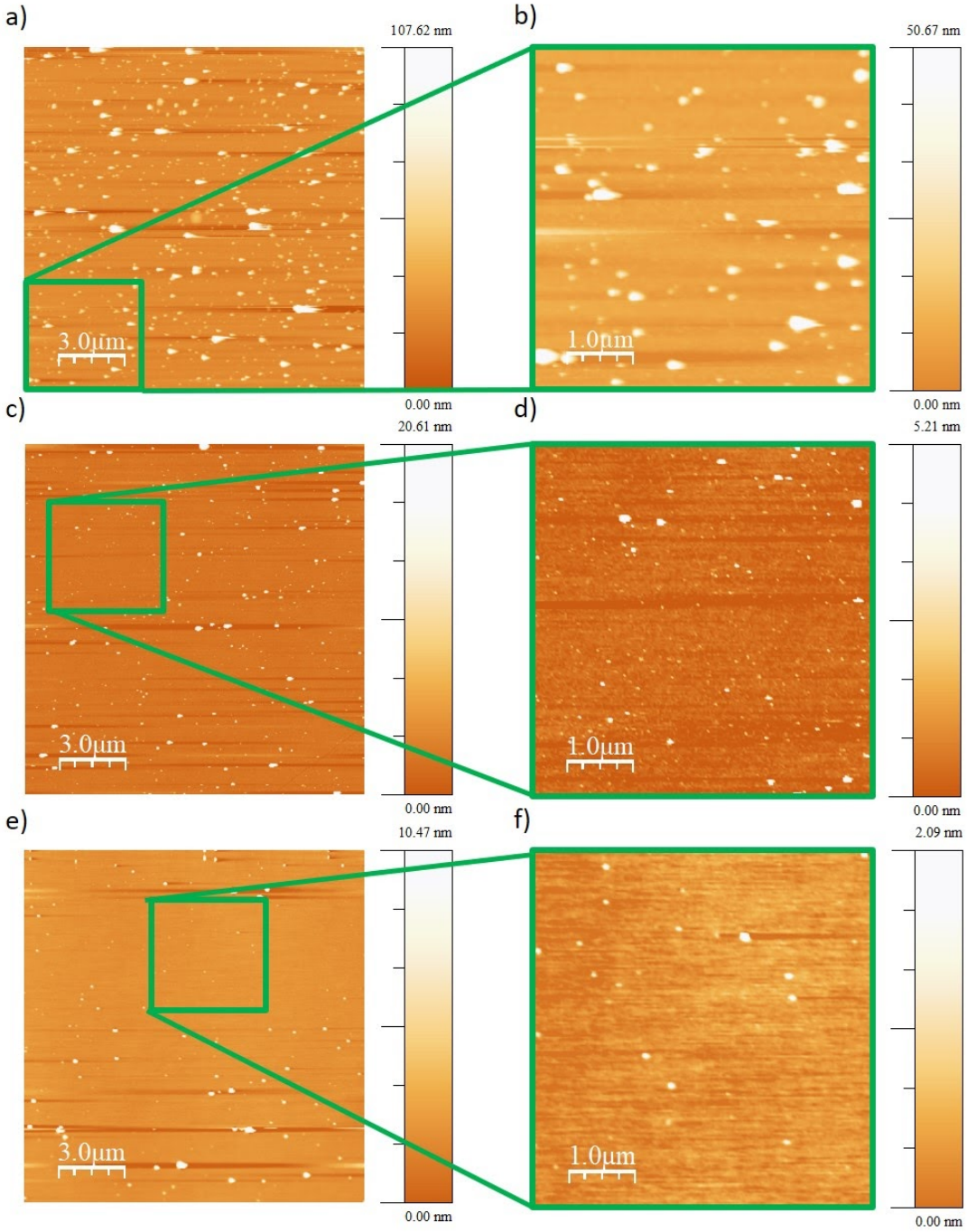

Figure 4.9) AFM micrographs MoS_2 thin films on GaN of varying thickness. 10 nm film with a) 225 μm^2 scan area and 13.0 nm RMS surface roughness and b) 25 μm^2 scan area and 7.6 nm RMS surface roughness respectively. 2 ML film with c) 225 μm^2 scan area and 3.5 nm RMS surface roughness and d) 25 μm^2 scan area and 1.04 nm RMS surface roughness respectively. 1 ML film with f) 25 μm^2 scan area and 0.27 nm RMS surface roughness [1] and e) 225 μm^2 scan area and 2.2 nm RMS surface roughness respectively.

4.4 Raman Spectroscopy

Raman spectroscopy has been used extensively to characterize MoS_2 films of varying thicknesses. Off resonance MoS_2 has four first-order Raman active modes at 408 cm^{-1} (A_{1g}), 382 cm^{-1} (E^1_{2g}), 286 cm^{-1} (E_{1g}) and 32 cm^{-1} (E^2_{2g}). In particular, the E^1_{2g} mode results from the in-plane vibrations of the two sulfur atoms moving in opposite directions with respect to the Mo atom while the A_{1g} mode is a result of the out-of-plane vibration of only the S atoms in opposite directions [3]. As shown experimentally, when the number of layers decreases, the A_{1g} peak blue shifts as a result of the interlayer van der Waals interaction in MoS_2 , resulting in higher force constants. By contrast, the E^1_{2g} peak red shifts. This red shift is thought to be due to stacking induced structural changes or long-range Coulombic intra-layer interactions in thicker MoS_2, which may dominate the change in atomic vibration frequency [3]–[5]. The difference between the in-plane E^1_{2g} mode and out-of-plane A_{1g} mode in the Raman spectrum, δ, is representative of the film's thickness with decreasing difference between the peaks corresponding to a decrease in the film thickness.

All grown MoS_2 thin films have a similar Raman signal in terms of peak position, peak height and line shape irrespective of the substrate on which they are grown suggesting that the films only weakly adhere to the diverse substrates by van der Waals forces, which can be seen in Figure 4.10.

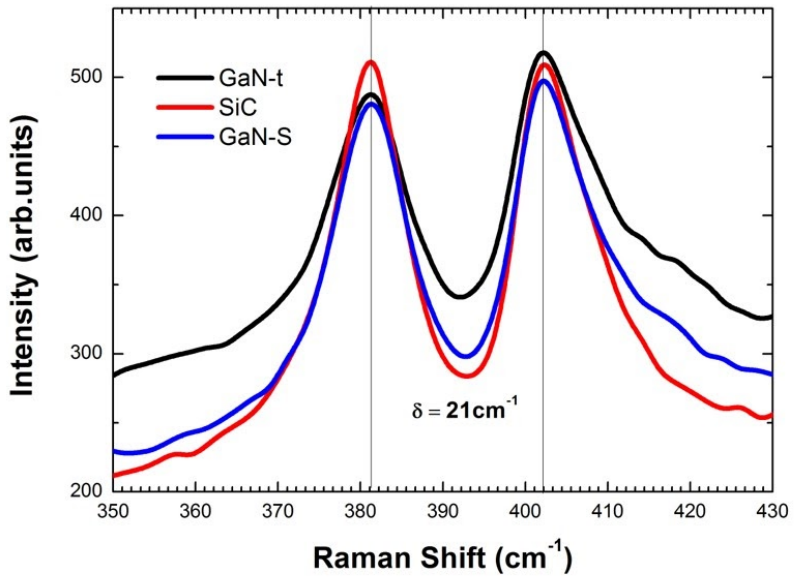

Figure 4.10) Raman spectra of 1 ML MoS_2 films on GaN/Al_2O_3 (0001) (black), SiC-6H (0001) (red) and GaN (0001) (blue) [1].

Thickness effects are clearly observed in the thinnest samples (1 ML) showing a δ = 20.5 cm^{-1} and the thickest films showing bulk like behavior with δ = 25 cm^{-1}. The thickness of the films are controlled by regulating the number of laser pulses as previously discussed and growth rate has been calculated by XRR measurements and further confirmed for films of only a few monolayers by TEM and Raman spectroscopy. Raman spectra for 1ML, 2ML, and 8ML MoS_2 films can be seen in Figure 4.11.

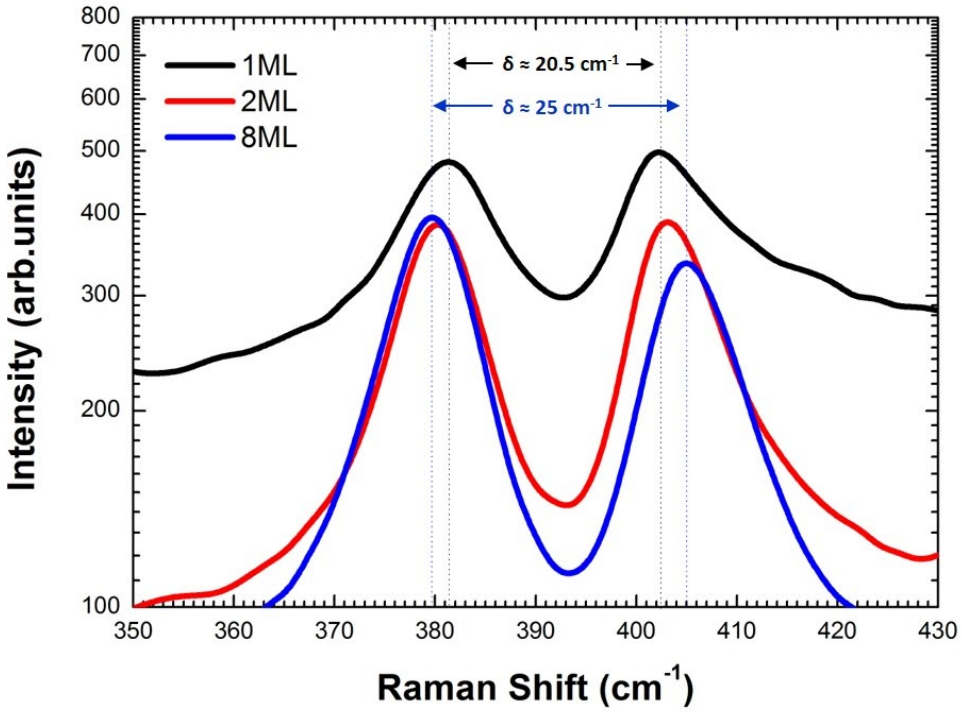

Figure 4.11) Raman spectra showing the effect of MoS_2 thickness variation on peak separation. All films were grown on GaN substrates [1].

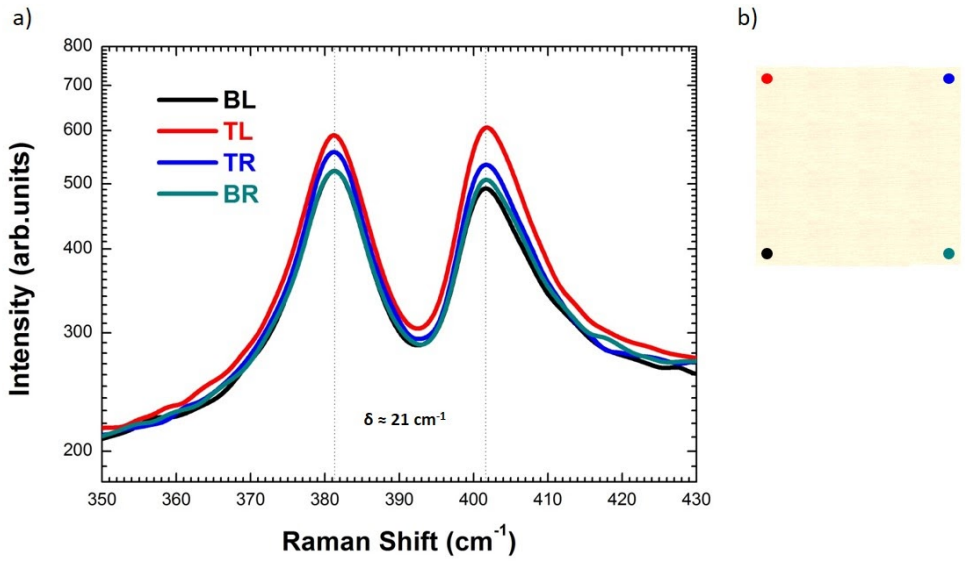

Figure 4.12) a) Raman microprobe measurement displaying curves corresponding to the four corner positions, bottom left (BL), top left (TL), top right (TR), and bottom right (BR) of a 5x5 mm^2 2ML thick MoS_2 film grown GaN indicating good uniformity over the area [1]. b) Schematic of the measured film.

In order to demonstrate the uniformity of the samples, Raman measurements were performed on all four corners of a 5x5 mm^2 2ML thick representative sample. Figure 4.12 shows the Raman spectrum taken at bottom left (BL), top left (TL), top right (TR), and bottom right (BR) on a 2ML MoS_2 film grown on SiC confirming a constant separation between the E^1_{2g} peak and A^1_g peaks of $\delta = 21\ cm^{-1}$ at all four corners and, consequently, a high degree of thickness uniformity.

References:

[1] C. R. Serrao *et al.*, "Highly crystalline MoS_2 thin films grown by pulsed laser deposition," *Appl. Phys. Lett.*, vol. 106, no. 5, p. 052101, Feb. 2015, doi: 10.1063/1.4907169.

[2] Z. H. Aitken and R. Huang, "Effects of mismatch strain and substrate surface corrugation on morphology of supported monolayer graphene," *Journal of Applied Physics*, vol. 107, no. 12, p. 123531, Jun. 2010, doi: 10.1063/1.3437642.

[3] H. Li *et al.*, "From Bulk to Monolayer MoS2: Evolution of Raman Scattering," *Adv. Funct. Mater.*, vol. 22, no. 7, pp. 1385–1390, Apr. 2012, doi: 10.1002/adfm.201102111.

[4] C. Lee, H. Yan, L. E. Brus, T. F. Heinz, J. Hone, and S. Ryu, "Anomalous Lattice Vibrations of Single- and Few-Layer MoS_2," *ACS Nano*, vol. 4, no. 5, pp. 2695–2700, May 2010, doi: 10.1021/nn1003937.

[5] P. A. Bertrand, "Surface-phonon dispersion of MoS 2," *Phys. Rev. B*, vol. 44, no. 11, pp. 5745–5749, Sep. 1991, doi: 10.1103/PhysRevB.44.5745.

Chapter 5

MoS_2 Device Characterization

Of the MoS_2 films synthesized, samples with a thickness of 8 nm grown on GaN(0001) substrates were chosen to be incorporated into top-gated transistor devices for electrical characterization. These samples exhibited very clean Raman spectra, among the best XRD patterns, and the highest degree of uniformity as evaluated by visual inspection of cross-sectional TEM micrographs. In addition, these films provided a mechanically more substantive film which was hypothesized to be more resilient to the deposition of additional device layers and electrical contacts.

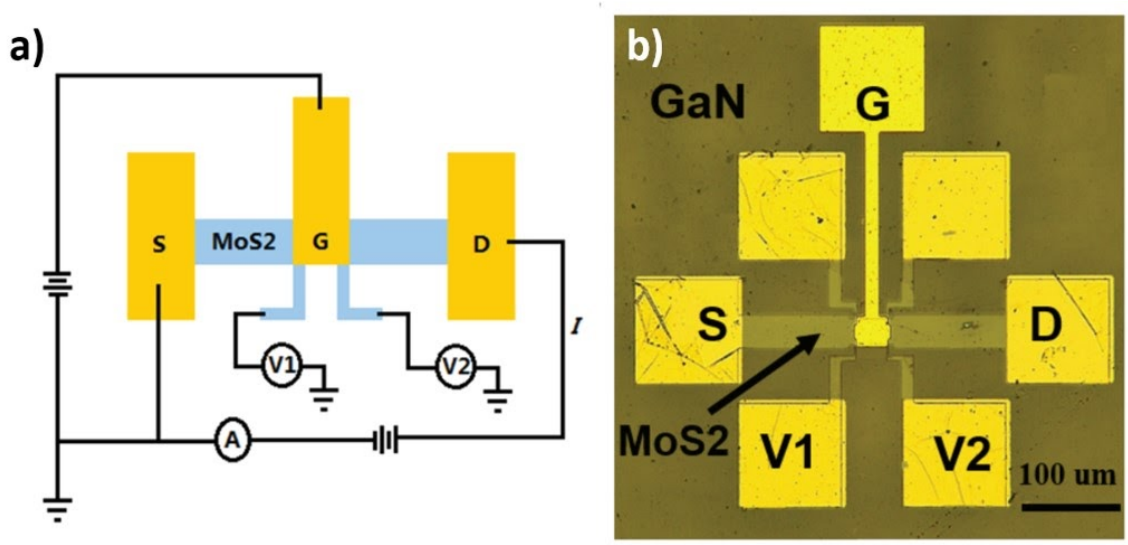

Figure 5.1) a) Circuit schematic for the top-gated four-probe MoS_2 transistor. Channel dimensions are W = 30 μm, L(between $V_1$and V_2)= 30 μm. b) Optical micrograph of the MoS_2 transistor structure showing the GaN substrate, patterned MoS_2 films as the channel, and the source, drain, and channel potential electrodes (Ti 3 nm/ Au 50 nm). [1]

A 15 nm thick layer of Al_2O_3 grown by atomic layer deposition (ALD) was used as the top gate dielectric. Al_2O_3 was selected because of its quasi-epitaxial relationship

to MoS_2 in hopes that a reduction in interfacial mismatch strain could reduce the presence of defects introduced at the interface. Electrical contacts consisting of 3nm of Ti capped with 50 nm of Au were grown by magnetron sputtering. As a low work function metal, Ti was demonstrated to form ohmic contacts to the MoS_2 thin films. Au was used as a capping layer to prevent oxidation of the Ti layer. Figure 5.1 (a) depicts a schematic representation of the top gated device as well as the electrical connections made for four-probe measurement configuration. As can be seen in the optical micrograph shown in Figure 5.1 (b) the channel width of the device was 30 μm while the channel length as measured between the voltage probe contacts was also 30 μm.

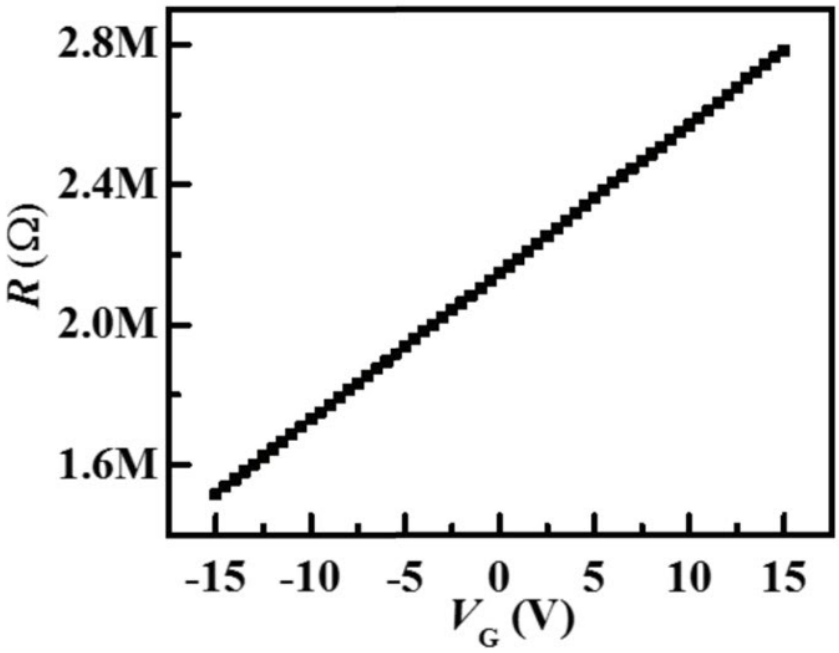

Figure 5.2) During I_D-V_G sweeps, the source electrode is held at ground and V_D is held constant (2.5 V) as V_G is swept. Current into the source and out of the drain electrode is monitored. The channel potential is measured during V_G sweeping. The close alignment of the edge of top-gate to the potential probes ensures that the potentials monitored at V_1 and V_2 are only of the gated channel region. [1]

The procedure for the gate-channel resistance measurement involved sweeping the gate voltage V_G while holding the drain voltage V_D at a constant 2.5 V. To accurately determine the current and voltage across the device channel, the drain current I_D was provided by a current source and the probe potentials V_1 and V_2 were monitored. Voltage sources were used to apply V_D and to measure the source current I_S and drain current I_D. Their placement in the measurement configuration is visible in the Figure 5.1 (a) schematic. Voltage monitoring units (VMU) were used to monitor V_1 and V_2 via channel probes and to source V_G. The close alignment of

the edge of top-gate to the potential probes as can be seen in Figure 5.1 (b) ensured that the potentials monitored at V_1 and V_2 were only that of the gated channel region. During I_D-V_G sweeps, the source electrode is held at ground. V_G was swept from -15V to +15V.

As is visible in Figure 5.2, from the small signal resistance measurement, the gated-channel resistance increased from 1.5 MΩ to 2.8 MΩ. This approximate two-fold increase in resistance indicated that the MoS_2 film was P-type. A calculated resistivity value of 1.6 Ω-cm obtained from the measurement suggests the presence of meaningfully large defect densities in the top-gated MoS_2 device. More recent work to understand defect chemistry and electron structure contributions in MoS_2 has suggested that P-type doping can occur in either S-rich samples by the presence of sulfur in anti-sites, intercalates and/or interstitials or the existence of molybdenum vacancies [2]. Given the significant efforts undertaken to ensure the synthesized MoS_2 samples were not sulfur poor, it is hypothesized that the P-type nature of the films can be attributed to excess sulfur content induced doping.

References

[1] C. R. Serrao *et al.*, "Highly crystalline MoS_2 thin films grown by pulsed laser deposition," *Appl. Phys. Lett.*, vol. 106, no. 5, p. 052101, Feb. 2015, doi: 10.1063/1.4907169.

[2] S. McDonnell, R. Addou, C. Buie, R. M. Wallace, and C. L. Hinkle, "Defect-Dominated Doping and Contact Resistance in MoS_2," *ACS Nano*, vol. 8, no. 3, pp. 2880–2888, Mar. 2014, doi: 10.1021/nn500044q.

Chapter 6

Conclusion and Future Directions

Moore's Law, first predicted in 1965 [1], has been maintained for more than four decades having enormous implications for the economics of computational power, the types of applications it can be applied to and expectations for continued economic growth. However, in recent years, device scaling has come up against physical limitations. As channel widths have continued to shrink, traditional MOSFET devices have begun to exhibit a number of physical effects that manifest themselves when standard device architectures scale down such as drain-induced barrier lowering, impact ionization, surface scattering, velocity saturation, and hot carrier injection [2]–[6]. The atomic scale thickness or 2D nature of transition metal dichalcogenides are advantageous when compared to bulk or 3D materials because of the reduced susceptibility to these short-channel effects [7].

Additionally, the ever growing need for computational power and the emergence of IoT have put a spotlight on device power consumption. Significant advancement toward low subthreshold slope devices, such as the TFET, has been made in recent years in a number of material systems [8]–[13], however there has still been great difficulty in developing TFET devices with high On current and subthreshold slopes under 60 mV/dec over multiple current decades. When coupled with the larger direct bandgap of monolayer MoS_2 devices which promise higher On/Off current ratios than Si based MOSFETs [7], MoS_2 based TFETs have proven to be an exciting avenue of study with the ATLAS-FET being the first planar TFET to demonstrate sub-thermionic subthreshold swings averaging 31 mV/decade over 4 decades and very low V_{DS} of 0.1V [14].

In order to materialize the promise of MoS_2, appropriate methods for large area growth must be developed. While there have been many approaches explored, most suffer from inconsistency such as exfoliation [15]–[18], are limited to small areas such as CVD [19], or have limited thickness control such as vapor solid epitaxy [20]. PLD is a PVD technique that offers unique capabilities for thin film synthesis such as possessing a wide array of tunable growth parameters, the ability to generate plasmas

that have less dependence on the vapor pressures of the target constituent, and the ability to grow metastable phases.

To avoid the preferential desorption of sulfur from the films during the growth process, a number of steps were taken to ensure sulfur rich growth conditions such as target enrichment and maintaining higher ambient background pressures. Substrates were chosen with well defined epitaxial relationships to establish strong out-of-plane texture and to minimize in-plane mismatch strain.

The resulting films were found to be highly crystalline with the desired in-plane and out-of-plane orientation and rocking curves with FWHM as low as 0.01 deg while demonstrating excellent thickness control down to a single monolayer and high film uniformity over large areas (0.25 cm^2). Films were found to have interlayer growth at higher film thicknesses and to exhibit corrugation which was hypothesized to be a result of van der Waals interaction coupled with in-plane mismatch strain. Electrical characterization of top-gated FETs incorporating the MoS_2 thin films revealed P-type behavior indicating meaningfully high defect densities.

Future avenues of investigation may include evaluating samples with X-ray photoemission spectroscopy to understand the types and concentration of defects that may be contributing to the electrical properties of the films. Computational modeling of material structure could be employed to determine if there is a deeper connection between the defects present and the faceted corrugation observed in the films. Additional steps to reduce the density of laser particles could be taken such as using a particle screen or minimizing target porosity which is expected to have beneficial effects to decrease film defects. Further work to evaluate annealing treatments in sulfurous environments could be explored, as the results presented here were by no means exhaustive. Additionally, reactive PLD whereby a Mo target is used as the cation source and a sulfur background gas acts as the anion source may provide a higher degree of compositional control. This technique variation is valuable because of the ability to tune the presence of the desired species in a continuous fashion without the need to fabricate additional targets. Finally, for the purposes of device fabrication and characterization, HfO_2 should be explored as a top-gating dielectric as it has shown promise at reducing interfacial defect states in other investigations [21].

While MoS_2 paired with TFET device architectures has demonstrated promise in initial investigations, it is just one of a multitude of approaches that are attempting to address the societal need for faster, lower power consuming computational systems. With the advent of machine learning and artificial intelligence, our relationship to computational power will be a defining characteristic in our evolution as a species. While the difficulties of continuing the phenomenal technological trend of Moore's Law sustained over the past four decades will be an immense challenge, there is little

that human ingenuity cannot achieve when combined with a spirit of curiosity and collaboration.

References

[1] G. E. Moore, "Cramming more components onto integrated circuits, Reprinted from , volume , number 8, April 19, 1965, pp.114 ff. - IEEE Journals & Magazine," *Electronics*, vol. 38, Accessed: Oct. 16, 2019. [Online]. Available: https://ieeexplore.ieee.org/document/4785860.

[2] K. M. Cham, S.-Y. Oh, J. L. Moll, K. Lee, P. Vande Voorde, and D. Chin, "Drain-Induced Barrier Lowering in Short Channel Transistors," in *Computer-Aided Design and VLSI Device Development*, K. M. Cham, S.-Y. Oh, J. L. Moll, K. Lee, P. Vande Voorde, and D. Chin, Eds. Boston, MA: Springer US, 1988, pp. 197–209.

[3] W. Muller, L. Risch, and A. Schutz, "Short-channel MOS transistors in the avalanche-multiplication regime," *IEEE Transactions on Electron Devices*, vol. 29, no. 11, pp. 1778–1784, Nov. 1982, doi: 10.1109/T-ED.1982.21026.

[4] V. K. Khanna, "Short-Channel Effects in MOSFETs," in *Integrated Nanoelectronics*, New Delhi: Springer India, 2016, pp. 73–93.

[5] G. W. Taylor, "Velocity-saturated characteristics of short-channel MOSFETs," *AT&T Bell Laboratories Technical Journal*, vol. 63, no. 7, pp. 1325–1404, Sep. 1984, doi: 10.1002/j.1538-7305.1984.tb00039.x.

[6] J. Keane and C. H. Kim, "Transistor Aging," *IEEE Spectrum*. https://spectrum.ieee.org/semiconductors/processors/transistor-aging (accessed Oct. 16, 2019).

[7] Y. Yoon, K. Ganapathi, and S. Salahuddin, "How Good Can Monolayer MoS_2 Transistors Be?," *Nano Lett.*, vol. 11, no. 9, pp. 3768–3773, Sep. 2011, doi: 10.1021/nl2018178.

[8] K. K. Bhuwalka, J. Schulze, and I. Eisele, "Performance Enhancement of Vertical Tunnel Field-Effect Transistor with SiGe in the δp+ Layer," *Jpn. J. Appl. Phys.*, vol. 43, no. 7R, p. 4073, Jul. 2004, doi: 10.1143/JJAP.43.4073.

[9] G. Dewey *et al.*, "Fabrication, characterization, and physics of III–V heterojunction tunneling Field Effect Transistors (H-TFET) for steep sub-threshold swing," in *2011 International Electron Devices Meeting*, Dec. 2011, pp. 33.6.1-33.6.4, doi: 10.1109/IEDM.2011.6131666.

[10] A. C. Ford *et al.*, "Ultrathin body InAs tunneling field-effect transistors on Si substrates," *Appl. Phys. Lett.*, vol. 98, no. 11, p. 113105, Mar. 2011, doi: 10.1063/1.3567021.

[11] H. Lu and A. Seabaugh, "Tunnel Field-Effect Transistors: State-of-the-Art," *IEEE Journal of the Electron Devices Society*, vol. 2, no. 4, pp. 44–49, Jul. 2014, doi: 10.1109/JEDS.2014.2326622.

[12] W. Y. Choi, B.-G. Park, J. D. Lee, and T.-J. K. Liu, "Tunneling Field-Effect Transistors (TFETs) With Subthreshold Swing (SS) Less Than 60 mV/dec," *IEEE Electron Device Letters*, vol. 28, no. 8, pp. 743–745, Aug. 2007, doi: 10.1109/LED.2007.901273.

[13] J. Appenzeller, Y.-M. Lin, J. Knoch, and Ph. Avouris, "Band-to-Band Tunneling in Carbon Nanotube Field-Effect Transistors," *Phys. Rev. Lett.*, vol. 93, no. 19, p. 196805, Nov. 2004, doi: 10.1103/PhysRevLett.93.196805.

[14] D. Sarkar *et al.*, "A subthermionic tunnel field-effect transistor with an atomically thin channel," *Nature*, vol. 526, no. 7571, pp. 91–95, Oct. 2015, doi: 10.1038/nature15387.

[15] K. F. Mak, C. Lee, J. Hone, J. Shan, and T. F. Heinz, "Atomically Thin MoS 2 : A New Direct-Gap Semiconductor," *Phys. Rev. Lett.*, vol. 105, no. 13, p. 136805, Sep. 2010, doi: 10.1103/PhysRevLett.105.136805.

[16] W. M. R. Divigalpitiya, R. F. Frindt, and S. R. Morrison, "Inclusion Systems of Organic Molecules in Restacked Single-Layer Molybdenum Disulfide," *Science*, vol. 246, no. 4928, pp. 369–371, Oct. 1989, doi: 10.1126/science.246.4928.369.

[17] C. Lee, H. Yan, L. E. Brus, T. F. Heinz, J. Hone, and S. Ryu, "Anomalous Lattice Vibrations of Single- and Few-Layer MoS_2," *ACS Nano*, vol. 4, no. 5, pp. 2695–2700, May 2010, doi: 10.1021/nn1003937.

[18] A. Splendiani *et al.*, "Emerging Photoluminescence in Monolayer MoS_2," *Nano Lett.*, vol. 10, no. 4, pp. 1271–1275, Apr. 2010, doi: 10.1021/nl903868w.

[19] Y.-H. Lee *et al.*, "Synthesis of Large-Area MoS_2 Atomic Layers with Chemical Vapor Deposition," *Adv. Mater.*, vol. 24, no. 17, pp. 2320–2325, May 2012, doi: 10.1002/adma.201104798.

[20] L. Ma *et al.*, "Epitaxial growth of large area single-crystalline few-layer MoS_2 with high space charge mobility of 192 $cm^2 V^{-1} s^{-1}$," *Appl. Phys. Lett.*, vol. 105, no. 7, p. 072105, Aug. 2014, doi: 10.1063/1.4893143.

[21] B. Radisavljevic and A. Kis, "Mobility engineering and a metal–insulator transition in monolayer MoS2," *Nature Mater*, vol. 12, no. 9, pp. 815–820, Sep. 2013, doi: 10.1038/nmat3687.